

Self-Cleaning Titania-Polyurethane Composites

(Spine title: Self-Cleaning Titania-Polyurethane Composites)

(Thesis format: Monograph)

by

Kevin David Burgess

Graduate Program in Chemical Engineering

A thesis submitted in partial fulfillment  
of the requirements for the degree of  
Master of Engineering Science

Faculty of Graduate Studies  
The University of Western Ontario  
London, Ontario, Canada

© Kevin David Burgess 2007

THE UNIVERSITY OF WESTERN ONTARIO  
FACULTY OF GRADUATE STUDIES

**CERTIFICATE OF EXAMINATION**

Supervisor

\_\_\_\_\_  
Dr. Paul A. Charpentier

Supervisory Committee

\_\_\_\_\_  
Dr. Amin S. Rizkalla

Examiners

\_\_\_\_\_  
Dr. Robert J. Klassen

\_\_\_\_\_  
Dr. Dimitre G. Karamanev

\_\_\_\_\_  
Dr. Amin S. Rizkalla

The thesis by

**Kevin David Burgess**

entitled:

**SELF-CLEANING TITANIA-POLYURETHANE COMPOSITES**

is accepted in partial fulfillment of the  
requirements for the degree of  
Master of Engineering Science

Date \_\_\_\_\_

\_\_\_\_\_  
Chair of the Thesis Examination Board

## ABSTRACT

The photooxidation of the polymer, polyurethane (PU), and the photocatalytic oxidation of its nanocomposites containing titanium dioxide (TiO<sub>2</sub>) nanoparticles, was investigated when exposed to ultraviolet radiation. The wettability, cleanability, and self degradation were studied using FTIR, TGA, SEM, AFM, and sessile drop analysis. The TiO<sub>2</sub> nanoparticles consisted of a 50:50 mixture of anatase:rutile crystal structure. Rutile TiO<sub>2</sub> nanoparticles have high UV opacity and low photoactivity, and are effective UV protectors for many polymer systems including polyurethanes. Anatase TiO<sub>2</sub> also acts as an opacifier, but unlike the rutile crystal structure, operates as an effective photocatalyst, decomposing organic materials. However, TiO<sub>2</sub> nanoparticles tend to strongly agglomerate causing poor dispersions within a PU matrix due to their strong intermolecular forces caused by increased surface area. The functionalization of these nanoparticles was found to aid in the breaking up of these agglomerates. Two techniques were explored for preparing TiO<sub>2</sub>-PU nanocomposites, one a polymer functionalization method, and the other a monomer functionalization method. The monomer functionalization method exhibited greater dispersion of TiO<sub>2</sub> nanoparticles in the PU matrix than the polymer functionalization method, thus increasing the thermal properties of the PU composite. Although increasing the surface area of TiO<sub>2</sub> by a better dispersion technique increased the amount of active sites for photocatalysis, it also increased the rate of electron-hole recombination, thus decreasing the composites cleanability efficiency and self-degradation. Increasing the mass percentage of TiO<sub>2</sub> in the PU composite coating decreased the contact angle with water, thus increasing the wettability and cleanability of the composite coating, but also increasing the self-degradation of the coating.

**Key Words:** photocatalysis, polyurethane, photodegradation, titanium dioxide, self-cleaning, functionalization.

## **DEDICATION**

To the people in my life who have always believed in me,  
seen me at my best and worst,  
my parents, David and Dawn Burgess, and  
my Aunt and Uncle, David and Kim Gelencher;  
Thank-you all for always being there for me.

## ACKNOWLEDGEMENTS

There are a many individuals that I would like to acknowledge for their help, support, encouragement, and patience throughout the past two years. Firstly, I would like to express my great appreciation and respect to my advisor, Dr. Paul Charpentier, who through numerous means provided me guidance, support, respect, and friendship though the progression of this research project. Without him, none of this would have been possible.

I would also like to extend acknowledgement to my fellow group members in the Supercritical Fluids Group at the University of Western Ontario, specifically Behnaz Hojjati, Zhiming (William) Xu, S.M. Zahangir Khaled, who provided their ongoing support, questions and suggestions.

Special thanks go to my close friends; Sara, Elwood, Brent, Paul, Mike, and Jay; my parents, Dawn and David; my brothers, Matthew and Ryan, for their love and encouragement throughout my life.

## TABLE OF CONTENTS

<b><i>CERTIFICATE OF EXAMINATION</i></b>	<b><i>II</i></b>
<b><i>Abstract</i></b>	<b><i>III</i></b>
<b><i>Dedication</i></b>	<b><i>IV</i></b>
<b><i>Acknowledgements</i></b>	<b><i>V</i></b>
<b><i>Table of Contents</i></b>	<b><i>VI</i></b>
<b><i>List of Figures</i></b>	<b><i>IX</i></b>
<b><i>List of Tables</i></b>	<b><i>XI</i></b>
<b><i>List of Abbreviations</i></b>	<b><i>XII</i></b>
<b><i>Nomenclature</i></b>	<b><i>XIII</i></b>
<b><i>Introduction</i></b>	<b><i>1</i></b>
<b><i>Objectives</i></b>	<b><i>3</i></b>
<b><i>Literature Review</i></b>	<b><i>4</i></b>
<b>1.1 Self Cleaning Coatings</b>	<b><i>4</i></b>
<b>1.2 Surface and Interfacial Properties of Films</b>	<b><i>4</i></b>
<b>1.3 Hydrophobic coatings</b>	<b><i>6</i></b>
1.3.1 Effect of Surface Roughness – Wenzel Equation	<i>7</i>
<b>1.4 Hydrophilic coatings</b>	<b><i>9</i></b>
<b>1.5 Photocatalysis</b>	<b><i>9</i></b>
1.5.1 Basic Principles – Heterogeneous Photocatalysis	<i>9</i>
1.5.2 Photocatalysis Chemistry	<i>10</i>
1.5.2.1 Intensity of Light	<i>10</i>
1.5.2.2 Step 1	<i>11</i>
1.5.2.3 Step 2	<i>12</i>
1.5.2.4 Step 3	<i>12</i>
1.5.2.5 Step 4:	<i>14</i>
1.5.3 Photoactivity	<i>14</i>
1.5.4 Electron-Hole Recombination	<i>14</i>
<b>1.6 Titanium Dioxide Photocatalysis</b>	<b><i>14</i></b>
1.6.1 Titanium dioxide Properties	<i>15</i>
1.6.2 TiO <sub>2</sub> Photo-reactive Crystal Structures	<i>16</i>
1.6.3 TiO <sub>2</sub> Photocatalysis Chemistry	<i>17</i>
<b>1.7 Applications of TiO<sub>2</sub> Photocatalysts</b>	<b><i>18</i></b>
1.7.1 Sterilizing Effect	<i>18</i>
<b>1.8 Self Cleaning Coatings</b>	<b><i>18</i></b>
1.8.1 Film Preparation	<i>18</i>
1.8.1.1 Solution routes	<i>19</i>
1.8.1.2 Gas phase methods	<i>19</i>
1.8.2 Ceramic Substrates	<i>20</i>
1.8.3 Glass Substrates	<i>20</i>

<b>1.9</b>	<b>Polymeric Substrates</b>	<b>22</b>
1.9.1	Surface Chemistry of Nanoparticles in Polymeric Materials	22
1.9.2	Metal Oxide Functionalization	22
1.9.2.1	Physisorption	23
1.9.2.2	Chemisorption	24
<b>1.10</b>	<b>Functionalization</b>	<b>24</b>
1.10.1	Polymer Functionalization	25
1.10.2	Monomer Functionalization	25
1.10.3	Photocatalytic Polymer Degradation	26
<b>1.11</b>	<b>Polyurethanes</b>	<b>27</b>
<b>1.12</b>	<b>Polyurethane Elastomers:</b>	<b>28</b>
1.12.1	Polyurethane Chemistry:	29
1.12.2	Bonding Properties	30
<b>Experimental Section</b>		<b>31</b>
<b>1.13</b>	<b>Materials</b>	<b>31</b>
<b>1.14</b>	<b>Polyurethane Elastomer Synthesis</b>	<b>31</b>
1.14.1	Experimental Setup	31
1.14.2	Polyurethane Synthesis	32
1.14.3	Monomer Functionalization Synthesis	33
<b>1.15</b>	<b>Characterization Methods</b>	<b>33</b>
1.15.1	Fourier Transform Infrared Spectroscopy	34
1.15.2	In situ Fourier Transform Infrared Spectroscopy	34
1.15.3	Thermo-Gravimetric Analysis	34
1.15.4	Atomic Force Microscopy	34
1.15.5	Scanning Electron Microscopy	35
1.15.6	Energy Dispersive X-ray Detection	35
1.15.7	Contact Angle Characterization	35
1.15.8	Characterization of self-cleaning photocatalytic properties	35
1.15.9	Characterization of self-cleaning degradable PU-TiO <sub>2</sub> composite coatings	36
1.15.10	Statistical Analysis	36
<b>Results - Chemistry</b>		<b>37</b>
<b>1.16</b>	<b>Polyurethane Synthesis</b>	<b>37</b>
<b>1.17</b>	<b>Fourier Transform Infrared Spectroscopy of Optimized Polyurethanes</b>	<b>38</b>
<b>1.18</b>	<b>Monomer Functionalization</b>	<b>40</b>
1.18.1	Scanning Electron Microscopy Imaging	40
1.18.2	FTIR analysis	43
1.18.3	In situ FTIR analysis	44
1.18.4	In situ FTIR Functionalization Kinetic Behavior	46
1.18.5	TGA Analysis	48
<b>1.19</b>	<b>Functionalized Polyurethanes</b>	<b>50</b>
1.19.1	SEM Analysis for TiO <sub>2</sub> Agglomeration	51
1.19.2	TGA Analysis	56
1.19.3	FTIR analysis	57
<b>1.20</b>	<b>Cleanability</b>	<b>58</b>
1.20.1	Surface Cleaning	59
<b>1.21</b>	<b>Results - Wettability</b>	<b>62</b>
1.21.1	Surface Roughness	62

<b>Results – Degradation of Polyurethane and its Composites</b>	<b>65</b>
<b>1.22 Polyurethane Thermal Degradation</b>	<b>65</b>
<b>1.23 Polyurethane Photodegradation</b>	<b>67</b>
<b>1.24 Polyurethane/TiO<sub>2</sub> Composite Degradation Chemistry</b>	<b>69</b>
1.24.1 Proposed Soft Segment Degradation	69
1.24.2 Hard Segment Degradation	70
<b>1.25 Photocatalytic degradation of Polyurethane</b>	<b>70</b>
<b>1.26 Thermogravimetric analysis</b>	<b>71</b>
1.26.1 Polyurethane Samples	76
1.26.2 5wt% TiO <sub>2</sub> -PU monomer method composite samples	77
1.26.3 5wt% TiO <sub>2</sub> -PU polymer method composite samples	78
1.26.4 10wt% TiO <sub>2</sub> -PU monomer method composite samples	80
1.26.5 Comparative TGA Analysis	80
<b>1.27 Fourier Transform Infrared Analysis</b>	<b>83</b>
1.27.1 Polyurethane Samples	83
1.27.2 TiO <sub>2</sub> -PU Composite Degradation (5% monomer functionalization method)	84
1.27.3 TiO <sub>2</sub> -PU Composite Degradation (5% polymer functionalization method)	85
1.27.4 TiO <sub>2</sub> -PU Composite Degradation (10wt% monomer functionalization method)	87
<b>Conclusions</b>	<b>89</b>
<b>Recommendations</b>	<b>90</b>
<b>References</b>	<b>92</b>
<b>Appendix A</b>	<b>101</b>
<b>Curriculum Vitae</b>	<b>109</b>

## LIST OF FIGURES

Figure 3.1 - Contact Angle Between Solid-Liquid-Vapor Phase of a Liquid Drop on a Flat Substrate. ....	6
Figure 3.2 – Sliding Water Droplet on an Ordinary Hydrophobic Surface Versus a Rolling Water Droplet on a Roughened Hydrophobic Surface. <sup>30</sup> .....	7
Figure 3.3 - TiO <sub>2</sub> photogenerated electron-hole pairs by UV excitation. ....	10
Figure 3.4 - Urethane Linkage. ....	28
Figure 3.5 - Schematic of Segmented Polyurethanes. ....	28
Figure 3.6 - Synthesis of Non-Segmented Polyurethanes - One Shot Process. ....	29
Figure 3.7 - Synthesis of Segmented Polyurethanes - Prepolymer Method. ....	29
Figure 4.1 – Polyurethane Laboratory Setup. ....	32
Figure 5.1 - Polyurethane Optimization for Varying ratio of NCO:OH groups. ....	37
Figure 5.2 – Segmented Polyurethane Elastomer Synthesis. ....	38
Figure 5.3 - FTIR Spectrum for optimized polyurethane elastomeric coating. ....	39
Figure 5.4 - HMPA Functionalization Synthesis. ....	40
Figure 5.5 – Digital Imaging of Crystal Color Change of HMPA (left) and Ti-HMPA (right). ....	40
Figure 5.6 – SEM Images of HMPA (a) 100μm Scale (b) 20μm Scale .....	41
Figure 5.7 - SEM Images of Ti-HMPA (a) 100μm Scale (b) 10μm Scale .....	42
Figure 5.8 - SEM Image of a Nano-TiO <sub>2</sub> Agglomerate. 5μm Scale. ....	42
Figure 5.9 – FTIR Peaks for (a) TiO <sub>2</sub> (b) HMPA (c) Ti-HMPA. ....	43
Figure 5.10 - Binding Modes of RCOO- with Titania Surface: (a) Chelating Bidentate, (b) Bridging Bidentate, and (c) Monodentate. ....	44
Figure 5.11 – FTIR Results for TiO <sub>2</sub> Coordination Peaks. ....	44
Figure 5.12 – In Situ Results for HMPA Functionalization – CO Range. ....	45
Figure 5.13 - In Situ Results for HMPA Functionalization – OH Range. ....	46
Figure 5.14 – Kinetic Data for TiO <sub>2</sub> -HMPA Functionalization. ....	47
Figure 5.15 -HMPA and Ti-HMPA DTG Curves for (a) 0% TiO <sub>2</sub> (b) 23.6% TiO <sub>2</sub> (c) 38.2% TiO <sub>2</sub> (d) 55.3% TiO <sub>2</sub> . Functionalization for Curves (b), (c), and (d) are Circled. ....	48
Figure 5.16 -HMPA and Ti-HMPA TG curves for (a) 0% TiO <sub>2</sub> (b) 23.6% TiO <sub>2</sub> (c) 38.2% TiO <sub>2</sub> (d) 55.3% TiO <sub>2</sub> . ....	49
Figure 5.17 – Functionalized Polyurethane Synthesis using the Monomer Approach. ....	50
Figure 5.18 - Functionalization Synthesis using the Polymer Approach. ....	51
Figure 5.19 – SEM Images for PU and TiO <sub>2</sub> -PU Composites. (a) PU (b) 5% TiO <sub>2</sub> -PU Composite – Polymer Functionalization Method (c) 5% TiO <sub>2</sub> -PU Composite – Monomer Functionalization Method and (d) 10% TiO <sub>2</sub> -PU Composite – Monomer Functionalization Method. All scale bars are 10μm. ....	52
Figure 5.20 - SEM-EDX Titanium Mapping of Composite Surfaces: Left is SEM Image, Right is EDX Image (a) 5wt% TiO <sub>2</sub> -PU Composite – Monomer Functionalization Method (b) 5wt% TiO <sub>2</sub> -PU Composite – Polymer Functionalization Method (c) 10wt% TiO <sub>2</sub> -PU Composite – Monomer Functionalization Method. ....	53
Figure 5.21 - EDX for PU Samples .....	54
Figure 5.22 - EDX for the 5wt% TiO <sub>2</sub> -PU Monomer Functionalization Method. ....	54
Figure 5.23 - EDX for the 5wt% TiO <sub>2</sub> -PU Polymer Functionalization Method. ....	55

Figure 5.24 - EDX for the 10wt% TiO <sub>2</sub> -PU Monomer Functionalization Method. ....	55
Figure 5.25 – Comparative Mass Loss with respect to Temperature for Different Concentrations and Functionalization Methods.....	56
Figure 5.26 – FTIR Comparisons for the Monomer Functionalized PU-TiO <sub>2</sub> composites at 0, 5, and 10wt% TiO <sub>2</sub> at 0 Hours of Degradation. ....	58
Figure 5.27 - FTIR Spectra for Composite Cleanability: (a) HMPA, (b) 5wt%TiO <sub>2</sub> -PU Composite Before Irradiation, (c) HMPA-Composite Mixture Before Irradiation, and (d) HMPA-Composite Mixture After 24 Hours After Irradiation.....	59
Figure 5.28 – Cleanability of HMPA from PU-TiO <sub>2</sub> Composites (a) Before Irradiation and (b) After Irradiation.....	60
Figure 5.29 – Proposed Chemistry for the Photocatalytic Degradation of HMPA (a) HMPA (l) Propanoic Acid (m) Pyruvic Acid (n) Acetaldehyde (o) Acetic Acid (p) Formic Acid (q) Glycolic Acid (r) Glyoxylic Acid (s) Oxalic Acid (t) CO <sub>2</sub> and H <sub>2</sub> O. ....	61
Figure 5.30 - AFM Image of 5wt% TiO <sub>2</sub> -PU Composite Produced by the Monomer Method.....	63
Figure 6.1 – Thermal Degradation of Urethane Linkages Forming CO <sub>2</sub> and an Olefin...	66
Figure 6.2 - Thermal Degradation of Urethane Linkages Forming CO <sub>2</sub> and a Secondary Amine.....	66
Figure 6.3 - Photolysis of MDI Polyurethanes via Photooxidation.....	67
Figure 6.4 - Photolysis of Polyurethanes via Urethane Scission.....	68
Figure 6.5 - Hard Segment Photocatalytic Degradation for TiO <sub>2</sub> -Polyurethane Composites.....	70
Figure 6.6 – A) TG and B) DTG Curves for PU for (a) 0 (b) 24 (c) 48 (d) 72 (e) 96 Hours of Irradiation. ....	72
Figure 6.7 – A) TG and B) DTG Curves for 5wt% TiO <sub>2</sub> -PU Composite - Monomer Method (a) 0 (b) 24 (c) 48 (d) 96 Hours of Irradiation.....	73
Figure 6.8 – A) TG and B) DTG Curves for 5wt% TiO <sub>2</sub> -PU Composite – Polymer Method - for (a) 0 (b) 24 (c) 48 (d) 96 Hours of Irradiation.....	74
Figure 6.9 – A) TG and B) DTG Curves for 10wt% TiO <sub>2</sub> -PU Composite – Monomer Method - for (a) 0 (b) 24 (c) 48 (d) 96 Hours of Irradiation.....	75
Figure 6.10 – Soft Segment Degradation Mass Loss with Time for: PU, 5M – 5wt% TiO <sub>2</sub> -PU Monomer Method Composites, 5P – 5wt% TiO <sub>2</sub> -PU Polymer Method Composites.....	79
Figure 6.11 – Comparative data at 0 hours of Irradiation for (PU) 0% TiO <sub>2</sub> , (5M) 5% TiO <sub>2</sub> – Monomer Method, (5P) 5% TiO <sub>2</sub> – Polymer Method, (10M) 10% TiO <sub>2</sub> – Monomer Method, (10P) 10% TiO <sub>2</sub> – Polymer Method. ....	81
Figure 6.12 - Comparative data at 100 hours of Irradiation for (a) 0% TiO <sub>2</sub> , (b) 5% TiO <sub>2</sub> – Monomer Method, (c) 10% TiO <sub>2</sub> – Polymer Method, (d) 10% TiO <sub>2</sub> – Monomer Method.....	81
Figure 6.13 - Digital Image for the (a) Top of the Film After UV Irradiation and (b) Bottom of the Film after UV Irradiation.....	82
Figure 6.14 – FTIR Analysis for Non-Functionalized PU Elastomer at (a) 0 Hours of Irradiation and (b) 100 Hours of Irradiation. ....	83
Figure 6.15 - FTIR Analysis for 5% TiO <sub>2</sub> -PU Composite Coating Produced Through the Polymer Method at (a) 0 Hours of Irradiation and (b) 100 Hours of Irradiation.....	84

Figure 6.16 - FTIR Analysis for 10% TiO <sub>2</sub> -PU Composite Coating Produced Through the Polymer Method at (a) 0 Hours of Irradiation and (b) 100 Hours of Irradiation.....	86
Figure 6.17 - FTIR Analysis for 10% TiO <sub>2</sub> -PU Composite Coatings Produced Through the Monomer Method at (a) 0 Hours of Irradiation and (b) 100 Hours of Irradiation.....	88
Figure A.1 - Soft Segment Degradation for Decreasing Mass % with Increasing Time of Irradiation –PU Elastomers.....	107
Figure A.2 - Soft Segment Degradation for Decreasing Mass % with Increasing Time of Irradiation – 5wt% TiO <sub>2</sub> -PU Composite – Monomer Method.....	107
Figure A.3 - Soft Segment Degradation for Decreasing Mass % with Increasing Time of Irradiation – 5wt% TiO <sub>2</sub> -PU Composite – Polymer Method.....	108

## LIST OF TABLES

Table 5.1 – Characteristic FTIR absorption frequencies in polyurethanes.....	39
Table 5.2 – TGA data for HMPA and Ti-HMPA.....	50
Table 5.3 - Calculations from Cassie's Equation.....	62
Table 6.1 - Onset of Dissociation for various Polyurethanes.....	65
Table A.1 – Raw Kinetic Data for the Functionalization of HMPA – Peak 1710cm <sup>-1</sup> ...	101
Table A.2 - Raw Kinetic Data for the Functionalization of HMPA – Peak 1050cm <sup>-1</sup> ...	102
Table A.3 - Common bond dissociation enthalpies <sup>96</sup> .....	103
Table A.4 – Average Photodegradation Values for Polyurethane Samples.....	104
Table A.5 – Average Photocatalytic Degradation Values for 5wt% TiO <sub>2</sub> -PU Composites Produced by the Monomer Functionalization Method.....	105
Table A.6 - Average Photocatalytic Degradation Values for 5wt% TiO <sub>2</sub> -PU Composites Produced by the Polymer Functionalization Method.....	106

## LIST OF ABBREVIATIONS

$A_{\text{ads}}$  – absorbed accepting molecule  
AFM – atomic force microscopy  
 $C_b$  – Conduction band  
CNT – carbon nanotubes  
CVD – chemical vapour deposition  
 $D_{\text{ads}}$  – adsorbed donor molecule  
DMF – dimethylformamide  
DTG – derivative thermogravimetric weight loss  
 $e^- - h^+$  – electron-hole pair  
EDX - energy dispersive x-ray  
Ti-HMPA – functionalized 2,2-bis(hydroxymethyl)propionic acid  
FTIR - fourier transform infrared  
HMPA - 2,2-bis(hydroxymethyl)propionic acid  
MDI – 4,4-methylene bis(p-phenyl isocyanate)  
PAN – polyacrylonitrile  
PEB – poly(ethylene-butane)  
PEO – poly(ethylene-oxide)  
PMEMA - methyl-ethyl methacrylate copolymer  
PMMA – poly(methylmethacrylate)  
PS – polystyrene  
PTHF – polytetrahydrofuran  
PTMEG - polytetramethylene etherglycol  
PU – polyurethane  
PVA – polyvinylalcohol  
PVC – poly(vinylchloride)  
PVD – physical vapour deposition  
SD – standard deviation  
SEM – scanning electron microscopy  
TDI - 1,6-toluene diisocyanate  
TG - thermogravimetric weight loss  
TGA – thermo-gravimetric analyzer  
THF – tetrahydrofuran  
UHMWPE – ultra-high molecular weight polyethylene  
 $V_b$  – Valance band

## NOMENCLATURE

- a – area ( $\text{m}^2$ )  
E – energy (J)  
 $E_{\text{cb}}$  – conduction band energy (J)  
 $E_{\text{gap}}$  – band gap energy (J)  
 $E_{\text{vb}}$  – valence band energy (J)  
f – frequency (Hz)  
 $f_i$  – surface fraction of a given component  
h – height (m)  
h – Planck's constant ( $\text{m}^2 \cdot \text{kg} \cdot \text{s}^{-1}$ )  
[M] – monomer concentration (mol/L)  
[Mo] – initial monomer concentration (mol/L)  
 $m_{\text{adj}}$  – adjusted mass of component i (kg)  
 $m_i$  – mass of component i (kg)  
 $R_{\text{rough}}$  – roughness factor (actual surface area / theoretical surface area)  
 $T_i$  – initial temperature of decomposition ( $^{\circ}\text{C}$ )  
 $T_i^{\text{max}}$  – maximum temperature of decomposition ( $^{\circ}\text{C}$ )  
v – velocity (m/s)  
 $\gamma$  – surface tension (N/m)  
 $\gamma_{\text{lv}}$  – liquid-vapour surface tension (N/m)  
 $\gamma_{\text{sl}}$  – solid-liquid surface tension (N/m)  
 $\gamma_{\text{sv}}$  – solid-vapour surface tension (N/m)  
 $\Delta H^{\circ}$  – standard enthalpy (J/kg)  
 $\theta$  – contact angle ( $^{\circ}$ )  
 $\theta_{\text{app}}$  – apparent contact angle ( $^{\circ}$ )  
 $\lambda$  – wavelength (nm)

## INTRODUCTION

Over the past 10 years, developments in bio and physical chemistry, microscopy, and engineering have shown great strides in understanding the properties and developing applications for nanoparticles. These technological innovations have led to the development of many tiny structures such as nanoshells, nanospheres, nanotubes, nanofillers, and quantum dots. There are many commercial products available today using these nanomaterials including transparent sunscreens, stain-resistant clothing, self-cleaning glass, paints, sports equipment, and numerous applications in electronics.

Nanofillers have previously been incorporated into paints and coatings to increase their mechanical strength, thereby increasing their lifespan. However, dirt and bacteria still accumulate on almost every surface, causing significant problems for cleaning and maintenance of these surfaces. Although these surfaces can be cleaned using chemical detergents accompanied with scrubbing and sometimes a high-pressure water jet, all these processes have inherent deficiencies such as the use of chemical detergents and high energy/labour costs.

A self-cleaning coating comprised of photocatalytic titanium dioxide ( $\text{TiO}_2$ ) offers three unique properties when exposed to ultraviolet (UV) light: 1) strong oxidation power that eliminates odor causing bacteria; 2) the breakdown of long chain organic molecules into smaller ones; and 3) a surface that experiences super-hydrophilicity, which allows these small chained organic molecules and everyday dirt and stains to be easily washed away with water. Due to the wide range of self-cleaning photocatalytic applications, from window glass<sup>1</sup> and cement to textiles<sup>2</sup>, self-cleaning coatings have the potential for creating important labour-saving and bacteria resistant surfaces.

Research into the photocatalyst semiconductor  $\text{TiO}_2$  began in the early 1970's with the work of Honda and Fujishima who investigated the splitting of water into oxygen and hydrogen using titanium dioxide irradiated by UV light.<sup>3</sup> Currently,  $\text{TiO}_2$  photocatalysis is actively used in the field of photodegradation of organic compounds, specifically in environmental decontamination of air<sup>4-11</sup> and water,<sup>12-15</sup> antibacterial surfaces, and

superhydrophilic coatings/glasses<sup>16-18</sup> for self-cleaning applications. All these areas utilize TiO<sub>2</sub>'s ability to breakdown organic compounds into CO<sub>2</sub> and H<sub>2</sub>O with UV light. As well, TiO<sub>2</sub> has many other applications other than photodegeneration, including photovoltaics, hydrogen generation, and as a common pigment in paints and textiles.

The main marketed photo-TiO<sub>2</sub> products include self-cleaning glass and air/water purification. However, clear coatings on organic substrates have proven to have many issues, impeding commercialization. Degradation on the substrate itself occurs for TiO<sub>2</sub> clear coat, which was coated directly on the polymeric substrate with poly(vinylchloride),<sup>19</sup> polystyrene,<sup>20</sup> and silicone polymer composites.<sup>20, 21</sup> To avoid surface degradation, an additional silica dioxide layer has been used,<sup>16</sup> however this incorporates increased costs and curing time. The incorporation of the photocatalyst bonded to the polymer, along with the study of its cleanability, wettability and degradation effects, has yet to be investigated for many polymers including polyurethanes. Also, attention has not been focused on the relationship between the photocatalysis, hydrophilicity, self-cleaning effect, and degradation on functionalized polymeric substrates.

Polyurethanes are commonly produced with rutile TiO<sub>2</sub> nanoparticles as an opacifying and UV stabilizing filler. To take advantage of the UV protection effect of rutile TiO<sub>2</sub> nanoparticles and the photocatalytic effect of anatase TiO<sub>2</sub>, an appropriate percentage of each crystal structure of TiO<sub>2</sub> nanoparticles into a polymer could be added. This can be used to protect polyurethanes in outdoor applications, improving the service life of the products, while allowing some self-cleaning properties for protection from outdoor contaminants.<sup>22</sup>

## **OBJECTIVES**

The objectives of this study are to:

1. Synthesize a polyurethane elastomeric coating containing a carboxylic acid functional group in the crystalline segment of the polymer;
2. Functionalize these subgroups with the nano spherical particles of self-cleaning titanium dioxide to use in photocatalysis;
3. Characterize the coatings in terms of its wettability, cleanability, and thermal properties, and;
4. Study the negative degradation effects of titanium dioxide photocatalysis on the polymer substrate.

## LITERATURE REVIEW

### 1.1 Self Cleaning Coatings

The ability of a surface to clean itself is attractive in terms of cost, maintenance, and the environment; all three of which are inter-related. There is a cost associated with cleaning solvents, and a time cost in scrubbing surfaces, along with a replacement cost from solvent use. Eliminating these costs not only benefits an individual, but also benefits society as a whole by eliminating solvent vapour into the environment, while also eliminating the harmful effects of bacteria from the surface.

Important properties of solid surfaces are wettability and water repellence, both of which depend directly on the surface energy and surface roughness. Surface energy, however, is an intrinsic property of the material employed, such that the wettability of the surface is difficult to control when exposed to ultraviolet light over an extended period of time.<sup>23</sup>

Self cleaning coatings clean themselves in the presence of water. They are divided into either super-hydrophobic or super-hydrophilic coatings. Hydrophobic coatings clean themselves by rolling droplets of water that carry away any dirt, while hydrophilic coatings clean themselves by sheeting water to remove dirt from the surface. Hydrophilic coatings, however, have the ability to chemically break down the absorbed organics in sunlight or UV.<sup>17</sup>

### 1.2 Surface and Interfacial Properties of Films

Surface and interfacial tensions are present whenever there is one or more condensed phase(s) and are measured in energy per unit area. Surface tension is the occurrence of one condensed phase, while interfacial tension is the occurrence of two condensed phases in contact with one another. One of the few measurable quantities in surface science is the contact angle at the intersection of three phases, typically solid, liquid and vapor phases. The contact angle is a measure of the competing tendencies of a drop to spread, so as to cover a solid surface or to round up so as to minimize its own area. The contact angle measures the wetting tendency, typically of a liquid droplet on a solid, and also

determines the boundary condition for the calculation of meniscus shapes from the Young-Laplace equation. Therefore, the contact angle can be used to calculate the surface tension of a solid surface and a liquid drop.<sup>24</sup>

The most common method for measuring the contact angle is to observe a sessile drop with a microscope using a light source positioned behind the drop, which makes the droplet appear dark. The contact angle is then determined directly with a goniometer, or the image is recorded by a video system and the contour is fitted by computer software using the Laplace equation. The Laplace equation can also use a circular cross-section of the droplet to predict its contact angle ( $\theta$ ). For small drops, hydrostatic effects are deemed negligible to where the contact angle is calculated from the measured height,  $h$ , and contact radius,  $a$ .<sup>25</sup>

$$\tan\left(\frac{\theta}{2}\right) = \frac{h}{a} \quad \mathbf{0.1}$$

The contact angle of a water droplets was first investigated by Thomas Young, who modeled the static contact angle of a droplet on a smooth surface. Young concluded that the interaction between the solid-liquid, liquid-vapor, and solid-vapor surface free energy can be determined by the water contact angle. The phenomenon of wetting is described quantitatively using Young's Equation, which relates contact angles to interfacial tensions ( $\gamma_{sv}$ ,  $\gamma_{lv}$ ,  $\gamma_{sl}$ ); where s, l, v are the solid, liquid, and vapor phases respectively. If a droplet of liquid is placed on a solid surface, the liquid can either spread completely giving a zero contact angle, or provide a measurable contact angle,  $\theta$ . For a  $\theta$  value greater than zero, a three-phase wetting line is created between the liquid, solid, and vapour as shown in Figure 3.1. Substrates with contact angles below 30° are termed super-hydrophilic, between 30-90° are hydrophilic, while above 90° are termed hydrophobic.<sup>25</sup>

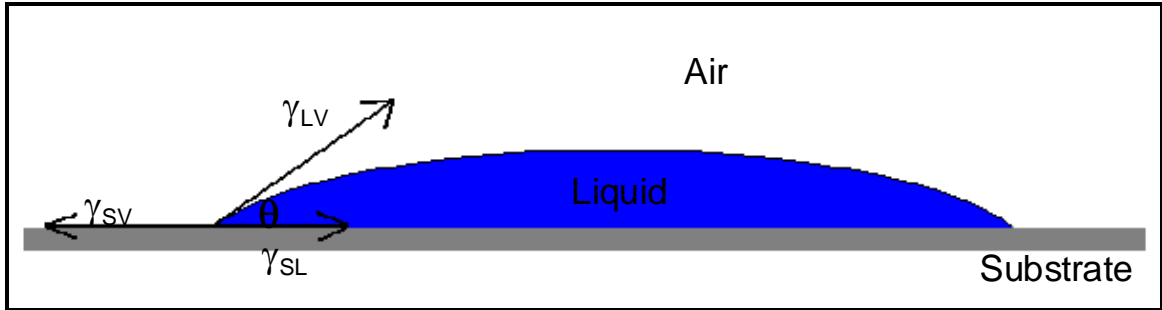


**Figure 0.1 - Contact Angle Between Solid-Liquid-Vapor Phase of a Liquid Drop on a Flat Substrate.**

Young's equation is the sum of the force vectors at equilibrium, and can be used to calculate the surface tension of a solid substrate given the three known liquid surface tensions, coupled with the three measured contact angles.

$$\gamma_{sv} = \gamma_{sl} + \gamma_{lv} \cos(\theta) \quad \mathbf{0.2}$$

However, when a water droplet rolls, hysteresis develops in the contact angles at both the advancing and receding solid-liquid-gas interfaces, in which case the contact angle of the advancing and receding ends differ in angle measurement. This can lead to errors in the surface tension, surface roughness, and surface energy calculations.<sup>25</sup>

### **1.3 Hydrophobic coatings**

Although hydrophobic coatings are those with contact angles greater than 90°, it is the rolling motion of the water droplet that cleans the surface. Many fluorinated polymer films such as Teflon™, are hydrophobic coatings that have contact angles of approximately 130 °.<sup>26</sup> However, these polymers are used as easy clean coatings rather than self-cleaning surfaces, because the contact angle is not high enough to cause the rolling motion for self-cleaning.<sup>27</sup> Hydrophobic self-cleaning coatings (superhydrophobic coatings) are driven by high contact angles with water, where water droplets on the surface are almost spherical, forming contact angles greater than 150-160°. Water droplets that form spheres with little to no adhesion with the surface are able to roll off the surface quickly, even at small inclinations.<sup>17</sup>

### 1.3.1 Effect of Surface Roughness – Wenzel Equation

The wettability of a solid surface is not only governed by the chemical composition, but also by the geometric micro/nanostructure of the surface as shown in Figure 3.2.<sup>28</sup> Water droplets as well as organic particles can only sit on top of the ridges of the surface, causing low adhesion forces between these particles. Therefore, when the surface and organic particles are exposed to water, the rolling water droplet creates adhesive forces with the contaminating particles, which are both effectively removed from the surface through a rolling motion.<sup>29</sup>

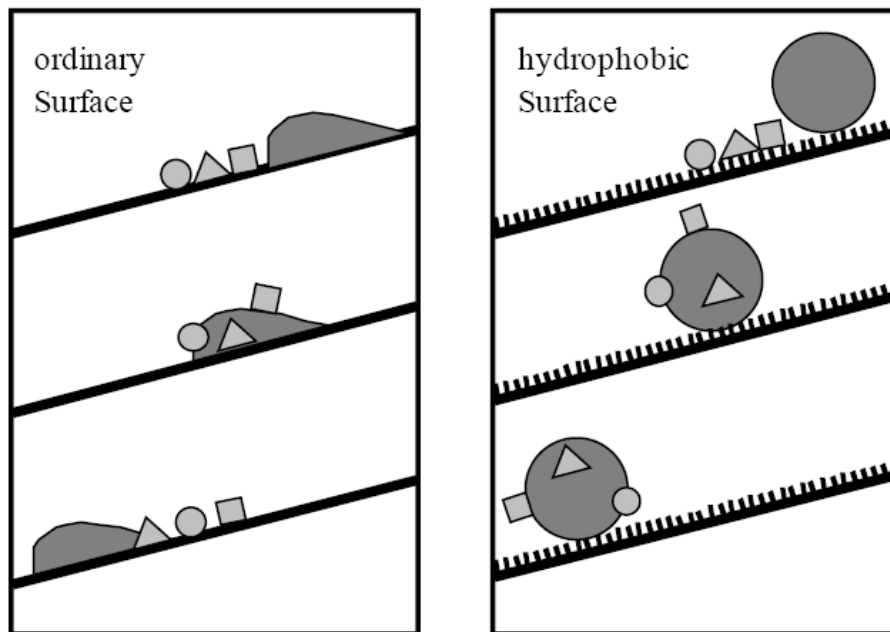


**Figure 0.2 – Sliding Water Droplet on an Ordinary Hydrophobic Surface Versus a Rolling Water Droplet on a Roughened Hydrophobic Surface.<sup>30</sup>**

Surface roughness plays a major role in contact angle science, as a water droplet placed on a micron textured hydrophilic surface causes the water to sink into the grooves, hence lowering the contact angle. This effect, however, has an opposite effect on a hydrophobic surface where Guo et al <sup>28</sup> showed a correlation between the contact angle and surface roughness, where increasing the surface roughness of a hydrophobic coating increased the contact angle almost uniformly. This is due to increases in surface energy by roughening, causing a greater differential in energy between the water droplet and the surface, causing the droplet to recede, thus forming larger contact angles.

There are many micron-scale texturing experiments to enhance surface roughening in order to increase the contact angle of a water droplet on hydrophobic surfaces. These experiments include: solidification, polymerization/etching, chemical vapor deposition, solvent-mediated phase separation, molding, and template-based extrusion. However, these methods are difficult to use for practical applications because of their complexity, material costs, and time consumption.<sup>28, 31-33</sup> Also, industrial coatings for most applications require smooth and aesthetic surfaces; hence surface roughening is not a viable option to increase/decrease the contact angle in coatings.<sup>17</sup>

However, as all surfaces are not perfectly smooth; roughness and heterogeneity of the surfaces leads to contact angle hysteresis, in which the mean contact angle is influenced. For surfaces that are rough and heterogeneous on a scale above the molecular scale, while below a scale where optical techniques could still be used, the surface roughness can be described by the Wenzel equation:

$$\cos \theta_{app} = R_{rough} \cos \theta \quad \mathbf{0.3}$$

where  $\theta_{app}$  is the apparent contact angle observed visually by eye or optical microscope, and  $R_{rough}$  is the ratio between the actual and projected surface area, and is always greater than or equal to one ( $R_{rough} \geq 1$ ). This equation thus shows that for  $\theta < 90^\circ$ , surface roughness decreases the apparent contact angle, while for  $\theta > 90^\circ$ , surface roughness increases the apparent contact angle.

Most solid surfaces are chemically non-homogeneous, to where the apparent contact angle is a function of two chemical species within or on the surface. Cassie<sup>34</sup> considered a smooth two component surface, where two different regions with contact angles  $\theta_1$  and  $\theta_2$  occupy the surface ratios  $f_1$  and  $f_2$ , giving an apparent average contact angle as:

$$\cos \theta_{app} = f_1 \cos \theta_1 + f_2 \cos \theta_2$$

0.4

## 1.4 Hydrophilic coatings

Hydrophilic coatings behave oppositely to that of hydrophobic coatings, with water having a high affinity for the surface, and a contact angle less than 90°. A self-cleaning hydrophilic surface (super-hydrophilic coating) cleans its surface not only by sheeting water, but also by chemically breaking down absorbed organic material when exposed to ultraviolet (UV) light; a process known as photocatalysis.<sup>1</sup>

## 1.5 Photocatalysis

Photocatalysis is the combination of photochemistry and catalysis with both light and a catalyst being required to start or accelerate a chemical transformation. Photocatalytic activity depends on the photocatalysts ability to create electron-hole pairings,<sup>35</sup> and is broken up into homogeneous and heterogeneous photocatalysis.

Heterogeneous photocatalysis includes many useful reactions in many different areas including: dehydrogenation, hydrogen transfer, oxidation reactions, metal deposition, and water and air purification. It can be carried out in either the gas phase or in solution.<sup>36</sup> This work focuses on heterogeneous photocatalysis, due to the desirable final application of the coating.

### 1.5.1 Basic Principles – Heterogeneous Photocatalysis

The oxidation/degradation of most hydrocarbons proceeds at a slow kinetic rate in the absence of a catalyst. However, a photocatalyst has the ability to decrease the activation energy, increasing the rate of oxidation.<sup>37</sup> Heterogeneous photocatalysis consists of a semiconductor photocatalyst in contact with a liquid and gaseous reaction medium, typically water and oxygen. Exposing the photocatalyst to light with a higher than its band gap energy, generates excited states in the photocatalyst that are able to initiate oxidation and reduction reactions, thereby forming molecular transformations.

### 1.5.2 Photocatalysis Chemistry

Figure 3.3 describes the production of electron-hole pairs that are photogenerated through excitation with a suitable energy light source, for example  $\text{TiO}_2$ , which requires a wavelength less than 388nm for photogenerated electron-hole production.<sup>36</sup> Photocatalysis is governed by the intensity of light that the semiconductor absorbs.

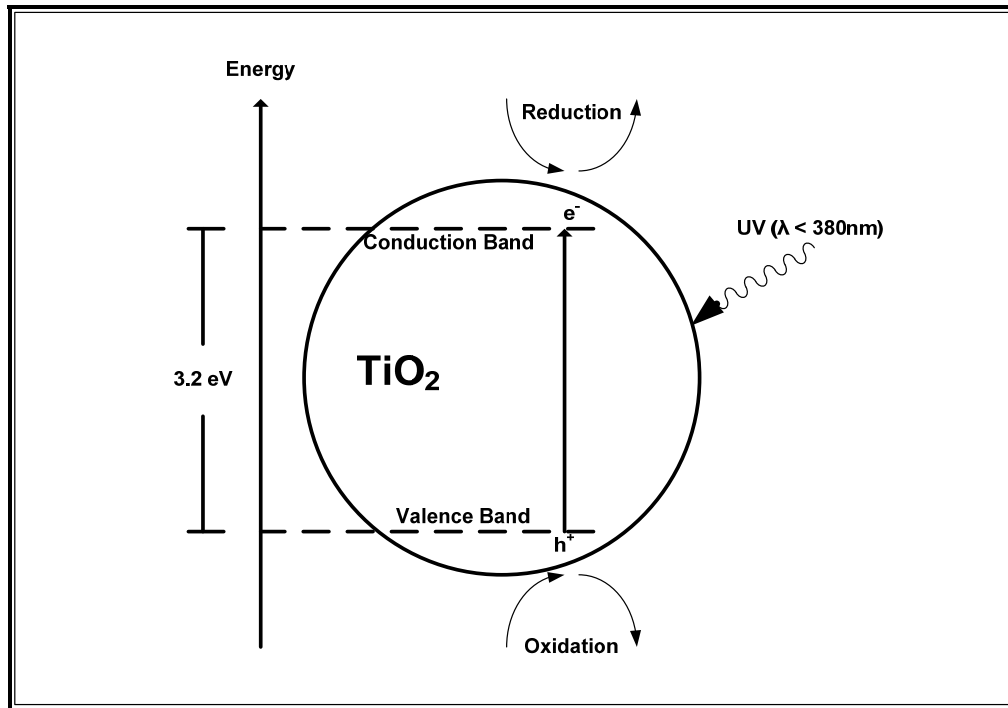


Figure 0.3 -  $\text{TiO}_2$  photogenerated electron-hole pairs by UV excitation.

#### 1.5.2.1 Intensity of Light

Electromagnetic radiation (the intensity of light) is determined using the wave model using a wavelength,  $\lambda$ , frequency,  $f$ , and velocity,  $v$ , such that:

$$\lambda f = v$$

0.5

where the speed of light,  $v$ , is a constant in vacuum at  $2.998 \times 10^8$  m/s. A photon is without mass but has a specific energy,  $E$ , related to the frequency of radiation by Planck's relation:

$$E = hf \quad \quad \quad \mathbf{0.6}$$

where  $h$  is Planck's constant,  $6.63 \times 10^{-34}$  J•s. By equating these two equations for a specific wavelength, the energy of an absorbed photon can be calculated. As mentioned earlier,  $\text{TiO}_2$  is a semiconductor with a band gap energy,  $E_{\text{gap}} = 3.2$  eV. Therefore, for photocatalysis to occur,  $\text{TiO}_2$  must be irradiated with photons with energy  $> 3.2$  eV, equivalent to  $\lambda < 388$  nm.<sup>30</sup> Regardless of the energy a molecule obtains when it absorbs a photon of light, it still may not compete in photocatalytic reactions due to competition among other deactivating processes which include radiative deactivation, radiationless deactivation, chemical reactions, and vibrational relaxation.<sup>37</sup>

Semiconductor heterogeneous photocatalytic reactions proceed on the surface of the photocatalyst through many steps: (a) production of photogenerated electron-hole pairs through semiconductor excitation; (b) separation of electrons and holes by available traps on the surface of the semiconductor; (c) a redox process between absorbed organics on the surface with the trapped electrons and holes; (d) desorption of the products, namely  $\text{CO}_2$  and  $\text{H}_2\text{O}$ , and reconstruction of the semiconductor surface.<sup>38</sup>

#### 1.5.2.2 Step 1

The initial stage for heterogeneous photocatalysis is the production of electron-hole pairs that are photogenerated through excitation with a suitable energy light source in order to promote electrons from the valence band ( $V_b$ ) to the conduction band ( $C_b$ ). As a result of this absorption, electron-hole pairs are formed having specific potential energies that correspond to their thermodynamic levels,  $E_{cb}$  for the electrons and  $E_{vb}$  for the holes. The difference between these levels forms the band gap energy,  $\Delta E_{\text{gap}}$ , which is the minimum quantity of light absorption required for electron-hole ( $e^-h^+$ ) separation as depicted by

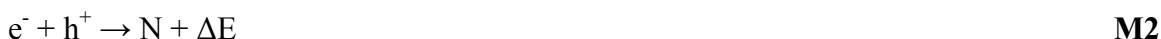
Mechanism 1 (M1). Radiation energy lower than this minimum will not promote photocatalysis, while radiation greater than the band gap will be dissipated as vibrational energy, and eventually lost as heat.



### 1.5.2.3 Step 2

Next, the electrons and holes have to be separated by available semiconductor surface traps (reactive species). Semiconductor materials must be controlled by three basic parameters: (1) light absorption property, (2) the rate of reduction and oxidation of reaction substrates by  $e^{-}$  and  $h^{+}$ , and (3) the rate of electron-hole recombination.<sup>39</sup>

In electrically conducting materials such as metals, the charge carriers produced recombine immediately, whereas semiconducting materials diffuse some of the photoexcited electron-hole charges to the surface, facilitating photocatalytic reactions.<sup>40</sup> For photocatalysis, this must occur at a higher rate than recombination of the electron-hole pairs. If these traps are not available on the semiconductor surface, the photogenerated electron-hole pairs recombine, converting the photoelectric energy into heat loss<sup>41</sup> as seen in Mechanism 2:



where  $N$  is the neutral center, and  $\Delta E$  is the energy released in the form of heat to the environment.<sup>36</sup>

### 1.5.2.4 Step 3

In this step, redox processes with absorbates present on the semiconductor surface are induced by the separated electrons and holes. This process determines the degradation reactions that take place. Chemical reactions with electrons and holes occur with either an adsorbed donor ( $D_{\text{ads}}$ ) or adsorbed accepting ( $A_{\text{ads}}$ ) molecule.<sup>42</sup> The valence band

holes ( $h^+$ ) oxidize donor molecules through Mechanism 3, whereas conduction band electrons ( $e^-$ ) reduce electron acceptor molecules via Mechanism 4. The photo-induced electron transfer ability from a semiconductor to an adsorbed particle is governed by the semiconductor band energy positions and adsorbate redox potentials.<sup>43</sup> The potential level of the acceptor species is required thermodynamically to be below the conduction band of the semiconductor, or above the valence band position of the semiconductor, in order to donate an electron to the empty hole.<sup>44</sup>



Only a portion of the photocatalyst can absorb incident photons, while the remainder of the photocatalyst does not participate in photocatalytic reactions. The quantity of substrate adsorbed on a photocatalyst particle increases with an increase of surface area, enhancing the reaction rate, while providing a constant density of  $e^-$  and  $h^+$  with the substrate.

Semiconductor metal oxides contain strong oxidation power through the reaction of  $h^+$ , which can react with water through an oxidation reaction to produce a highly reactive hydroxyl radical ( $\cdot\text{OH}$ ), as seen in Mechanism 5, which oxidizes most organic compounds/contaminants.<sup>42</sup>



Semiconductors also undergo a reduction reaction with oxygen, as seen in Mechanism 6, forming a super-oxide ion  $\text{O}_2\cdot^-$  that can react with an  $h^+$  to form a singlet oxygen able to oxidize saturated organic materials shown in Mechanism 7.



#### 1.5.2.5 Step 4:

The final stage of a photocatalysis reaction is desorption of the reaction products and reconstruction of the semiconductor surface.<sup>37</sup>

### 1.5.3 Photoactivity

Comparing photocatalysis results from various sources is difficult as the photoactivity of each sample is dependant on several experimental parameters, including surface area, crystal defects, particle size, and impurities. The precise influence these properties have on photocatalytic behaviour, especially for TiO<sub>2</sub>, is not fully understood.<sup>45</sup> Theoretically, nano-TiO<sub>2</sub> should be more photoactive than micron sized titania, due to a higher surface area, thus causing greater oxidation power of excited holes, and a greater reducing power of excited electrons.<sup>45</sup> However, studies have shown the opposite effect,<sup>46</sup> where films composed of closely packed nanoparticles display lower photoactivity than the larger immobilized TiO<sub>2</sub> particles.<sup>16</sup> This was attributed primarily to the increased recombination of electrons and holes.

### 1.5.4 Electron-Hole Recombination

Crystallinity plays an important role in the recombination of electrons and holes; with amorphous TiO<sub>2</sub> being found to have negligible photocatalytic activity due to the defects in the particles. It was assumed by Landsberg that the recombination of electron-hole pairs occurs at the crystal defect sites.<sup>47</sup> As mentioned earlier, a large surface area increases the amount of sites for photocatalytic activity with a given substrate; however, the large surface area also increases the recombination rate. Therefore, a combination of large surface area and high crystallinity is important for photocatalytic reactions.<sup>48, 49</sup>

## 1.6 **Titanium Dioxide Photocatalysis**

There are many semiconductor materials that can be used for heterogeneous photocatalysis, including ZnO, ZnS, CdS, Fe<sub>2</sub>O<sub>3</sub>, and TiO<sub>2</sub>. Titanium dioxide is typically

the photocatalyst of choice due to achieving the best photocatalytic performance with maximum quantum yields, especially the anatase crystal structure of  $\text{TiO}_2$ .<sup>36</sup>  $\text{TiO}_2$  photocatalytic oxidation has the following advantages, making it competitive to other processes oxidizing contaminants:

- $\text{TiO}_2$  is a low-cost material.
- The photocatalysis reaction is quite fast at mild operating conditions (room temperature, atmospheric pressure).
- A wide spectrum of organic contaminants can be converted to water and  $\text{CO}_2$ .
- No chemical reactants are required, and no side reactions are produced.<sup>42</sup>

#### 1.6.1 Titanium dioxide Properties

Titanium is found primarily in minerals such as rutile (the most stable form of titanium dioxide), anatase (defected crystal structure with a longer vertical axis), brookite, ilmenite, leucosene, perovskite, and sphene, and it is also found in titanates and many iron ores typically bound to oxygen in the form of titanium oxides.<sup>50</sup>

Titanium dioxide has become the material of choice for hydrophilic self-cleaning surfaces because of its favourable physical and chemical properties.  $\text{TiO}_2$  is not only an efficient photocatalyst for breaking down organic dirt in sunlight and obtaining superhydrophilicity, it is also non-toxic, inexpensive, and chemically inert in the absence of light.<sup>42</sup>  $\text{TiO}_2$  is relatively easy to handle and to deposit into thin films, and has been widely used in many household chemicals and applications such as a pigment in paints, cosmetics, and food additives.<sup>17</sup>  $\text{TiO}_2$  properties have been studied and reported according to the structure and characteristics of  $\text{TiO}_2$  particles, such as crystallinity and porosity.<sup>42, 44</sup> Photocatalytic activity, production of electron-hole pairs, surface adsorption, surface desorption and the redox process of  $\text{TiO}_2$  is influenced mainly by the crystal structure (anatase and/ or rutile), surface area, size distribution, porosity, and surface hydroxyl group density.<sup>38</sup>

$\text{TiO}_2$  has one major drawback, attributed to its high energy bandgap of 3.2 eV, meaning it functions only when exposed to ultraviolet light, compared to a more cost effective

source of energy, visible light. Even with a high energy bandgap, the several advantages of TiO<sub>2</sub> as a photocatalyst still offsets this disadvantage, and therefore still continues to be the most industrially and experimentally used photocatalyst for air/water purification and self cleaning coatings.<sup>16</sup>

### 1.6.2 TiO<sub>2</sub> Photo-reactive Crystal Structures

Titanium (IV) oxide exists in nature in two tetragonal forms, rutile and anatase, but it is also found in a rhombic form, brookite.<sup>42</sup> The rutile form of titanium dioxide has been found to have high UV opacity and low photoactivity, and is an effective UV protector for many polymer systems including polyurethane systems. The anatase form also acts as an opacifier, but unlike rutile crystal structures, operates as an effective photocatalyst, decomposing organic materials. Polyurethanes and its composites with anatase and rutile TiO<sub>2</sub> nanoparticles demonstrate that anatase nano-TiO<sub>2</sub> is a photosensitiser, and rutile nano-TiO<sub>2</sub> is a nano-stabilizer.<sup>22</sup>

The anatase crystalline phase of TiO<sub>2</sub> is the more thermodynamically unstable phase and has greater photocatalytic activity compared to that of the rutile phase. The small difference in band gap energy however, is not a factor in this property, but rather anatase possesses a greater Fermi level along with an increased degree of surface hydroxylation. As mentioned previously, the fundamental process of heterogeneous photocatalysis is the photon absorption of sufficient energy to elevate electrons from the valence band to the conduction band, and then trapping both the electrons and holes.<sup>38</sup> In photocatalysis processes performed in aqueous solution, the most abundant traps tend to be absorbed water either as an H<sub>2</sub>O radical or OH radical. It is this trapping process that directly competes with the electron-hole recombination processes, thus making anatase a more suitable form of TiO<sub>2</sub> for photocatalysis.<sup>51</sup>

However, the most effective method for trapping electrons and holes for reducing recombination, is the use of a space-charge layer at the surface, such as platinum or other chemisorbed substrates. Functionalization of a carboxylic acid will also act as a charge carrier for TiO<sub>2</sub> by absorbing e<sup>-</sup> and h<sup>+</sup>. The electric field in the space-charge layer of the

chemisorbed material-TiO<sub>2</sub> has the effect of moving the charged species in opposite directions of one another, thus reducing the recombination rate and providing no interference of a lattice phonon.<sup>51</sup>

### 1.6.3 TiO<sub>2</sub> Photocatalysis Chemistry

Titanium (IV) dioxide photocatalysis – initial reaction steps

1.  $\text{TiO}_2 + h\nu \rightarrow \text{TiO}_2^* (\text{e}^- + \text{h}^+)$
2.  $\text{TiO}_2^* (\text{e}^-) + \text{O}_2 \rightarrow \bullet\text{O}_2^-$
3.  $\text{TiO}_2^* (\text{h}^+) + \bullet\text{O}_2^- \rightarrow {}^1\text{O}_2$
4.  $\bullet\text{O}_2^- + \text{H}_2\text{O}_{(\text{g})} + \text{TiO}_2^* (\text{h}^+) \rightarrow \text{HO}\bullet_{(\text{g})} + \text{HO}_2\bullet$
5.  $2 \text{HO}_2\bullet_{(\text{g})} \rightarrow \text{H}_2\text{O}_2 + \text{O}_2$
6.  $\text{H}_2\text{O}_2 + h\nu \rightarrow 2 \text{HO}\bullet$
7.  $\text{TiO}_2^* (\text{h}^+) + \text{H}_2\text{O}_{(\text{adsorbed})} \rightarrow \text{HO}\bullet_{(\text{adsorbed})} + \text{H}^+$
8.  $\text{HO}\bullet_{(\text{adsorbed})} \rightarrow \text{HO}\bullet_{(\text{g})}$

Irradiation of TiO<sub>2</sub> with ultraviolet light greater than the 3.2eV band gap (wavelength  $\lambda < 388 \text{ nm}$ ) for TiO<sub>2</sub> creates an electron hole pairing (Step 1).<sup>17</sup> The electron reacts with an acceptor species, which in this case is oxygen as seen in Step 2 and the exciton/hole ( $\text{h}^+$ ) reacts with surface hydroxyl groups to form a hydroxyl radical (Step 7 – Step 8).<sup>52</sup>

The reaction between the excited state of TiO<sub>2</sub><sup>\*</sup> with the superoxide radical releases a singlet oxygen molecule, <sup>1</sup>O<sub>2</sub> (Step 3), which has the ability to attack any unsaturation within the polymer. This will have degradation effects for the hard segment of the polyurethane/TiO<sub>2</sub> composite explored in this thesis. The superoxide radical undergoes a reaction with entrained water in air, producing hydroxy and perhydroxy radicals (Step 4). The perhydroxy radical reacts forming peroxide, which undergoes a photoreaction splitting into two hydroxyl radicals (Step 5 – Step 6).<sup>53</sup> Throughout the entire reaction, TiO<sub>2</sub> is used, but it reconverts to TiO<sub>2</sub><sup>4+</sup>, thus it is used as a catalyst.<sup>54</sup>

## **1.7 Applications of TiO<sub>2</sub> Photocatalysts**

Currently, TiO<sub>2</sub> photocatalysis is actively used in the field of photodegradation of organic compounds, specifically in environmental decontamination of air and water, antibacterial surfaces, and superhydrophillic coatings/glasses for self-cleaning application. All these areas utilize TiO<sub>2</sub>'s ability to break down organic compounds into CO<sub>2</sub> and H<sub>2</sub>O. In addition, TiO<sub>2</sub> has many other applications including photovoltaics, hydrogen generation, and as a common pigment in paints and textiles.

### **1.7.1 Sterilizing Effect**

Photocatalysts have the ability to not only kill bacteria, but also to decompose the cell itself. The TiO<sub>2</sub> photocatalyst has been found to be more effective than any other antibacterial agent, as the photocatalytic reaction works even when there are cells covering the surface, and while the bacteria are actively propagating. The end toxin, if produced by the cell death, is also decomposed by photocatalytic action. TiO<sub>2</sub> does not deteriorate, and it shows a long-term anti-bacterial effect. Generally, disinfections by TiO<sub>2</sub> is three times stronger than chlorine, and 1.5 times stronger than ozone.<sup>30</sup>

## **1.8 Self Cleaning Coatings**

### **1.8.1 Film Preparation**

Lately, an increasing amount of semiconductor photocatalysis research, especially using nano-TiO<sub>2</sub>, has moved from the use of powder dispersions to their use in thin films.<sup>16</sup> Preparation of photocatalytic TiO<sub>2</sub> thin films can be synthesized from TiO<sub>2</sub> crystallites ranging from the nanometer to micrometer sizes. However, nanometer sized crystallites tend to agglomerate, often requiring a deagglomeration step. New application methods are focused on separating the nanoparticles without this deagglomeration step.<sup>50</sup> The two main application steps for the synthesis of TiO<sub>2</sub> films are through solution routes and gas phase methods.

### 1.8.1.1 *Solution routes*

Liquid phase processing is one of the most convenient and utilized methods for synthesis of TiO<sub>2</sub> thin films because of its ability to: control stoichiometry, produce homogeneous materials, form complex shapes, and prepare composite materials. However, long processing times, impurities, and high costs are some of the disadvantages of using solution routes.<sup>50</sup> The most commonly used solution routes in the synthesis of nano-TiO<sub>2</sub> are:

- Precipitation methods - Precipitation of hydroxides by the addition of a basic solution (NaOH, NH<sub>4</sub>OH, urea) followed by calcination to crystallize the oxide producing the anatase and/or rutile crystal structures.
- Sulfate Method – This utilizes a titanium oxysulfate (TiOSO<sub>4</sub>) solution produced by dissolving titanium minerals in sulfuric acid, neutralized with a base, to yield a hydrated titanium oxide. It is then calcined to form anatase or rutile crystal structure.<sup>51</sup>
- Chlorine Method – The reaction of titanium minerals and chlorine gas at elevated temperatures in order to thermally decompose titanium tetrachloride vapor. Degussa P-25 TiO<sub>2</sub>, a commonly used industrial TiO<sub>2</sub> nanopowder, is produced by this method.<sup>55</sup>
- Sol–gel methods. Utilized for the synthesis of thin films via dip or spin coating as a final step, through either an alkoxide route,<sup>56</sup> or non-alkoxide route<sup>57</sup>.

### 1.8.1.2 *Gas phase methods*

For TiO<sub>2</sub> thin films, most synthesis routes are performed using gas phase methods, as it enables control of temperature and pressure via a spray method in which titanium alkoxide and water are sprayed on a substrate heated to a desired temperature.<sup>39</sup>

- Chemical vapour deposition – A continuous process that coats large surface areas in a short time.<sup>58</sup>

- Physical vapour deposition – Films produced without a chemical transition from precursor to product formed from the gas phase, typically through thermal evaporation.<sup>50</sup>

Physical properties and photocatalytic activity of TiO<sub>2</sub>, for both physical and chemical vapour deposition methods, depend on the temperature of substrate, flow rate of carrier gas, and partial pressure of starting material in the system.<sup>39</sup>

Titanium dioxide can be coated on many different types of substrates including ceramics, glass, and polymeric substrates.

### 1.8.2 Ceramic Substrates

Traditional clear coatings for flooring and ceramics were designed using commercial grade raw materials of kaolin, feldspar, dolomite, whiting, wollastonite, corundum and/or quartz. Hupa et al studied the chemical resistance and cleanability of glazed surfaces using these materials, and found that the adhesion of soil on glazed surfaces and cleanability relies on the chemical and phase compositions, as well as surface roughness. Also surface degradation was found to create microscale holes that were difficult to clean by conventional cleaning methods.<sup>59</sup>

Kuisma et al studied glazed surfaces coated with functional layers in order to achieve soil-repelling properties as well as to enhance cleanability. The ZrO<sub>2</sub> and TiO<sub>2</sub> clear coatings were applied using a dip-coated sol-gel method, and decreased the soiling of most materials. The contact angle analysis showed that after cleaning, the contact angle increased, meaning that soiling was not completely cleaned. However, the study did not take into account the UV light exposure to the material to test the self-cleaning effects of TiO<sub>2</sub>.<sup>2</sup>

### 1.8.3 Glass Substrates

In 2001, Pilkington Glass announced the world's first commercially available, self-cleaning glass, Pilkington Activ™, composed of a nanocrystalline TiO<sub>2</sub> photocatalyst film (about 15 nm thick) that is a hard, thin, transparent, and mechanically-robust.<sup>16</sup>

Several other major glass companies released similar products, including PPG's Sunclean™.<sup>17</sup> Transparent self-cleaning TiO<sub>2</sub> films on glass substrates potentially have many practical applications in the automotive field such as mirrors<sup>60</sup>, window glasses, and windshields.<sup>61</sup>

As described above, there are two main methods in which TiO<sub>2</sub> films are deposited onto glass substrates: (a) sol-gel route, which can be easily wiped away from solid surfaces, and (b) on-line chemical vapour deposition. Activ™ films are applied to a hot substrate by an on-line chemical vapour deposition process, in which a hard, thin, transparent, mechanically-robust, photoactive coating of TiO<sub>2</sub> is affixed on glass.<sup>16</sup> To prevent alkaline metal ion migration from glass substrates to the deposited TiO<sub>2</sub> layer, most commercial glasses are coated with a SiO<sub>2</sub> blocking layer (approximately 30 nm thick).<sup>16</sup>

It was found by Guan<sup>1</sup> in 2005, that upon irradiation, the contact angle of a nano-layer of TiO<sub>2</sub> decreased almost to zero, thus achieving super-hydrophilicity. However, once the sample was placed in a dark area, the contact angle was restored back to its original state, at a fast rate. This lessens the efficiency of the photocatalytic coating for rainfall at night. The incorporation of SiO<sub>2</sub> to form a TiO<sub>2</sub>/SiO<sub>2</sub> composite films achieved a more efficient hydrophilic state during dark hours, and the photocatalysis reactivity of the coating also increased.<sup>1</sup>

It was shown by Mills et al<sup>16</sup> that the aforementioned photocatalytic layer demonstrated the removal of stearic acid, which was added as a model for dirt, to where no gas phase products other than CO<sub>2</sub> and H<sub>2</sub>O were generated during the course of the photocatalytic reaction. However, this photocatalytic reaction showed extremely slow reaction kinetics compared to that of a sol-gel produced layer of TiO<sub>2</sub>, as this glass glazed nano-layer achieved low light absorption at a wavelength of 365nm. The greater photocatalytic activity of the sol-gel films compared to Activ™ films upon irradiation was due mainly to the thickness of the TiO<sub>2</sub> layer. The sol-gel layer (90nm in thickness) comprised of large almost microcrystalline aggregates of TiO<sub>2</sub> gave lower recombination rates.<sup>16</sup> However, the effect of chemically absorbed charge carriers or chemically absorbed

organic species on the TiO<sub>2</sub> glazed glass was not explored. The incorporation of charge carrying species could potentially increase the photocatalytic reactivity for self-cleaning glass.

## **1.9 Polymeric Substrates**

### **1.9.1 Surface Chemistry of Nanoparticles in Polymeric Materials**

For nanotechnology and nanoparticles, the surface properties are important because as the particle size is reduced, the surface area to volume ratio increases. Nanoparticles tend to strongly agglomerate because the intermolecular attraction forces of the nanoparticles are high due to their large surface area, thus reducing the resulting mechanical properties of the nanocomposite materials.

The main types of molecular interactions between nanoparticles are: van der Waal forces (main attractive forces), electrostatic double layer forces (main repulsive forces), and acid-base interactions. These interactions can be positive or negative in nature, depending on the separation distance between the particles, the type of force, and the type of particulates used.<sup>24</sup>

### **1.9.2 Metal Oxide Functionalization**

Metal-oxide nanoparticles, in particular TiO<sub>2</sub>, can be used to optimize UV absorption and to enhance the stiffness, toughness, and service life of polymeric materials. They exhibit a diverse range of magnetic, electronic, and optical properties which can be utilized in many different applications. TiO<sub>2</sub> is traditionally used as whitening pigments to enhance the appearance and durability of many polymeric materials, including polyurethanes.<sup>62</sup>

Polymer systems are widely used due to their unique and advantageous attributes such as: ease of production, low cost, light weight, and often ductile nature. However, polymers have a lower modulus and strength as compared to metals and ceramics. One way to improve their mechanical properties is by reinforcement with fillers. The addition of ceramic material to a polymer matrix to form composites that enhance the material properties has been in practice for many years. These improvements have been realized

at low filler content as was seen in the work of Khaled et al. with TiO<sub>2</sub> nanofillers for bone cement applications.<sup>63</sup> Traditionally, composites were reinforced with micron sized fillers, but recently have been developed to nanoscale fillers. Generally, the material properties of a nano-composite material are superior to those of the micro-composite materials.<sup>64</sup>

Polymer composites reinforced with nanosized ceramic materials achieve greater mechanical properties than those using micron-sized particles.<sup>65</sup> However, flocculation and coagulation of these nanofillers causes decreased mechanical properties, due to creating gaps in the polymer matrix and therefore increasing the composites ability to move or flow with an applied stress. Therefore, aggregation of the particles must be prevented by increasing the repulsive forces between these nanofillers, where an energy barrier is created between the particles.

This energy barrier can be accomplished by many means; one method of keeping the nanoparticles separated is to coat the particles with polymer chains secured at one end to the nano surface. If the density of these chains is high enough, the chains extend from the surface to avoid overlapping one another, where the osmotic pressure between the two coated particles acts as a spring, providing the necessary repulsive force to keep the nanoparticles separated. Stable dispersions in various solvent systems can be prepared providing adequate polymer functionality with evenly spaced metal oxide materials within the matrix of the polymer. It is the length of the polymer chains that affects the final spacing of the nanoparticles in the film, meaning that the packing of nanoparticles can be controlled by controlling the polymer chain length. However, to effectively coat a nanoparticle, the polymer chains must be attached to the surface by either physical or chemical means.

#### *1.9.2.1 Physisorption*

Physisorption or physical adsorption is a type of adsorption where an adsorbate adheres to the surface through weak interactions; mainly van der Waals interactions and hydrogen bonding. In this type of adsorption, the chains are not strongly bound to the surface and

are easily displaced by solvation, increased temperature, or shear stress. In a polymeric material, one block or segment will have a greater affinity for the surface of the nanoparticle than other segments, where one segment will adsorb by physical means onto the surface, while the other block will extend into the solvent somewhat like a micelle. Physisorption is an equilibrium process in which changes in solvent and polymer concentrations change the number of polymer chains adsorbed per unit surface area. Also, physisorption is governed by many reversible processes, thus limiting the effectiveness for transforming surfaces with specific and complex polymer chains that can remain stable over a large range of conditions.

#### *1.9.2.2 Chemisorption*

Chemisorption is a type of adsorption where a molecule adheres to a surface through the formation of a covalent bond. This provides a strong anchoring of the polymer chains to the surface of the nanoparticle<sup>65</sup> and a functional platform for the development of complex structures. Covalent bonding between metal oxides and polymer substrates are accomplished mainly by the functionalization of a metal oxide surface with a specific organic group. For TiO<sub>2</sub>, a carboxylic acid derivative can be used to functionalize to the TiO<sub>2</sub> surface by coordination, with the other end available for polymerization.<sup>66</sup>

Two possible actions apply for functionalization: the functionalization of a block copolymer to the metal oxide nanoparticles, or the functionalization of an initiator to the nanoparticle then growing the polymer chain from this functionalized group.

### **1.10 Functionalization**

The inclusion of nano-fillers into the polymer matrix gives superior properties if the fillers are chemically bonded to the polymer, which requires functionalization. Functionalization of TiO<sub>2</sub> can occur by either polymer functionalization, or monomer functionalization method.

### 1.10.1 Polymer Functionalization

The functionalization of a polymer chain directly to the surface of a nanoparticle is deemed as a “grafting to” or the polymer approach. There have been several discoveries in the field of polymer functionalization, including the number of polymer chains that one can graft to the surface.<sup>67</sup> Normally this is very small because the free volume consumed by each grafted chain acts as a barrier to the attachment of additional polymer chains. Also, the rates of grafting reactions are dependant on the molar concentration of chain ends, and increasing this concentration makes the removal of the ungrafted chains from the system more difficult.<sup>68</sup>

Sathiyarayanan et al.<sup>69</sup> studied the functionalization of TiO<sub>2</sub> with polyaniline through chemical oxidation for a corrosion resistant, conductive polymer coating on steel. Their research showed increased corrosion protection with decreased resistivity, or increase conductivity compared to that of conventional aniline polymer coatings. Lin et al studied the formation of TiO<sub>2</sub>-silicone polymer composites<sup>21</sup> formed through the functionalization of silicone surfactant to the hydroxyl groups at the surface of the fine TiO<sub>2</sub> particles. It was found that the nano-TiO<sub>2</sub> particles were unable to escape from the film surface due to chemical bonding, which imparted good photodegradation resistance and antifouling properties to the composite.

### 1.10.2 Monomer Functionalization

In the “grafting from” or monomer method, an initiator is grafted to the surface of a nanoparticle, and the growing polymer chain then propagates outwards into the solution. The initiator is able to polymerize many monomers in solution or bulk polymerization. The monomer method is generally faster than the polymer method, as low molecular weight monomer molecules can diffuse rapidly to the surface of the nanoparticles, more easily than a polymer chain can.<sup>68</sup>

The dispersion of functionalized TiO<sub>2</sub> was found to increase using the monomer functionalization method compared to that of functionalizing the polymer itself.<sup>20, 53</sup>

Kim et al studied the functionalization of 2,2-bis[hydroxy oligo(3-caprolactone)methyl propionic acid, the same chemical formula as HMPA, a hard segment monomer option

for polyurethane synthesis, and polymerized poly(vinyl-chloride) (PVC). In this study, TiO<sub>2</sub> nanoparticles were incorporated with modified HMPA through a self-assembly process to form a HMPA–TiO<sub>2</sub> composite, avoiding massive agglomerates for the synthesis of degradable PVC.<sup>19</sup> Gao<sup>28</sup> claimed an increase in the collision possibility of pollutants with TiO<sub>2</sub> photocatalysts by supporting TiO<sub>2</sub> and activated carbon particles on silicone rubber films. The resulting immobilized TiO<sub>2</sub> had good crystallinity and powder size and the nearby activated carbon provided high concentrations of organic species around the TiO<sub>2</sub> particles, thus enhancing the rate of photo-oxidation. Losito et al synthesized a TiO<sub>2</sub>-poly(vinylidene fluoride) polymer composite material for the coating of glass substrates to be used for water purification of phenylurea herbicide (isoproturon). This material demonstrated an increased degradation rate of the pesticide compared to that of regular photolysis.<sup>70</sup> Although these methods have provided accelerated photodegradation in terms of cleanability, they have also been shown to increase the photodegradation of the polymer itself.

### 1.10.3 Photocatalytic Polymer Degradation

Historically, TiO<sub>2</sub> is used to prevent photodegradation of many polymers, but this is only true for the rutile crystal structure, not the anatase crystal structure. Anatase TiO<sub>2</sub> undergoes photodegradation more rapidly through photocatalysis, causing the breakdown of organic materials on the surface, along with some breakdown of the surface itself. Under UV irradiation, TiO<sub>2</sub> photocatalysts decompose organic contaminants into water and carbon dioxide. As polymers are also organic compounds, they can also be potentially broken down through photocatalytic degradation. When it comes to polymer based paints, this industrially-known effect is the phenomenon of “paint chalking”, where the organic components of the paint are decomposed as a result of photocatalytic processes. Compared with rutile and brookite, anatase shows the highest photoactivity, hence the TiO<sub>2</sub> in industrial products is almost exclusively of the rutile crystal type.

Light penetration into composite films is known to be a function of concentration, dispersity and size of TiO<sub>2</sub> particles in the polymer composites, as well as the thickness of the film itself. Shorter irradiation distances accelerate the photodegradation rate due to

the higher light intensity and thicker films having slower degradation rates.<sup>71</sup> It has been studied by Cho and Choi that light can penetrate the surface of a TiO<sub>2</sub>/PVC composite approximately 66 μm, but the concentration of TiO<sub>2</sub> within the sample had little effect on the penetration distance.<sup>53</sup> All polymeric materials exhibit this characteristic penetration, thus experiencing this degradation.

The photodegradation efficiency can be affected by size, shape, and agglomeration of TiO<sub>2</sub> particles. TiO<sub>2</sub> nanoparticles incorporated into the polymer matrix appear in the form of micron-sized agglomerates, and can significantly reduce the efficiency of photodegradation through two mechanisms: (a) decreasing the interface area between the polymer and photocatalyst; and (b) inducing rapid whitening that decreases the light penetration depth into the composite film. Increasing the dispersion of TiO<sub>2</sub> nanoparticles into the polymer matrix is expected to increase polymer degradation significantly.<sup>20</sup> Literature has proven that increasing the dispersion of TiO<sub>2</sub> nanoparticles in polymeric systems through functionalization can decrease the size of agglomerates, hence increasing the photocatalytic degradation efficiency.<sup>19</sup> This is because TiO<sub>2</sub> particles will aggregate significantly in a lower polar medium if there is not sufficient steric hindrance.<sup>20</sup>

Polymer photodegradation and cleanability have been studied in some polymer systems including polyethylene,<sup>72</sup> polystyrene,<sup>73</sup> poly(vinyl chloride),<sup>54</sup> and silicone rubber,<sup>21</sup> however, polyurethanes have not been studied.

### **1.11 Polyurethanes**

Polyurethanes are a collective group of polymers composed of a plethora of urethane (carbamate) linkages, as shown in Figure 3.4.

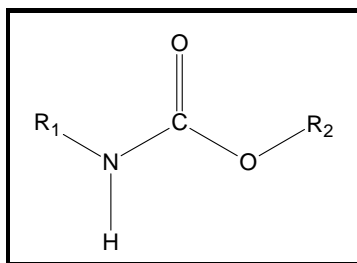


**Figure 0.4 - Urethane Linkage.**

Polyurethanes are produced by the polyaddition process of polyisocyanates reacted generally with polyalcohols that can be used to form a wide range of products including adhesives, coatings, elastomers, foams, and paints.

### 1.12 Polyurethane Elastomers:

To obtain PU elastomers with superior properties, the polyaddition reaction mixture usually contains three components, namely, a diisocyanate, a long-chain polyether or polyester polyol, and a short-chain diol (chain extender) forming segmented PU's. Segmented polyurethanes are block copolymers of the  $(AB)_n$  type, consisting of alternating sub segments, a soft segment and a hard segment. The soft segment consists of the long chain diol whereas the hard segment consists of the diisocyanate and chain extender as depicted in Figure 3.5. It is this phase segregation between the hard crystalline segment and the soft amorphous segment that is responsible for the unique physical and mechanical properties of polyurethanes.<sup>74</sup>

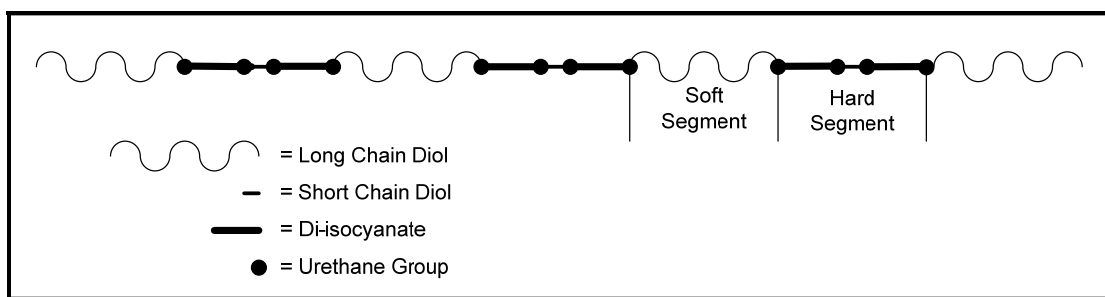


**Figure 0.5 - Schematic of Segmented Polyurethanes.**

Polyurethane elastomers are a two-phase structure, where the hard segments separate to form discrete domains in a matrix of soft segments. Hard segments significantly affect mechanical properties such as modulus, hardness, and tear strength. The performance of

elastomers at elevated temperatures is very dependant on the structure of the rigid segments and their ability to remain chemically linked at these temperatures. Rigid segments are considered to result from contributions of the di-isocyanate, typically: 4,4-methylene bis(p-phenyl isocyanate) (MDI) or 1,6-toluene diisocyanate (TDI), and chain extender, typically ethylene glycol or 1,4-butane glycol, components. The soft segment is typically a polyol, usually a liquid, that contain two isocyanate reacting groups attached to a single molecule. The majority of polyols are either hydroxyl-terminated or amino-terminated and have high molecular weights of approximately 1,000-6,500 Daltons for elastomeric coatings.<sup>75</sup> Polyether-based polyols, such as polytetramethylene etherglycol (PTMEG) also known as polytetrahydrofuran (PTHF), produce high quality polyurethane foams and elastomers. Chain extenders are typically low molecular weight diols or diamines.

#### 1.12.1 Polyurethane Chemistry:

Polyurethanes are block copolymers of either the non-segmented (Figure 3.6) or segmented variety (Figure 3.7) produced by the one-shot or prepolymer method respectively.

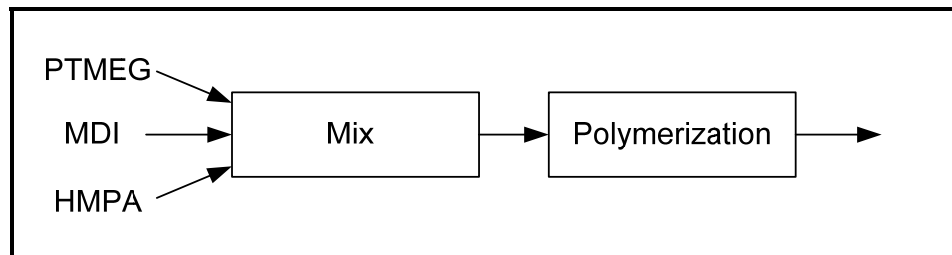


**Figure 0.6 - Synthesis of Non-Segmented Polyurethanes - One Shot Process.**

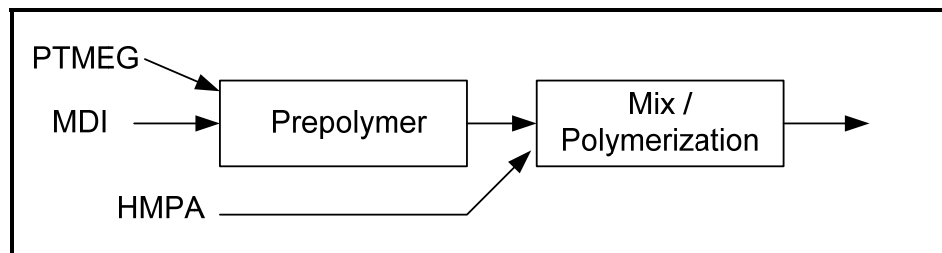


**Figure 0.7 - Synthesis of Segmented Polyurethanes - Prepolymer Method.**

The one-shot process depicts a di-polyalcohol (e.g. poly tetra methylene ether glycol (PTMEG)), a di-isocyanate (e.g. methylene di-isocyanate (MDI)), and a chain extender (e.g. 2,2-bis(hydroxymethyl)propionic acid (HMPA)) all mixed in a batch process to form a final polymer. The prepolymer method uses the same three reactants, but in a two step process in which a prepolymer consisting of the long chain diol and the diisocyanate is created first, then mixed with the chain extender.<sup>75</sup>

### 1.12.2 Bonding Properties

It is the secondary bonding forces acting between different molecules in the polymer chains that contribute to the unique properties of polyurethanes. These forces are classified as van der Waals forces, dipole interaction, and hydrogen bonding and are much weaker forces than covalent bonds. However, they directly affect the polymer's physical properties, such as viscosity, surface tension, frictional forces, miscibility, and solubility.

Ionic and coordination bonds are other types of forces that can contribute to polyurethanes. Functionalized TiO<sub>2</sub> is formed through coordination bonding that can help link the chains together making the coating stronger.<sup>75</sup>

## EXPERIMENTAL SECTION

### 1.13 Materials

All chemicals were purchased from Sigma-Aldrich (Mississauga, ON). 4,4-methylene bis(p-phenyl isocyanate) (MDI) was purified using hot filtration of the melt with Whatman 50 filter papers at a temperature of 65°C under vacuum. Poly(tetrahydrofuran) (PTHF) with an average molecular weight of 1000 Daltons was heated at 90°C under vacuum to remove all moisture. 2,2-bis(hydroxymethyl)propionic acid (HMPA) was washed and filtered under vacuum with distilled reagent plus methanol, and recrystallized under vacuum at 70°C.

Titanium (IV) oxide nanopowder (TiO<sub>2</sub>) with an average particle size of 25 nm at 99.9% purity, comprised of 50% anatase and 50% rutile crystal forms, Toluene anhydrous, 99.8%, dimethylformamide (DMF) ACS reagent, ≥99.8%, and tetrahydrofuran (THF) anhydrous, ≥99.9%, inhibitor-free were all used as prepared by Sigma Aldrich.

### 1.14 Polyurethane Elastomer Synthesis

#### 1.14.1 Experimental Setup

The polyurethane (PU) synthesis experimental setup is shown in Figure 4.1, where a three-necked flask was used to: a) mix the solvents, reactants and products during polymerization; b) measure the temperature of the mixture; and c) provide a purge stream of nitrogen to avoid any entrained moisture in the air that could quench the reaction. All of the glassware was dried in an oven at 120°C prior to use. A Fuji electronic temperature controller was used with fuzzy logic to control the temperature of the reaction, typically between 80-85 °C.

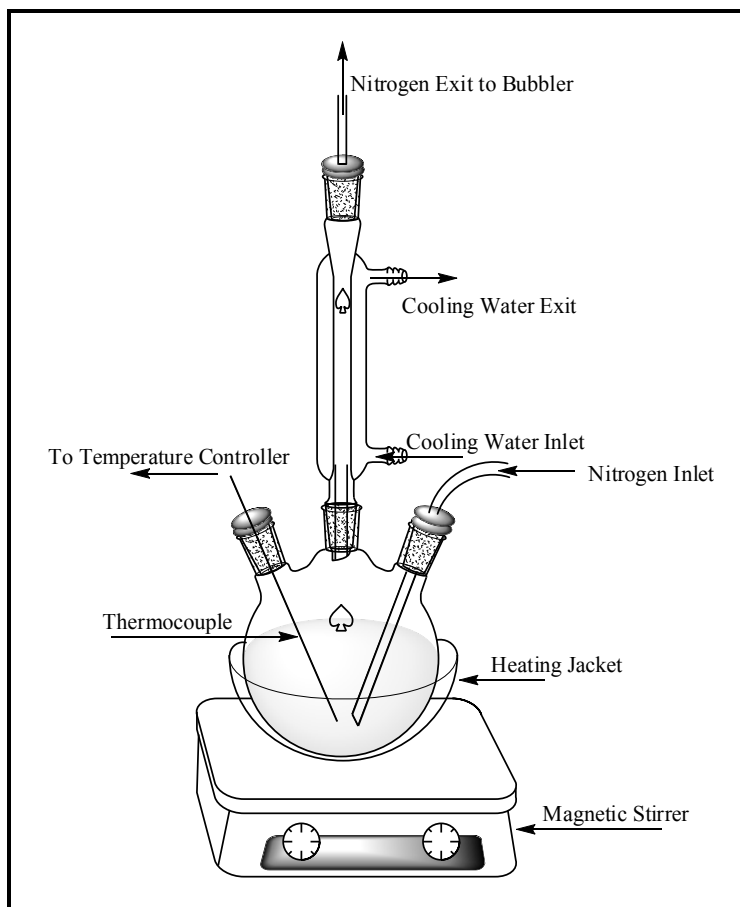


**Figure 0.1 – Polyurethane Laboratory Setup.**

#### 1.14.2 Polyurethane Synthesis

The segmented polyurethane coatings were synthesized using MDI and HMPA for the hard segment, and PTHF for the soft segment. This synthesis took place as a two step reaction in DMF and Toluene at 85°C for prepolymerization, and then polymerized with HMPA.

For the prepolymerization, MDI was reacted with PTHF at a molar ratio of 2:1 under nitrogen gas and solvent at 85°C for 2 hours and was constantly mixed by a magnetic stirring. Due to the long organic chain length of PTHF and its insolubility in most oxygenated solvents, a mixture of DMF/toluene at a 1:1 volume ratio was used as the reaction medium. The said prepolymer was then polymerized at a 1:1 molar ratio with a chain extender, HMPA for 2 hours.<sup>76</sup>

The synthesized polyurethane was then mixed with a varying amount of nano-TiO<sub>2</sub>; either 0wt%, 5wt%, or 10wt% TiO<sub>2</sub> in a mixture of PU, Toluene/DMF at 85 °C for 12 hours for polymer functionalization.

The polyurethanes were then poured into a methanol solution in a 10:1 methanol to DMF/toluene (v/v) ratio at room temperature and stirred; thus quenching the reaction and dissolving the short chain oligomers, such that the polymer yield could be associated with reasonably high molecular weight polymers. The solution was then filtered in a Buchner funnel, with the remaining polyurethane elastomer being placed on a Teflon plate, then dried under vacuum at 85°C for 24 hours.

#### 1.14.3 Monomer Functionalization Synthesis

In this method, the as received 50-50% anatase-rutile titania nanospheres were reacted in different percentages so that the final polymerization percentages of TiO<sub>2</sub> by mass were 2.5%, 5%, and 10%. To functionalize the nanospheres, nanotitania powder was dispersed in 100 mL of 2-propanol with the aid of ultrasonic agitation with 5g of HMPA at 82°C under constant agitation and nitrogen gas for 12 h. The final polymers were purified by methanol washing and poured onto a Teflon plate and heated at 80°C for 12 h under vacuum.<sup>63</sup>

The functionalized HMPA was then reacted using the same synthesis procedure mentioned in section 4.2.2., where it was added with the prepolymer as a chain extender. However, TiO<sub>2</sub> is insoluble in every solvent, therefore, an increased reaction time of 4 h was required. This reaction led to the functionalized polyurethanes of varying TiO<sub>2</sub> content.

### **1.15 Characterization Methods**

Many characterization methods were used for TiO<sub>2</sub>-PU composite analysis.

### 1.15.1 Fourier Transform Infrared Spectroscopy

Fourier Transform Infrared (FTIR) spectroscopy was used to identify the characteristic functional groups of the polyurethane elastomers, as well as the cleanability study in cleaning excess HMPA from the surface of PU-TiO<sub>2</sub> composites. FTIR analysis was also used for examining the functional peaks of coordinated carboxylate groups to TiO<sub>2</sub>. FTIR analysis was performed using a Bruker<sup>®</sup> Vector 22 spectrometer for solid polyurethane samples. The aforementioned spectrometer provided spectra in the range of 400– 4000cm<sup>-1</sup> and was operated using 32 scans at 4cm<sup>-1</sup> resolution for each sample film.

### 1.15.2 In situ Fourier Transform Infrared Spectroscopy

In situ FTIR was used to identify the characteristic functional groups of the HMPA functionalization in order to determine the kinetic parameters of coordination of HMPA-TiO<sub>2</sub> for specific reaction conditions (T = 82°C, P = 1atm, R=300rpm) and for a given composition of HMPA to TiO<sub>2</sub>, 0.660g and 0.405g respectively. In situ FTIR analysis was performed using a Metler Toledo<sup>®</sup> ReactIR 4000 spectrometer in a 100mL reactor where the spectrometer provided spectra in the range of 400 – 4000cm<sup>-1</sup> and was operated using 32 scans at 4cm<sup>-1</sup> resolution for each reaction time sequence of 1 hour intervals.

### 1.15.3 Thermo-Gravimetric Analysis

A Thermo-Gravimetric Analyzer (TGA) was used to: a) identify the characteristic hard and soft segments of the polyurethane elastomers, b) determine the degree of TiO<sub>2</sub> coordination to HMPA at different compositions, and c) study the effects of photodegradation of the polyurethane composite samples. TGA analysis was performed using a TA Instruments<sup>®</sup> Q-series TGA Q500 analyzer and the spectra were analyzed using TA Instruments<sup>®</sup> Universal Analysis 2000 software. The aforementioned analyzer provided spectra in the temperature range of 25 – 700°C at a constant heating rate of 20°C/min for sample sizes ranging from 5 - 10mg.

### 1.15.4 Atomic Force Microscopy

Atomic Force Microscopy (AFM) was used to visualize the surface topography and surface roughness of the composite samples. AFM was performed using an Agilent

5500™ AFM/SPM microscope in intermittent contact mode. All samples were taken at 1.9V for a 20x20µm scanning area.

#### 1.15.5 Scanning Electron Microscopy

Scanning Electron Microscopy (SEM) was used to see the morphology of HMPA and the functionalization of HMPA to TiO<sub>2</sub>. SEM was performed using a Hitachi® S-2600N Scanning Electron Microscope after each sample was gold sputtered using a EMITCH® K550X deposited at 15 mA/min for 90 seconds to achieve a 5-7nm gold layer. All samples were taken at 5 kV at varying magnifications for different views. For full scale views, the magnification was taken at 350x and for the close up images, the magnification was 2500x and 4000x for HMPA and Ti-HMPA respectively.

#### 1.15.6 Energy Dispersive X-ray Detection

Energy Dispersive X-ray (EDX) Detection was used to determine the approximate fractions of TiO<sub>2</sub> on the surface of PU composite coatings, and to measure the dispersion of TiO<sub>2</sub> within each sample. EDX measurements were performed using a Quartz Xone EDX scattering device attached to the Hitachi® S-2600N Scanning Electron Microscope after each sample was gold sputtered using the aforementioned technique.

#### 1.15.7 Contact Angle Characterization

Hydrophilic and hydrophobic behavior was evaluated by measuring the contact angle of a water droplet on the films under an ambient condition of 20°C in air atmosphere using the sessile-drop method. A droplet was dropped on the surface using a micro-injector from a distance of 1cm from the surface. Assuming spherical geometry of the sessile drop, the static contact angle was estimated by manual measurements at the vapor-liquid-solid interface using a reading microscope.

#### 1.15.8 Characterization of self-cleaning photocatalytic properties

The self-cleaning photocatalytic properties of the films were evaluated by examining the oxidation and reduction reactions of excess HMPA on the surface of the functionalized polyurethane films under UV irradiation. The samples were dissolved in 50mL of THF and 20% HMPA, then poured onto a Teflon plate and dried under vacuum at 65°C for 24

hours. The samples were then irradiated perpendicular to the light source, at a constant distance of 10cm with a 20 W black light bulb. The UV intensity irradiated to the sample surface was given to be  $0.8\text{mW}/\text{cm}^2$  at the said distance using a  $365\pm 20$  nm UV light source (model B100AP; UVP Inc.). During irradiation, air at room temperature was allowed to flow around the sample and the elimination of HMPA from the surface was determined using FTIR analysis.

#### 1.15.9 Characterization of self-cleaning degradable PU-TiO<sub>2</sub> composite coatings

Photocatalysis degradation experiments were performed on mostly TiO<sub>2</sub> functionalized polyurethane elastomeric coatings with varying amounts of TiO<sub>2</sub>, 0, 5, and 10% by mass. The sample thicknesses for all samples were between 90-100 $\mu\text{m}$  controlled using a constant surface area Teflon plate for a constant mass of 1.0g.

#### 1.15.10 Statistical Analysis

All available data was statistically analyzed using two way analysis of variance (ANOVA) for a 95% confidence level by Sigma Plot software, version 9.

## RESULTS - CHEMISTRY

### 1.16 Polyurethane Synthesis

Multiple polyurethane samples with varying  $-NCO$  and  $-OH$  ratios were successfully synthesized in solution using the prepolymer method (Figure 3.7) with MDI and PTHF for the prepolymer, and HMPA to synthesize the final polymer. According to Szycher,<sup>75</sup> the optimal molar ratio between di-isocyanate groups and di-alcohol groups for polymerization is between 1.00:1.00 – 1.00:1.05 NCO groups to OH groups. Figure 5.1 shows that the PU was optimized at this ratio corresponding to polymer yield, after liquid-liquid extraction.

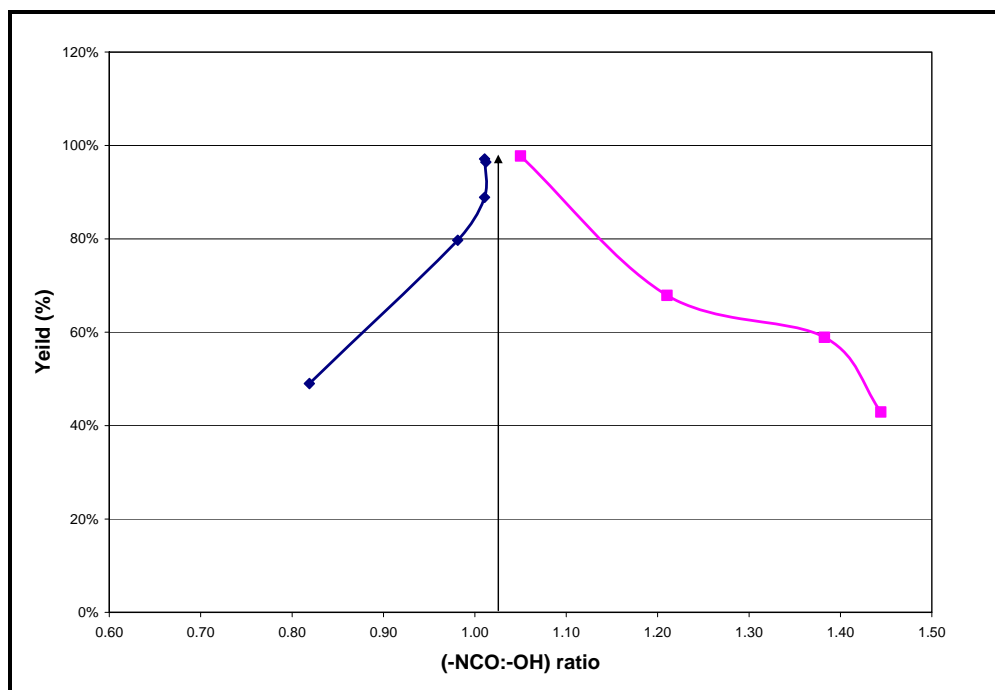


**Figure 0.1 - Polyurethane Optimization for Varying ratio of NCO:OH groups.**

A maximum yield was achieved with an OH:NCO ratio as previously mentioned. In order to synthesize a A-B type segmented polymer as seen in Figure 5.2, the PU was synthesized using a molar ratio of PTHF:MDI of 1:2 (mol/mol) forming a polyurethane prepolymer, and then reacting this prepolymer with HMPA in a 1:1 molar ratio.

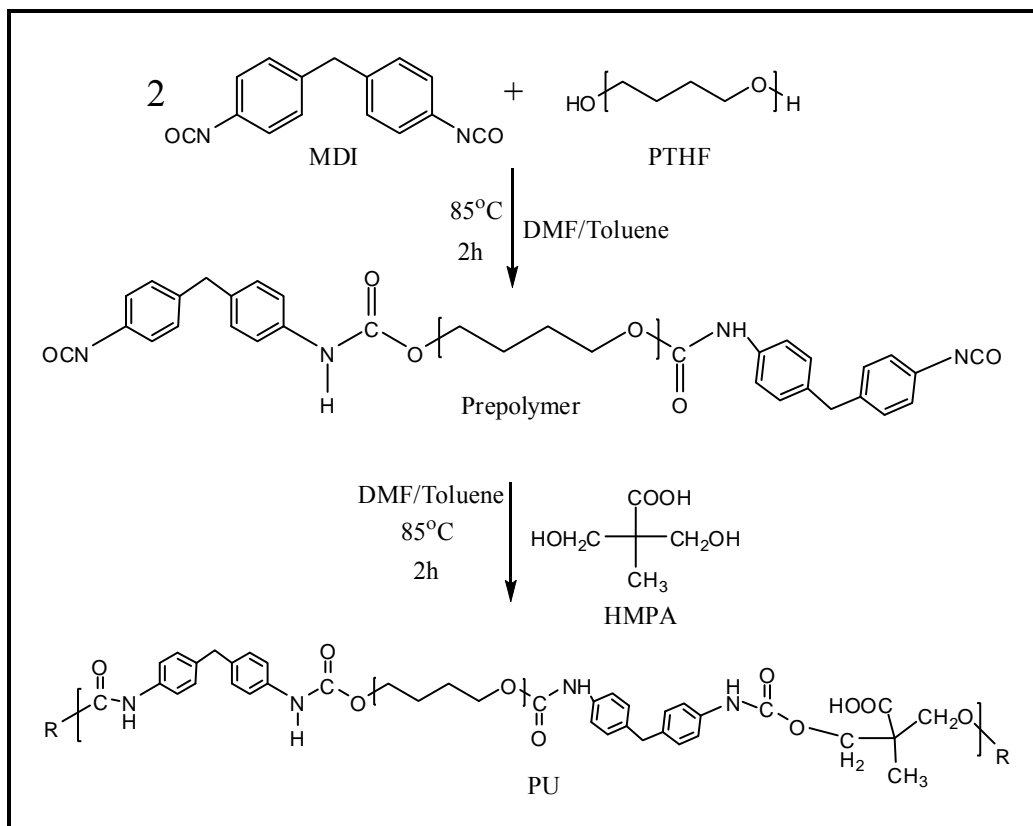
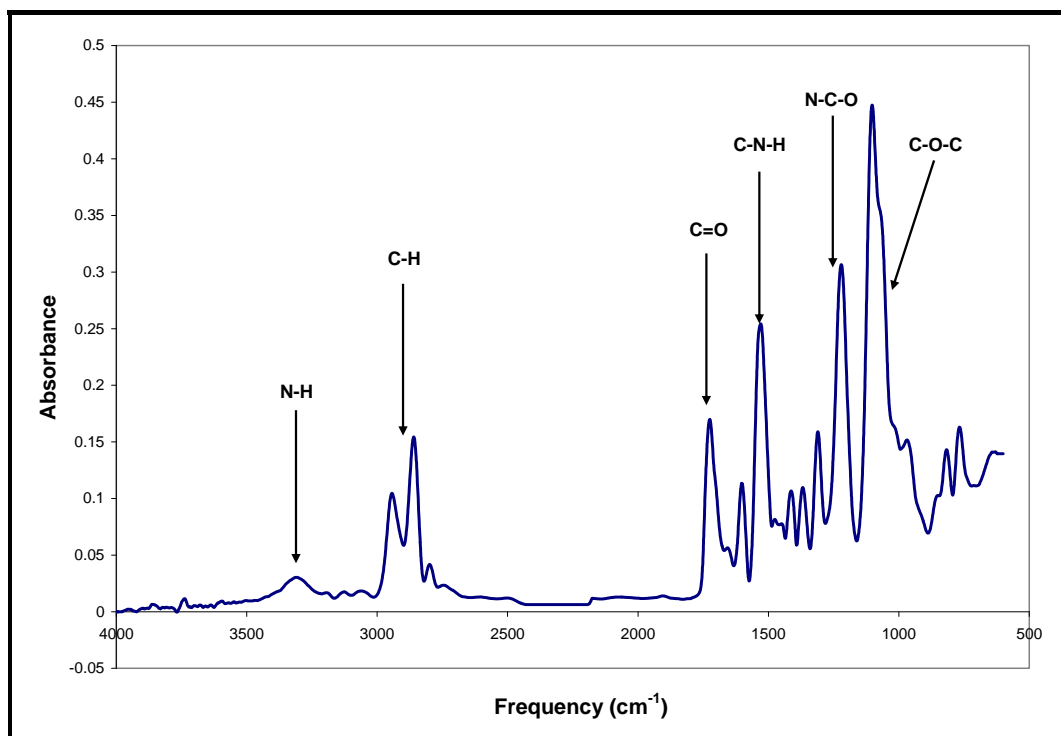


Figure 0.2 – Segmented Polyurethane Elastomer Synthesis.

### 1.17 Fourier Transform Infrared Spectroscopy of Optimized Polyurethanes

Polyurethanes have many characteristic peaks which are outlined in Table 5.1. The FTIR spectrum for an optimized PU elastomer is shown in Figure 5.3, where all anticipated peaks were detected, and are shown on the spectrum. The characteristic NH peak at  $3350\text{cm}^{-1}$ , and the carbonyl peak at  $1710\text{cm}^{-1}$  are characteristic urethane linkage peaks, and also the non existent isocyanate peak at  $2265\text{cm}^{-1}$  all prove that the polyurethane shown in Figure 5.2 was formed.<sup>77</sup> The spectrum for the prepolymer was not measured because the -NCO end groups react once introduced to humid air to form an aldehyde end group.



**Figure 0.3 - FTIR Spectrum for optimized polyurethane elastomeric coating.**

**Table 0.1 – Characteristic FTIR absorption frequencies in polyurethanes.**

Functional Group	Absorption Frequency Range (cm <sup>-1</sup> )
NH	3300-3500
OH (Alcohols)	3000-3600
OH (Carboxylic Acids)	2500-3000
CH	2800-3000
C=O	1680-1750
C-N-H	1500-1600
N-C=O	1250-1300
C-O-C	1050-1300

## 1.18 Monomer Functionalization

In the functionalization of 2,2 bis(hydroxymethyl) propionic acid (HMPA) with TiO<sub>2</sub> nanopowder, a new functionalized monomer, termed Ti-HMPA, was synthesized as seen in Figure 5.4.

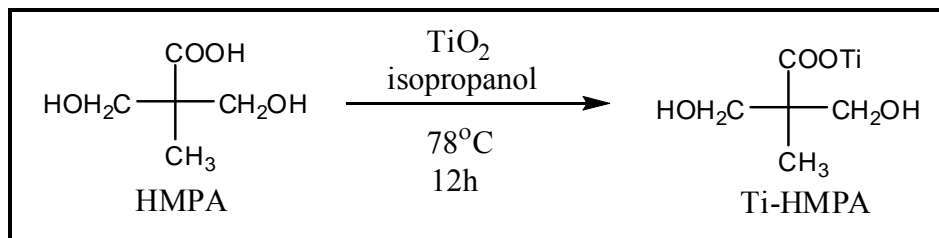


Figure 0.4 - HMPA Functionalization Synthesis.

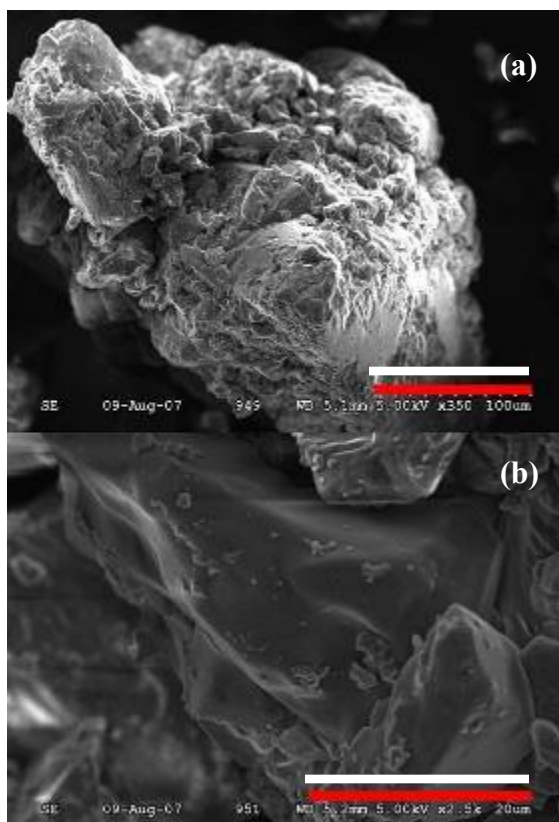
Figure 5.5 shows digital visualization of HMPA before and after functionalization, which transforms from a white powder to a yellowish crystalline powder after functionalization (Ti-HMPA).



Figure 0.5 – Digital Imaging of Crystal Color Change of HMPA (left) and Ti-HMPA (right).

### 1.18.1 Scanning Electron Microscopy Imaging

In order to examine the microstructure of the Ti-HMPA, SEM analysis was conducted. Figures 5.6a and 5.6b show the SEM micrographs of the agglomerated crystal structure of HMPA in two different scales, 100 $\mu\text{m}$  and 20 $\mu\text{m}$ , respectively.



**Figure 0.6 – SEM Images of HMPA (a) 100 $\mu$ m Scale (b) 20 $\mu$ m Scale**

Figures 5.7a and 5.7b show the Ti-HMPA crystals at two different magnification scales. The SEM micrographs show that the crystal morphology of HMPA changes from that of a block crystal to rod shape agglomerate crystals with agglomerated nano-TiO<sub>2</sub> functionalized to the surface of HMPA. Also, the HMPA crystal size decreases when formed into Ti-HMPA. This is due to HMPA having three hydrogen-bonding sites (two alcohol groups and one carboxylic acid group), whereas after functionalization, the carboxylic acid group changes to a titania functionalized carboxylate, decreasing the amount of hydrogen bonding between the HMPA crystals. However, TiO<sub>2</sub> agglomerates have the ability to bond two crystals together, leading to agglomerates of Ti-HMPA rod-shaped crystals as seen in Figure 5.7.

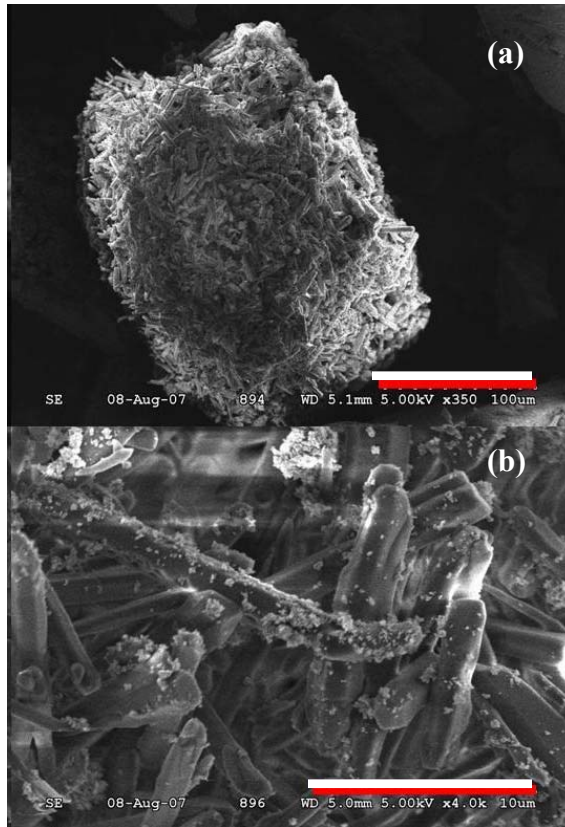


**Figure 0.7 - SEM Images of Ti-HMPA (a) 100 $\mu$ m Scale (b) 10 $\mu$ m Scale**

In addition, it is observable from Figure 5.7b, that the nano-TiO<sub>2</sub> is reasonably well dispersed throughout the HMPA crystals, although some TiO<sub>2</sub> agglomerates less than 1 $\mu$ m are still evident.

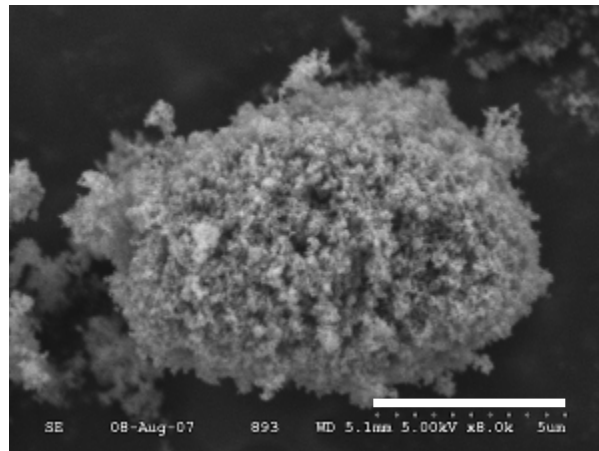


**Figure 0.8 - SEM Image of a Nano-TiO<sub>2</sub> Agglomerate. 5 $\mu$ m Scale.**

Figure 5.8 shows a nano-TiO<sub>2</sub> agglomerate of 5-10µm not functionalized to HMPA. It is evident when comparing Figure 5.7b to Figure 5.8, that the functionalization of nano-TiO<sub>2</sub> to HMPA decreases agglomeration.

### 1.18.2 FTIR analysis

FTIR analysis in Figure 5.9 was used to show the specific characterization peaks for: (a) n-TiO<sub>2</sub>, (b) HMPA, and (c) Ti-HMPA. The Ti-HMPA trace shows that the peaks at 1710cm<sup>-1</sup>(C=O peaks), 1250cm<sup>-1</sup> and 1050cm<sup>-1</sup>(both C-O peaks) decrease, indicating that a reaction has taken place. The C=O bonds and C-O peaks associated with the carboxylic acid group of HMPA are replaced with a conjugated carboxylate group as seen in Figure 5.4 for Ti-HMPA.

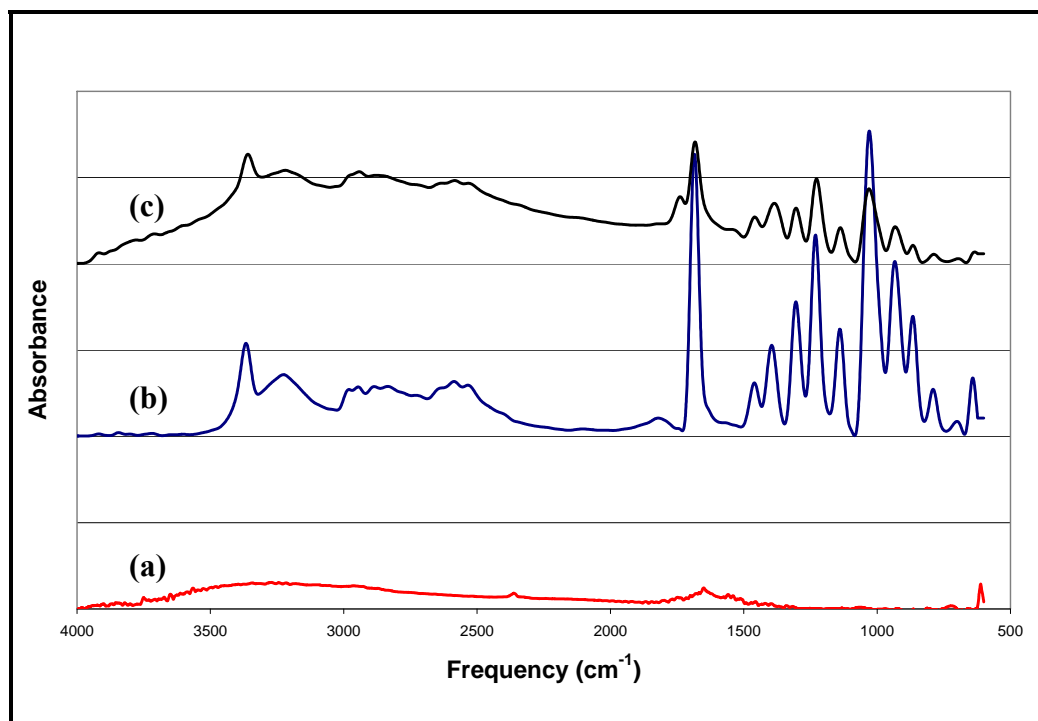


**Figure 0.9 – FTIR Peaks for (a) TiO<sub>2</sub> (b) HMPA (c) Ti-HMPA.**

The carboxylates coordinated to the titania surface are functionalized via three possible chemical structures as seen in Figure 5.10: (a) chelating bidentate, (b) bridging bidentate and (c) monodentate.<sup>78</sup> Figure 5.11 shows the FTIR results for Ti-HMPA, where three Ti functionalization peaks between 1350cm<sup>-1</sup> and 1550cm<sup>-1</sup> are present. These peaks are

similar to that of many groups: Khaled et al.,<sup>63</sup> Mao et al.,<sup>79</sup> Hojjati et al.,<sup>80</sup> although slightly shifted, as the acetate coordination to TiO<sub>2</sub> will change in different chemical environments, causing shifting of the acetate peaks.<sup>63, 80</sup> The remaining carboxylic acid peak for HMPA at 1707cm<sup>-1</sup> indicates that not all of the HMPA monomer was functionalized.

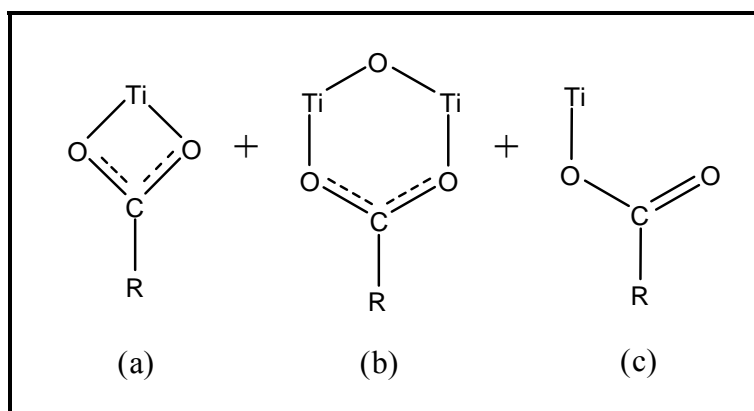


**Figure 0.10 - Binding Modes of RCOO<sup>-</sup> with Titania Surface: (a) Chelating Bidentate, (b) Bridging Bidentate, and (c) Monodentate.**

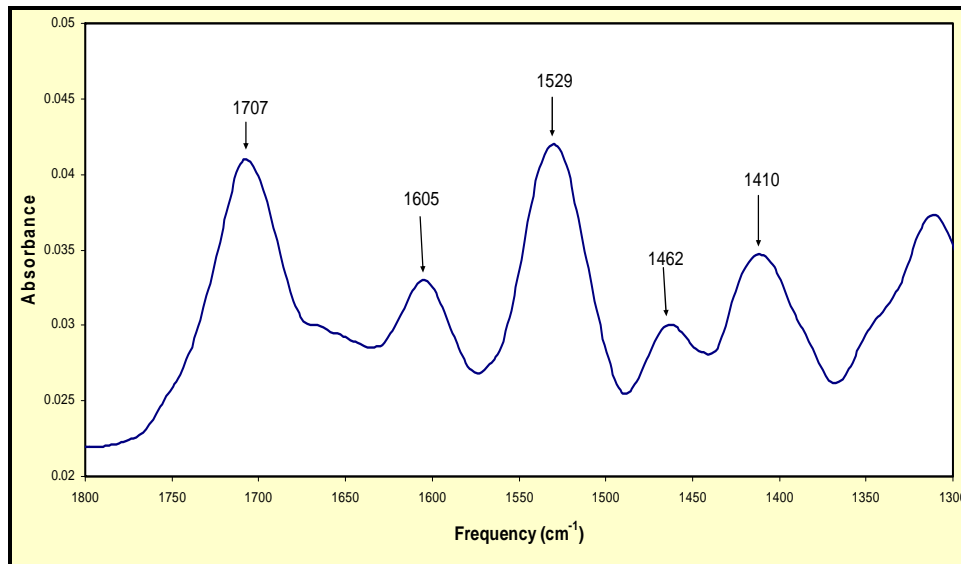


**Figure 0.11 – FTIR Results for TiO<sub>2</sub> Coordination Peaks.**

### 1.18.3 In situ FTIR analysis

The chemical structures of HMPA and HMPA/n-TiO<sub>2</sub> monomer were also characterized using in situ FTIR spectroscopy, as shown in Figure 5.12 and Figure 5.13, to reveal

chemical functionalization as a function of time. Figure 5.12 shows the lower IR spectrum range (1800-1000 $\text{cm}^{-1}$ ) of HMPA converting into the HMPA/n-TiO<sub>2</sub> monomer for 0-24 hours. The characteristic peak at 1708 $\text{cm}^{-1}$  for the carbonyl group (C=O) stretch and the C-O peak at 1045 $\text{cm}^{-1}$  in HMPA both decrease over a reaction time of 12 hours. This indicates that the functionalization of HMPA has removed the C=O group and the C-O group, and replaced it with a 1.5 bonds as seen in Figure 5.4 by the (a) chelating bidentate and (c) bridging bidentate forms of functionalization. However, the acetate peaks are not observed in the in situ reaction due to their small absorptions, but the peak changes at 1410 $\text{cm}^{-1}$  and 1470 $\text{cm}^{-1}$  indicate some changes in the titanium coordination peaks, further demonstrating functionalization.

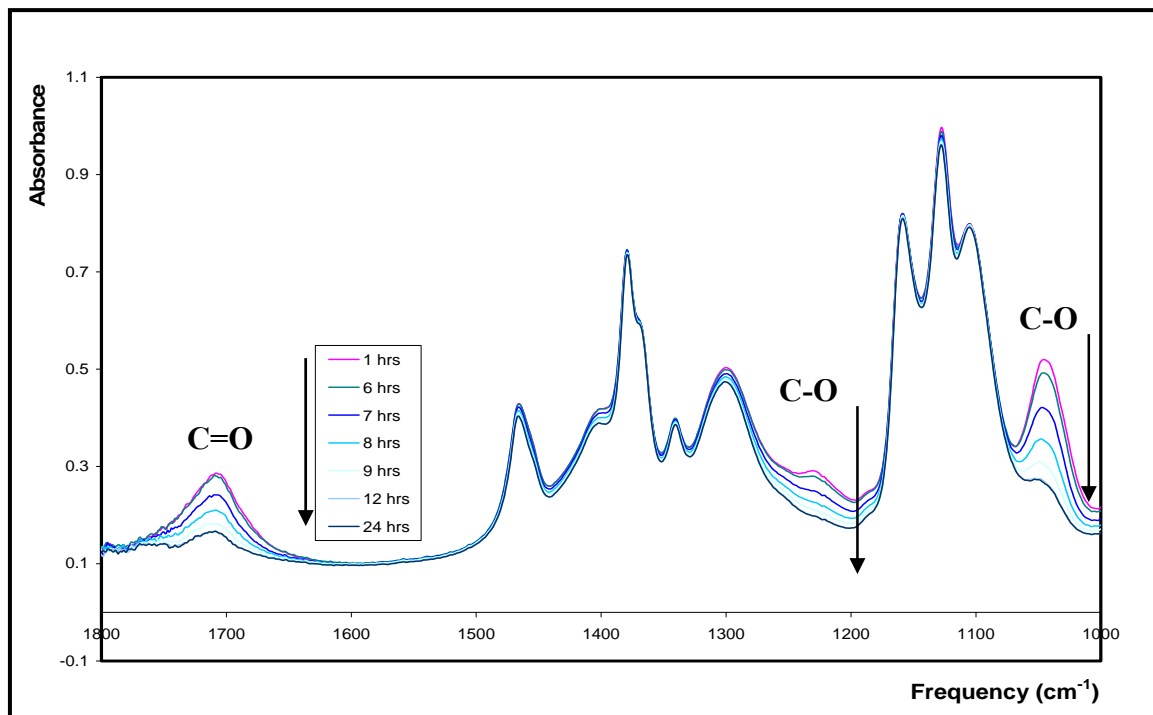


**Figure 0.12 – In Situ Results for HMPA Functionalization – CO Range.**

The percentage of functionalization was calculated to be approximately 60 - 64.5% using the in situ FTIR peak area. Figure 5.13 shows the upper IR spectrum range of HMPA converting into the HMPA/n-TiO<sub>2</sub> monomer, where the region from 2500 - 3000 $\text{cm}^{-1}$  decreased uniformly, indicating that the alcohol group (OH) from a carboxylic acid decreased, and also signifying functionalization. However, the C-H peak at 2970 $\text{cm}^{-1}$

does not change because the solvent peaks for 2-propanol disguises the carboxylic acid OH decrease. This figure also shows that the OH peak from the di-alcohol from 3000 - 3500 $\text{cm}^{-1}$  does not change, showing that further reactions with the OH groups can occur, a requirement for the Ti-HMPA monomer to be used in subsequent nanocomposite synthesis.

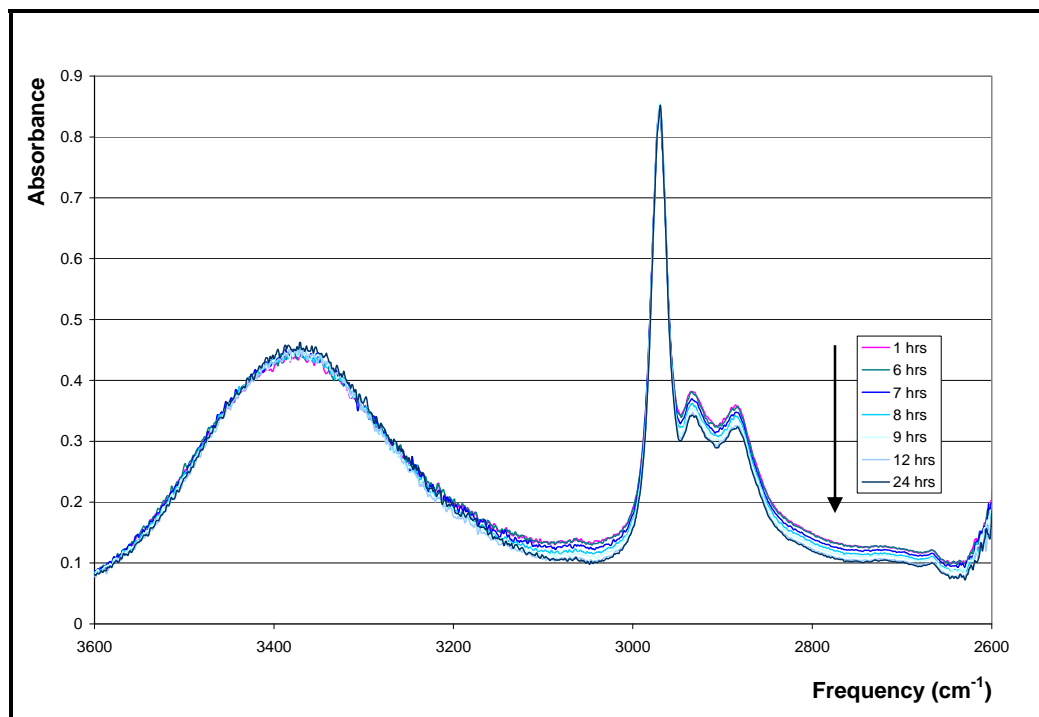


**Figure 0.13 - In Situ Results for HMPA Functionalization – OH Range.**

#### 1.18.4 In situ FTIR Functionalization Kinetic Behavior

Since the in situ FTIR data was recorded with time, a kinetic study for functionalization of HMPA and n-TiO<sub>2</sub> can be determined. The data for the kinetic study is seen in Table A.1 and Table A.2 in the Appendix. From this data, the coordination reaction can be examined using first order kinetics, as described by:

$$\frac{d[M]}{dt} = r = -k[M] \quad \mathbf{0.1}$$

Figure 5.14 graphs the kinetic data as a first order set of data, in which the logarithm of the initial HMPA ( $[M_0]$ ) concentration over the actual HMPA concentration ( $[M]$ ) versus time is plotted. The two peaks at  $1050\text{cm}^{-1}$  and  $1710\text{cm}^{-1}$  differ slightly, but this can be associated with the FTIR systematic error, in which the data from one peak is constantly higher than the data from the second peak.

From Figure 5.14, the overall reaction takes approximately 10 hours to completion, including a lag time of approximately 5 hours. This lag time is attributed to the crystal restructure of HMPA as seen in the SEM images in Figure 5.6 and Figure 5.7, in which the three dimensional hydrogen bonding of the HMPA crystals needs to be broken, before the functionalization reaction can begin.

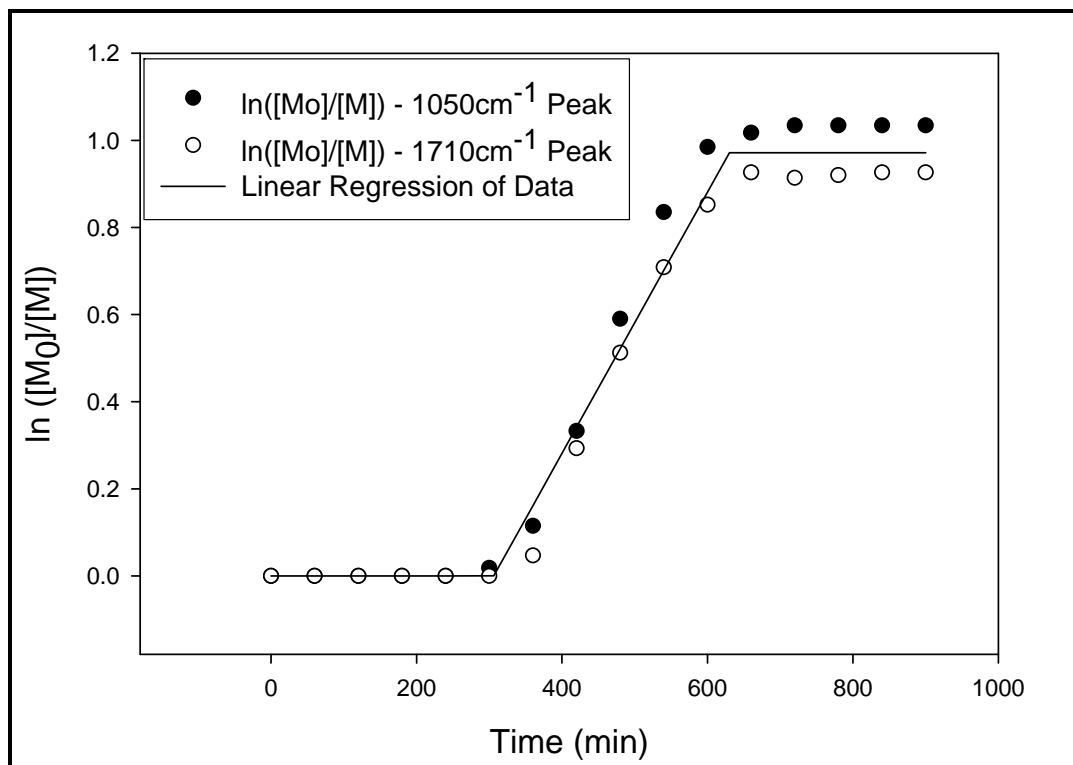
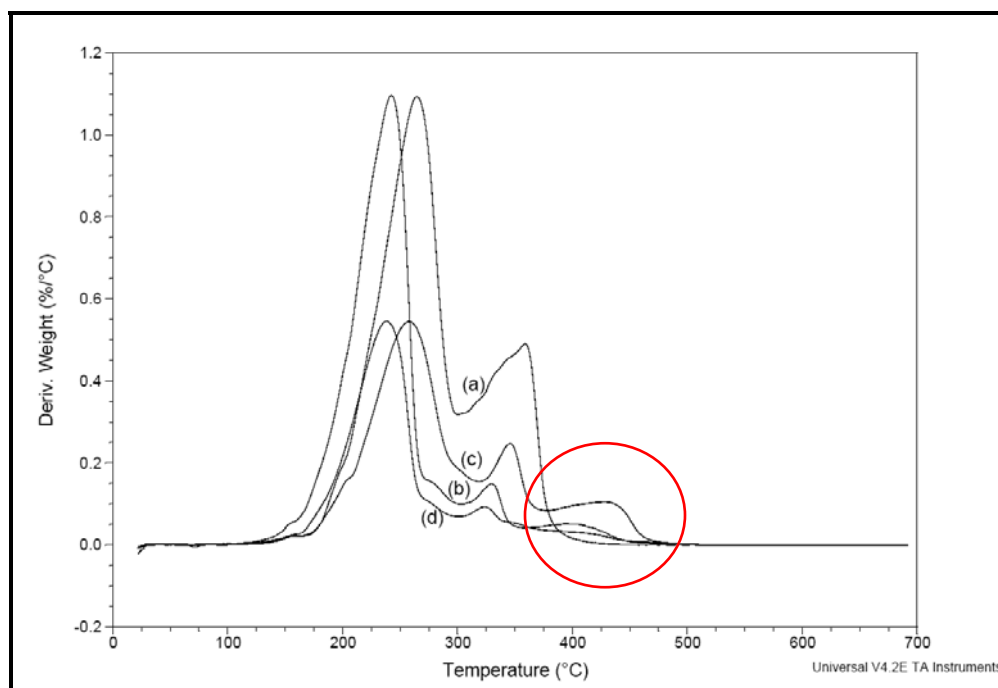


Figure 0.14 – Kinetic Data for  $\text{TiO}_2$ -HMPA Functionalization.

### 1.18.5 TGA Analysis

TGA analysis was also conducted on the Ti-HMPA monomer to further demonstrate functionalization of Ti to HMPA, and how thermal decomposition changes upon functionalization. Figure 5.15 and Figure 5.16 contain the derivative thermogravimetric (DTG) plot and thermogravimetric (TG) plot, respectively, for varying the wt% TiO<sub>2</sub>-HMPA functionalized monomer. HMPA thermal oxidation degradation is broken into two parts as seen in Figure 5.15(a): the decomposition of alcohols and carboxylic acids which begins at approximately 172°C,<sup>56, 81</sup> and the decomposition of the remaining oxidized carbon chain that starts at approximately 293 °C. It is noticed that upon functionalization, a third step of thermal decomposition that begins at approximately 350-370°C, as shown in curves (b), (c), and (d). The third peak in these curves represents the functionalized carboxylate groups chemically bonded to TiO<sub>2</sub>. It is also observed that there is not a linear trend for functionalization. This is possibly due to a maximum functionalization for a given percentage of TiO<sub>2</sub> compared to HMPA, or most likely due to the change in concentration of TiO<sub>2</sub>, because the volume of solvent and mass of HMPA remained constant for each reaction.



**Figure 0.15 -HMPA and Ti-HMPA DTG Curves for (a) 0% TiO<sub>2</sub> (b) 23.6% TiO<sub>2</sub> (c) 38.2% TiO<sub>2</sub> (d) 55.3% TiO<sub>2</sub>. Functionalization for Curves (b), (c), and (d) are Circled.**

To further quantify the DTG and TG plots, the two characteristic temperatures for each peak: the initial temperature of decomposition ( $T_i$ ), and the temperature maximum degradation ( $T_i^{\max}$ ), are provided in Table 5.2. These thermal degradation values are outlined in Table 5.2 where HMPA is the degradation associated with the unfunctionalized monomer, Ti-HMPA corresponds to the functionalized monomer, and Ti-HMPA\* is calculated for the adjusted mass values of the three segments when the mass of  $\text{TiO}_2$  is not included. The TG curves in Figure 5.16 show increasing  $\text{TiO}_2$  peaks from 0-55.3%  $\text{TiO}_2$ . It is also evident that the initial decomposition temperature ( $T_i$ ) decreases from 172.7°C for HMPA to 161.8°C for a 23.6%  $\text{TiO}_2$  Ti-HMPA monomer. This is due to the loss of hydrogen bonding between the individual monomer molecules. However, as the % $\text{TiO}_2$  increases, the initial decomposition temperature also increases from 161.8°C for 23.6%  $\text{TiO}_2$  Ti-HMPA monomer to 168.1°C for 55.3%  $\text{TiO}_2$  Ti-HMPA monomer, due to increased ionic stabilization between HMPA and  $\text{TiO}_2$ . This trend was also observed for the functionalization of  $\text{TiO}_2$  to methacrylic acid.<sup>63</sup>

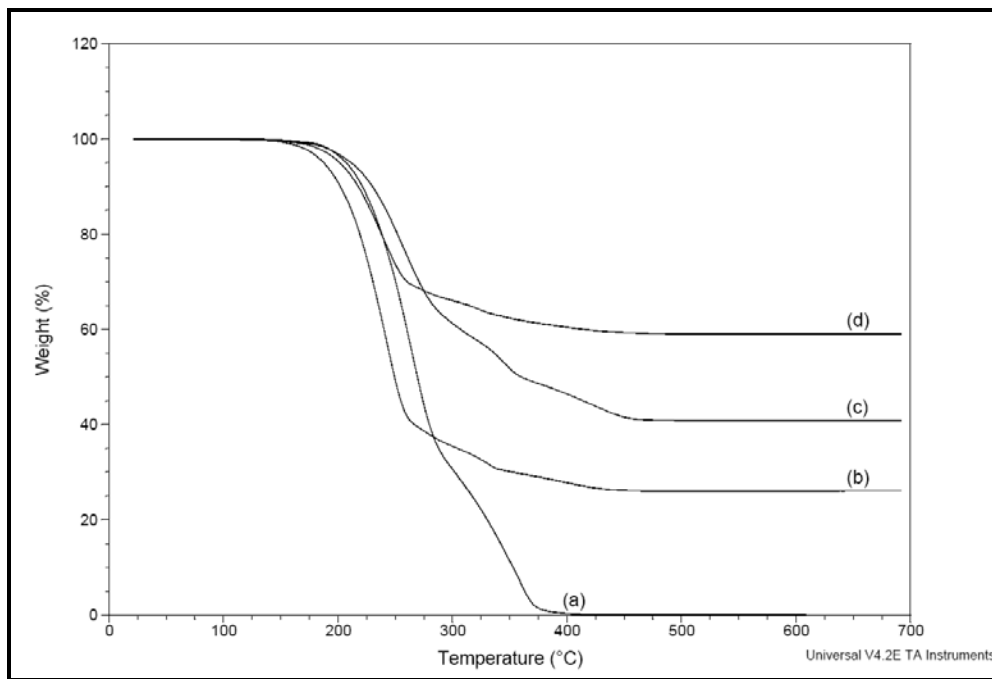


**Figure 0.16 -HMPA and Ti-HMPA TG curves for (a) 0%  $\text{TiO}_2$  (b) 23.6%  $\text{TiO}_2$  (c) 38.2%  $\text{TiO}_2$  (d) 55.3%  $\text{TiO}_2$ .**

Table 0.2 – TGA data for HMPA and Ti-HMPA

Sample (%TiO <sub>2</sub> )	T <sub>1i</sub> (°C)	T <sub>1max</sub> (°C)	Δm <sub>1</sub> (%)	T <sub>2i</sub> (°C)	T <sub>2max</sub> (°C)	Δm <sub>2</sub> (%)	T <sub>3i</sub> (°C)	T <sub>3max</sub> (°C)	Δm <sub>3</sub> (%)
HMPA	172.7	264.5	66.2	292.9	358.8	32.7	N/A	N/A	N/A
23.6% Ti-HMPA	161.8	251	54.3	279.2	319.1	17.2	352.3	390.4	4.70
23.6% Ti-HMPA*	-	-	71.1	-	-	22.5	-	-	6.15
38.2% Ti-HMPA	167.3	257.8	37.9	300.5	345.7	11.8	364.4	427.9	8.64
38.2% Ti-HMPA*	-	-	61.3	-	-	19.1	-	-	14.0
55.3% Ti-HMPA	168.1	238.3	30.6	271	323.8	7.1	369.2	412.1	4.75
55.3% Ti-HMPA*	-	-	68.5	-	-	15.9	-	-	10.6

\* represents the mass percentages after the mass of TiO<sub>2</sub> was subtracted.

### 1.19 Functionalized Polyurethanes

As mentioned previously, there are two main methods for functionalization; both of which were explored in this work, i.e. monomer and polymer functionalization methods, shown in Figure 5.17 and Figure 5.18, respectively. Using these two methods, nano-TiO<sub>2</sub>/PUcomposites were formed with varying mass percentages of TiO<sub>2</sub> for subsequent cleaning and contact angle analysis studies.

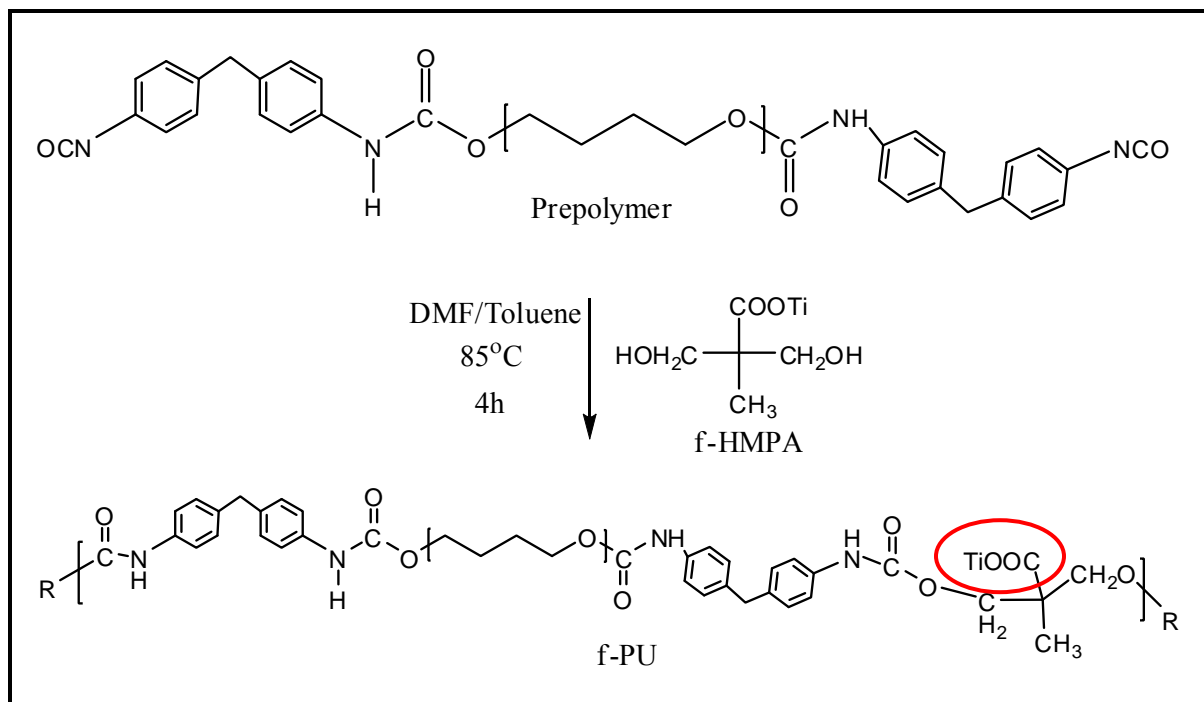
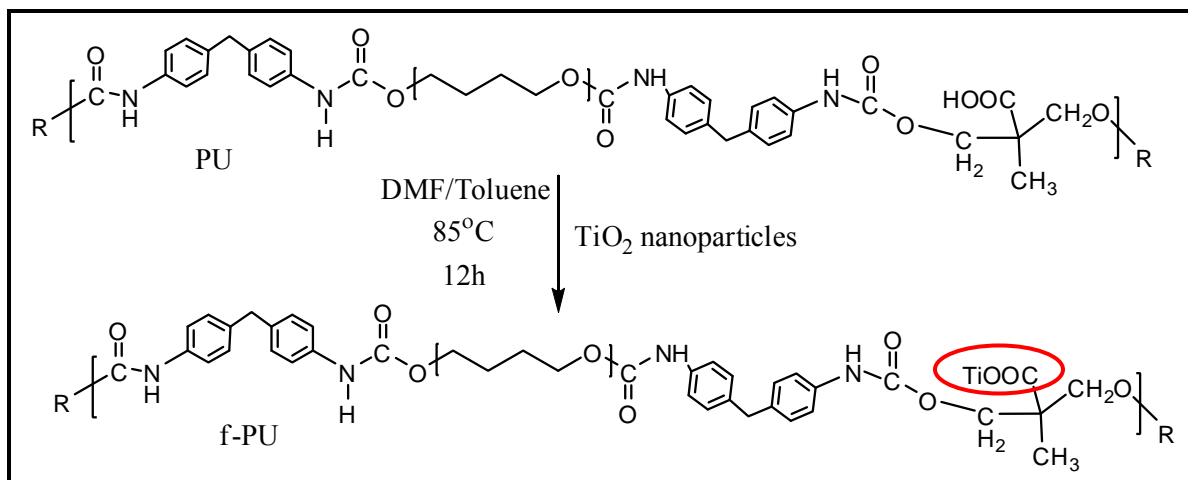


Figure 0.17 – Functionalized Polyurethane Synthesis using the Monomer Approach.



**Figure 0.18 - Functionalization Synthesis using the Polymer Approach.**

### 1.19.1 SEM Analysis for TiO<sub>2</sub> Agglomeration

As previously mentioned, the photodegradation/cleaning efficiency can be affected by the size, shape, and agglomeration of TiO<sub>2</sub> particles. TiO<sub>2</sub> nanoparticles incorporated into the polymer matrix appear in the form of micron-sized agglomerates, depicted in Figure 5.19(b). Random sections of the coatings were sampled and the following images represent each of the surfaces. The monomer functionalization method, however, significantly reduces the size of these agglomerates for both the 5wt% TiO<sub>2</sub>, (c), and 10wt% TiO<sub>2</sub>, (d), samples.

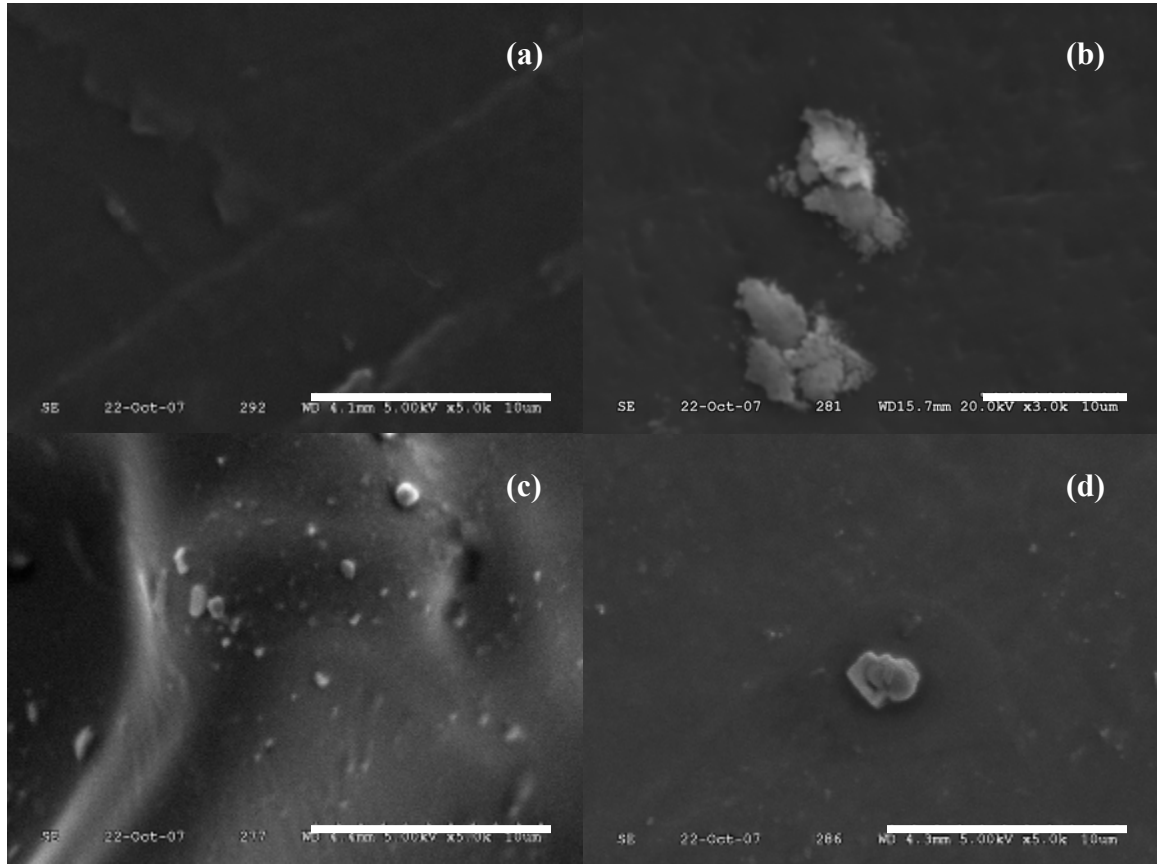


**Figure 0.19 – SEM Images for PU and TiO<sub>2</sub>-PU Composites. (a) PU (b) 5% TiO<sub>2</sub>-PU Composite – Polymer Functionalization Method (c) 5% TiO<sub>2</sub>-PU Composite – Monomer Functionalization Method and (d) 10% TiO<sub>2</sub>-PU Composite – Monomer Functionalization Method. All scale bars are 10µm.**

In addition, the dispersion of TiO<sub>2</sub> in each of these samples can clearly be seen using SEM-EDX imaging as shown in Figure 5.20.

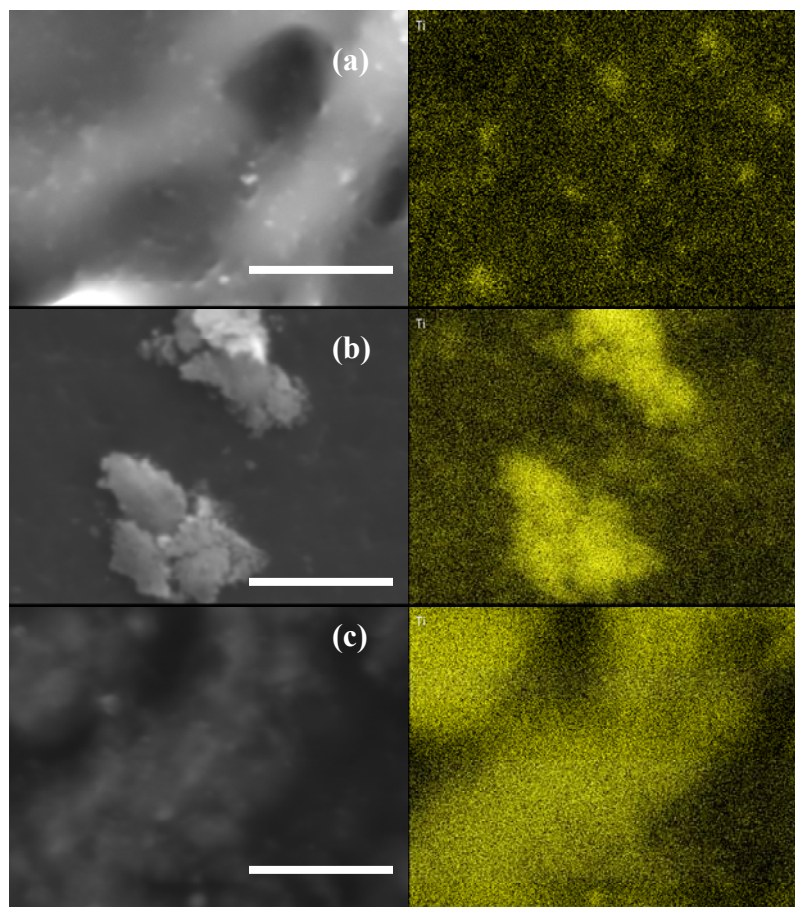


**Figure 0.20 - SEM-EDX Titanium Mapping of Composite Surfaces: Left is SEM Image, Right is EDX Image (a) 5wt% TiO<sub>2</sub>-PU Composite – Monomer Functionalization Method (b) 5wt% TiO<sub>2</sub>-PU Composite – Polymer Functionalization Method (c) 10wt% TiO<sub>2</sub>-PU Composite – Monomer Functionalization Method.**

The monomer functionalization method shown in (a) and (c) for 5wt% and 10wt% TiO<sub>2</sub>-PU composites, respectively, show improved separation, and decreased agglomeration compared to that of (b) 5wt% TiO<sub>2</sub>-PU composite, produced via the polymer functionalization method.

Figures 5.21 – 5.24 show the EDX titanium mapping for PU, 5wt% TiO<sub>2</sub>-PU monomer synthesis, 5wt% TiO<sub>2</sub>-PU polymer synthesis, and 10 wt% TiO<sub>2</sub>-PU monomer synthesis samples respectively. The PU clearly describes a surface with no TiO<sub>2</sub>, whereas the other three surfaces contain a certain percentage of TiO<sub>2</sub>. The 5wt% TiO<sub>2</sub>-PU monomer synthesis sample shows an absorbance of 7500 and 2000 counts at 4.5 keV and 5.0 keV respectively, but the 5wt% TiO<sub>2</sub>-PU polymer synthesis, and 10 wt% TiO<sub>2</sub>-PU monomer

synthesis samples showed much larger absorbance's, 25000/5000 counts and 31000/5100 counts respectively. The higher absorbance corresponds to a greater amount of  $\text{TiO}_2$  at the surface of the composite samples.

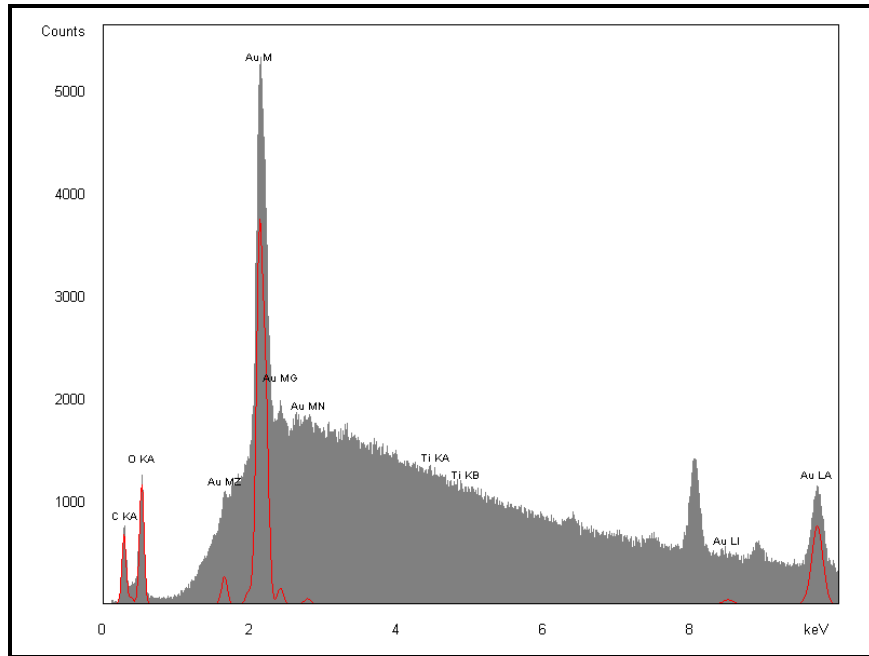


**Figure 0.21 - EDX for PU Samples**

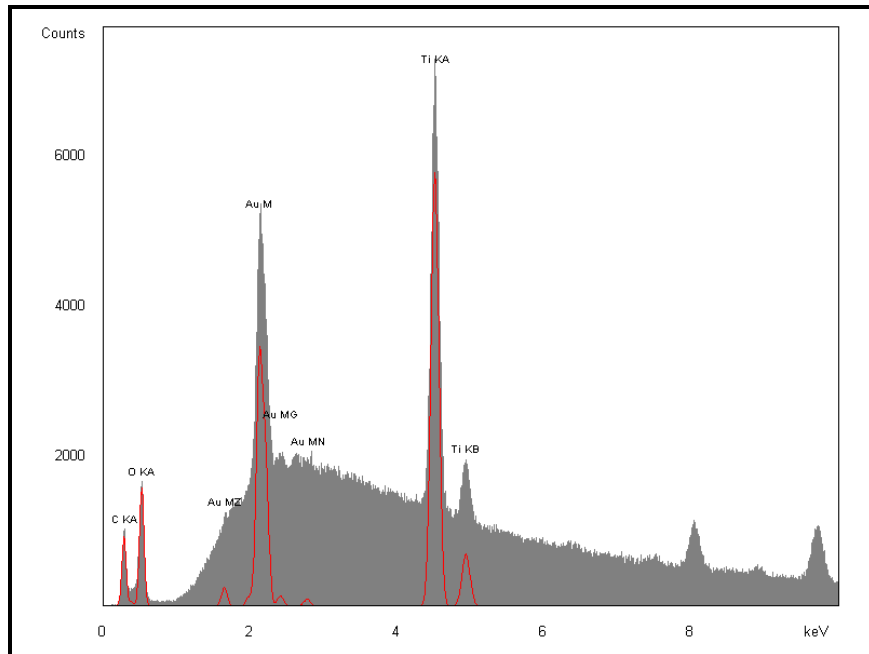


**Figure 0.22 - EDX for the 5wt%  $\text{TiO}_2$ -PU Monomer Functionalization Method.**

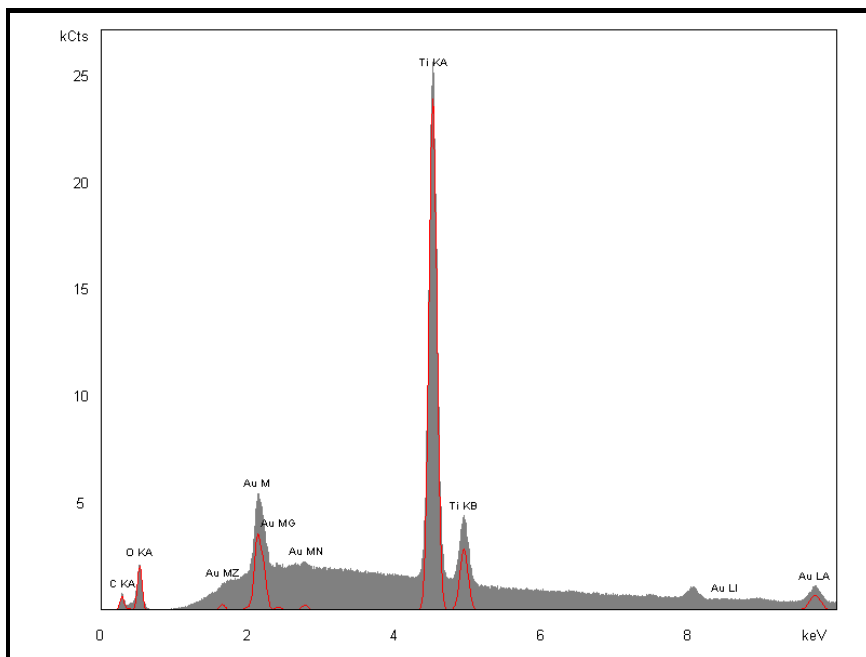


**Figure 0.23 - EDX for the 5wt% TiO<sub>2</sub>-PU Polymer Functionalization Method.**

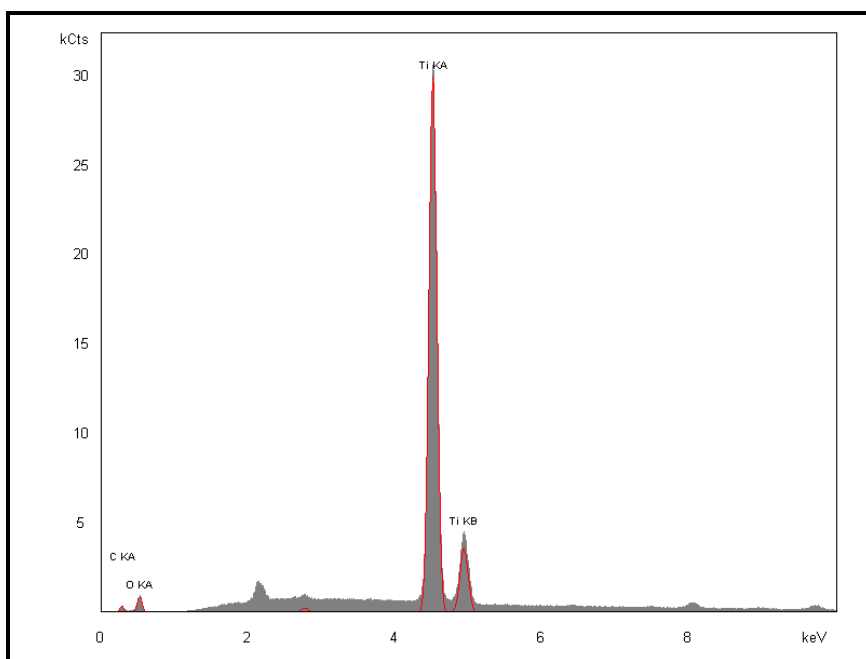


**Figure 0.24 - EDX for the 10wt% TiO<sub>2</sub>-PU Monomer Functionalization Method.**

### 1.19.2 TGA Analysis

The effect of the TiO<sub>2</sub> mass percentage on the thermal decomposition of polyurethane hard segment, and the effect of the different method of functionalization was studied using TGA analysis. The TG curves in Figure 5.25 show both functionalization methods at 5 and 10wt% TiO<sub>2</sub> for decreasing mass % with increasing temperature. Bajsik<sup>82</sup> studied the thermal degradation of PU before and after photodegradation and found that the MDI hard segment thermally decomposed around 275°C. This figure shows that increasing the mass percentage of TiO<sub>2</sub> in the polymer increases the thermal stability of the hard segment, thus increasing the thermal degradation temperature. This enhanced thermal behaviour is due to the ionic bonding between TiO<sub>2</sub> and the polymer chains, and the amount of ionic cross-linking formed through functionalization.

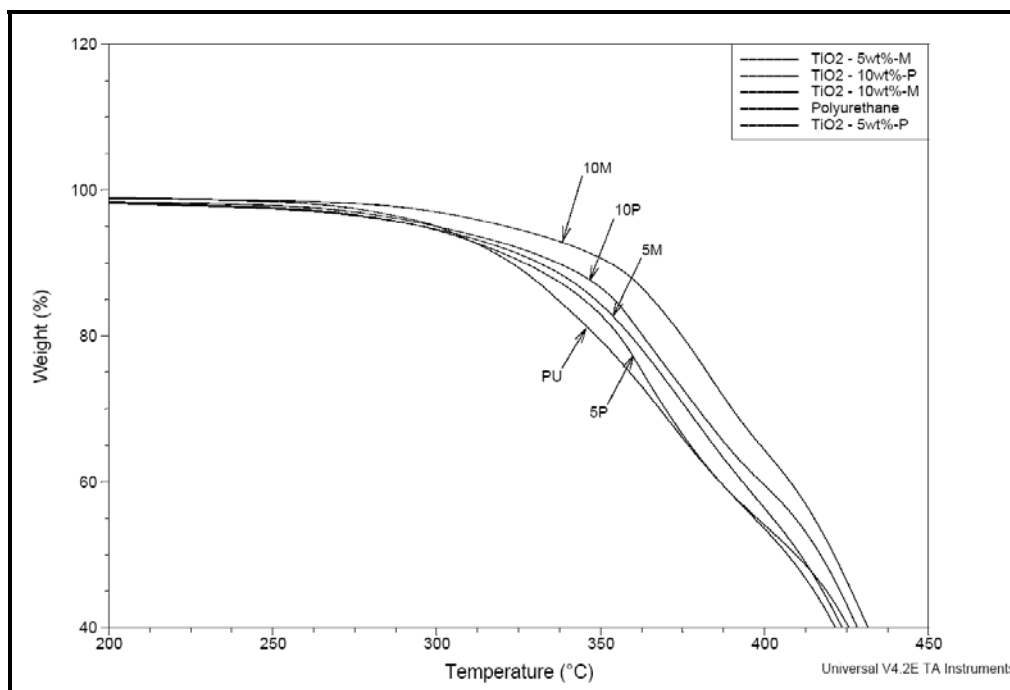


**Figure 0.25 – Comparative Mass Loss with respect to Temperature for Different Concentrations and Functionalization Methods.**

The TG curves also prove the monomer method of functionalization (“grafting from” method) improves the thermal stability of the PU elastomer. This is due in part to increased dispersion of TiO<sub>2</sub> and decreased surface area, shown previously in Figure 5.20, meaning that the polymer method of functionalization is giving way to other forces,

not breaking apart the TiO<sub>2</sub> agglomerates, thus having larger groups of particles not functionalized in the matrix of the polymer. This can lead to gaps in the polymer chains decreasing the thermal properties, thus decreasing the mechanical properties of the polyurethane.<sup>75</sup> This can be compared to the monomer method which decreases the size of the TiO<sub>2</sub> agglomerates, increasing the amount of ionic cross-linking.

Nanoparticles tend to strongly agglomerate due to the intermolecular attraction forces from their large surface area and close distance between particles. This becomes important because the functionalization via the monomer method aids in the breaking up of these agglomerates as seen in the SEM images in Figure 5.6 for Ti-HMPA and Figure 5.20 for TiO<sub>2</sub>-PU composites, whereas the polymer functionalization method does not break up these agglomerates as well, decreasing some of the properties of the final composite. These properties are also seen via TGA analysis where the hard segment of the polyurethane prepared by the monomer functionalization method has a higher thermal stability compared to those prepared by the polymer method.

### 1.19.3 FTIR analysis

Figure 5.26 compares the FTIR spectra for varying TiO<sub>2</sub> mass % in the PU composites. This figure shows little to no difference with increasing percentages of TiO<sub>2</sub> in the PU samples. The functionalization peaks seen in Figure 5.11 are not observed because the absorption levels for Ti-O-C coordination is almost negligible compared to that of the polyurethane peaks.

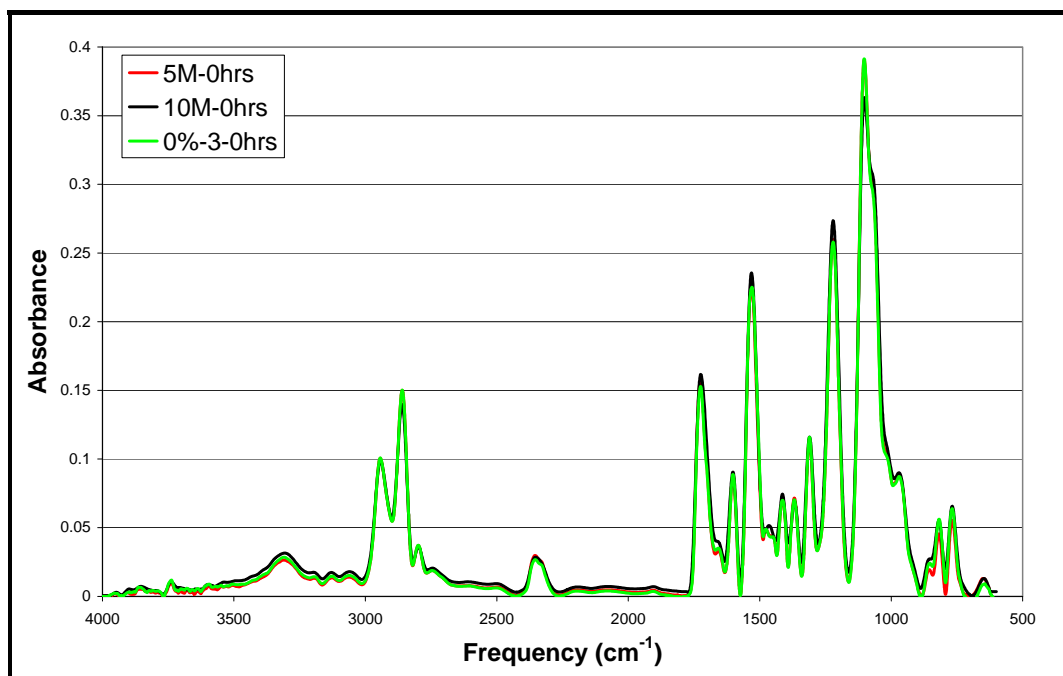


**Figure 0.26 – FTIR Comparisons for the Monomer Functionalized PU-TiO<sub>2</sub> composites at 0, 5, and 10wt% TiO<sub>2</sub> at 0 Hours of Degradation.**

## 1.20 Cleanability

In all photocatalytic reactions, the intensity of light is important to calculate the amount of UV directed at the sample in order to compare it with natural light. It has been shown that greater degradation occurred at higher lamp power for PEO, as predicted by Vijayalakshmi and Madras,<sup>83</sup> whereas at lower lamp power, no degradation occurred indicating that a minimum threshold of light intensity is necessary for initiating the degradation process. An energy of 3.4eV was calculated using the wave model equation and Planck's relation for a photon of 365nm, which is greater than the band gap energy  $E_g = 3.2\text{eV}$  of TiO<sub>2</sub>, meaning photocatalysis can occur at  $\lambda = 365\text{nm}$ . However, it is assumed that one photon interacts with one molecule of TiO<sub>2</sub> that causes a photoreaction.<sup>37</sup> Therefore, the energy of radiation produced at this wavelength becomes 328 KJ/mole or 78.5 Kcal/mol, which is sufficient to break certain chemical bonds (see Table Appendix A.3 for common bond dissociation enthalpies).

### 1.20.1 Surface Cleaning

Figure 5.27 shows the FTIR analysis for the cleanability of a 5wt% TiO<sub>2</sub>-PU composite sample produced through the monomer functionalization method, with the addition of 20% excess HMPA in order to study the cleaning effect.

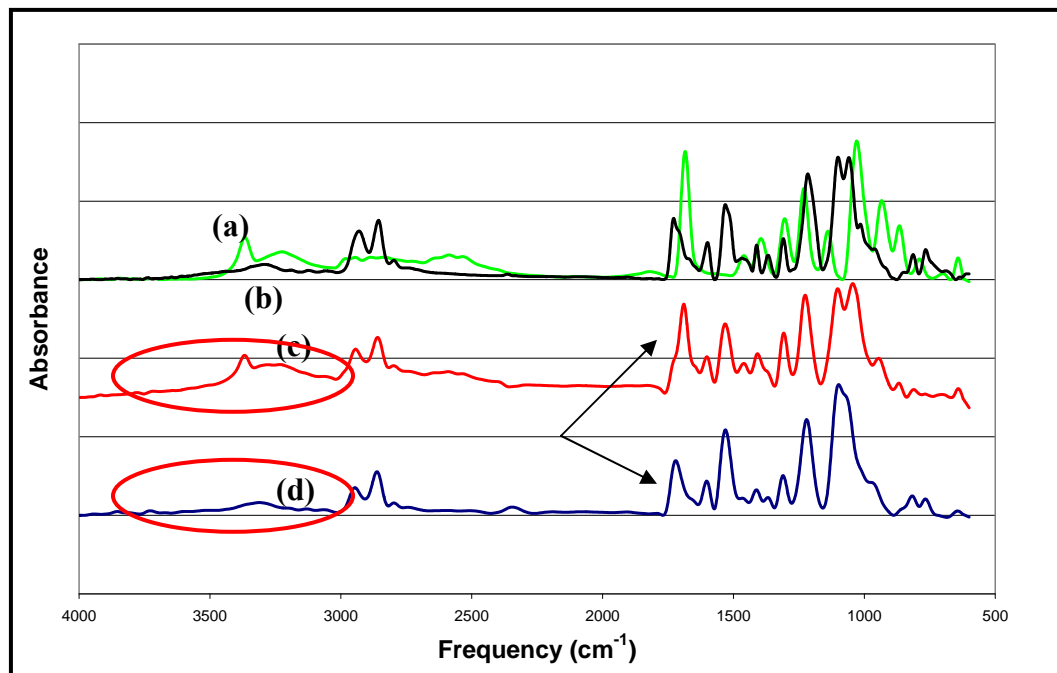


**Figure 0.27 - FTIR Spectra for Composite Cleanability: (a) HMPA, (b) 5wt%TiO<sub>2</sub>-PU Composite Before Irradiation, (c) HMPA-Composite Mixture Before Irradiation, and (d) HMPA-Composite Mixture After 24 Hours After Irradiation.**

The figure shows the individual spectra peaks for HMPA (a) and the TiO<sub>2</sub>/PU composite (b), and the combined spectra for the PU-Composite material with the HMPA mixed within the bulk of the polymer (c). Curve (d) shows the resulting surface spectra of the PU-Composite after 24 hrs of irradiation. It is evident that the OH stretch peak, 3000-3600cm<sup>-1</sup>, and the C=O stretch peak, 1710cm<sup>-1</sup>, decrease upon irradiation. Both the polymer functionalization method and the monomer functionalization method yielded the same final results using FTIR analysis after 24 hrs of irradiation. Figure 5.28 compares the peaks for the cleanability study, before and after irradiation, where the complete degradation of HMPA is seen by the disappearance of the OH peaks located between 3000-3600cm<sup>-1</sup>, the carboxylic acid OH peaks located between 2500-3000cm<sup>-1</sup> and a

decrease in the C=O peak at  $1710\text{cm}^{-1}$ ; all three of which are the main characteristic peaks of HMPA.

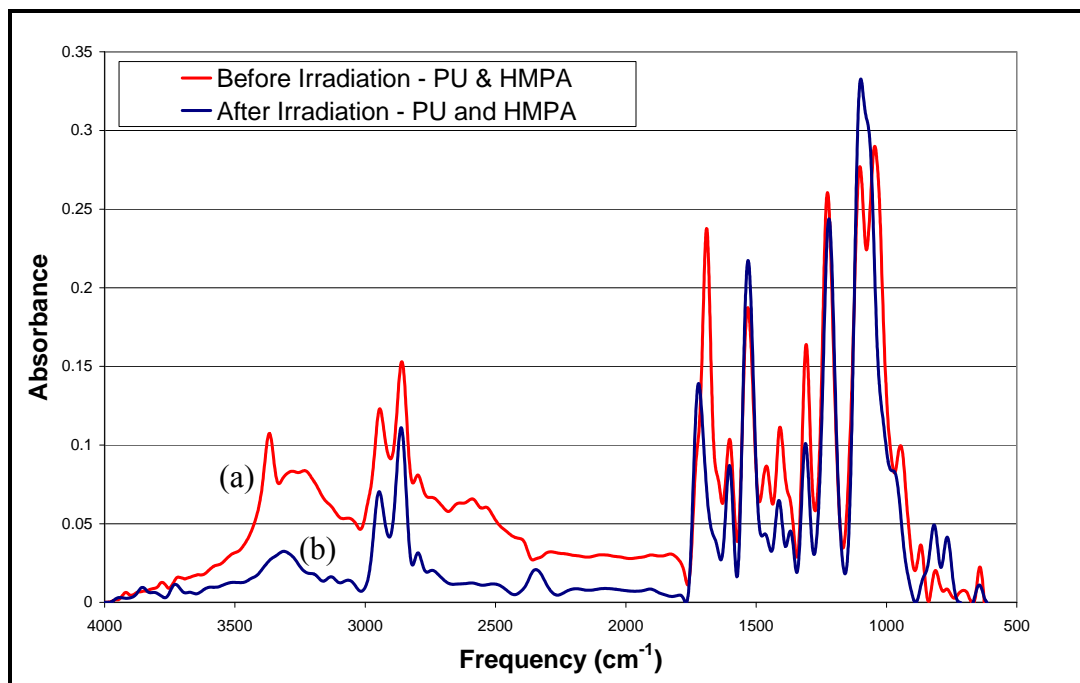


**Figure 0.28 – Cleanability of HMPA from PU-TiO<sub>2</sub> Composites (a) Before Irradiation and (b) After Irradiation.**

Combining this FTIR analysis with literature for the photocatalytic degradation pathway of malic acid,<sup>36</sup> stearic acid,<sup>16</sup> and acetic acid,<sup>36</sup> the proposed chemistry for the photocatalytic degradation of HMPA is provided in Figure 5.29. The synthesis at which the HMPA is degraded is through oxidation and decarboxylation reactions. The mechanism for malic acid proposed by Hermmann, eventually photocatalytically degrades into acetic acid, which is oxidized into carbon dioxide. Throughout every step, both H<sub>2</sub>O and CO<sub>2</sub> are the compound gases being generated from the photocatalytic oxidative reaction. In the cleaning of HMPA from the surface of a PU-TiO<sub>2</sub> composite coating, all samples (5% and 10%) and both methods (polymer and monomer functionalization) cleaned the surface within 24 hours.

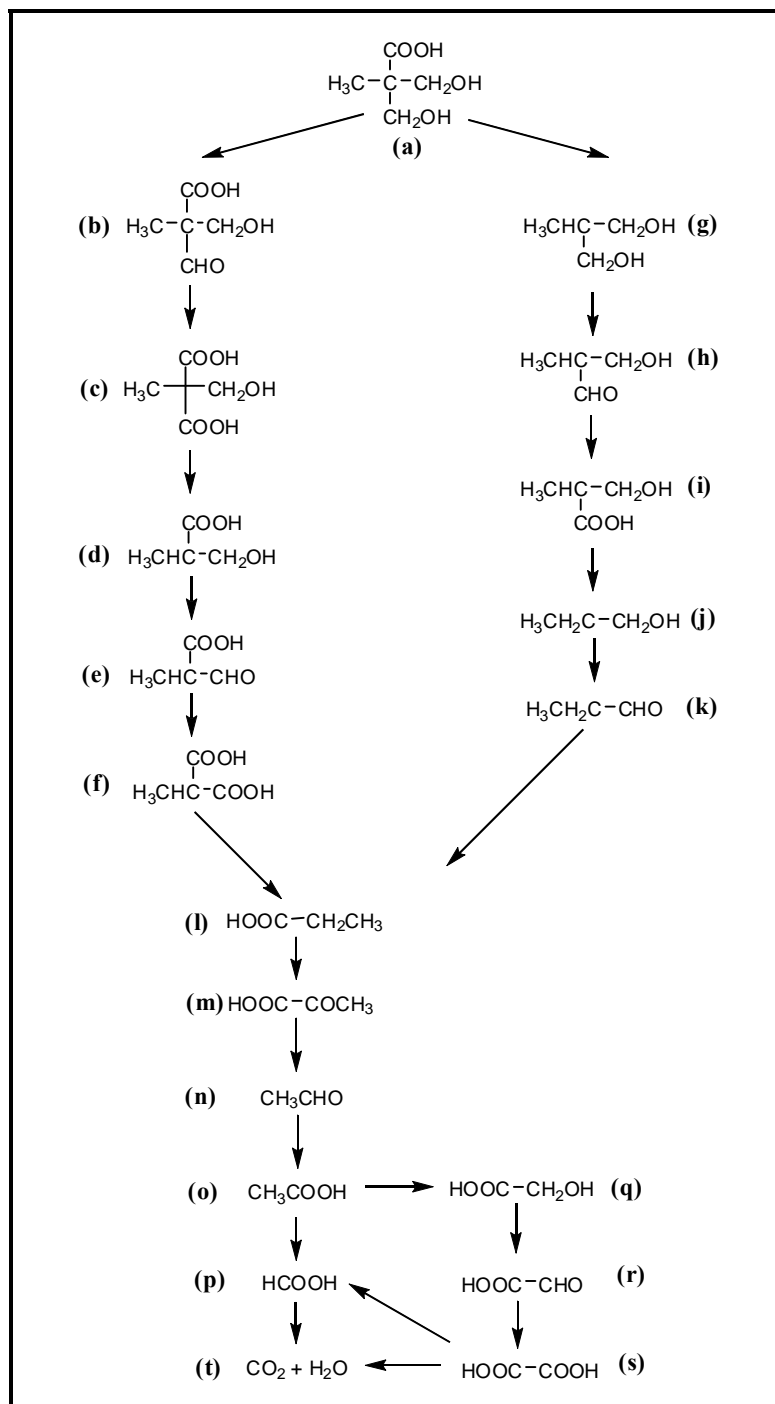


**Figure 0.29 – Proposed Chemistry for the Photocatalytic Degradation of HMPA (a) HMPA (l) Propanoic Acid (m) Pyruvic Acid (n) Acetaldehyde (o) Acetic Acid (p) Formic Acid (q) Glycolic Acid (r) Glyoxylic Acid (s) Oxalic Acid (t) CO<sub>2</sub> and H<sub>2</sub>O.**

Horikoshi et al. also noticed that the photocatalytic degradation of PVC blended with TiO<sub>2</sub> achieved a clean disposal method where no dioxins, typically created by PVC

degradation, formed. The resulting products formed were CO<sub>2</sub>, H<sub>2</sub>O and chlorine.<sup>81</sup> The proposed mechanism then converts acetic acid to either formic acid or hydroxyethanoic acid, in which both photocatalytically oxidize into formic acid and carbon dioxide.

## 1.21 Results - Wettability

### 1.21.1 Surface Roughness

It has been shown in the literature<sup>1</sup> that a film consisting of only TiO<sub>2</sub> has a water contact angle close to zero upon UV irradiation. From the SEM analysis shown in Figure 5.20, it is clear that the composite sample surfaces are composed of both polyurethane and TiO<sub>2</sub>. Polyurethane is a semi-hydrophobic polymer, and therefore the contact angle after irradiation does not decrease to zero, hence, a super-hydrophilic surface cannot be created upon irradiation. Table 5.3 shows the solved values for  $f_{TiO_2}$  and  $f_{PU}$ , the surface area fractions of TiO<sub>2</sub> and PU respectively using Cassie's equation (Eqn. 3.4) for all samples. The  $\theta_{app-avg}$  is the average apparent contact angle from sessile drop measurements. The trend shows that the fraction of TiO<sub>2</sub> on the surface increases with increasing TiO<sub>2</sub> content (7.9% to 31.7%) and increases from the monomer synthesis (7.9%) to the polymer synthesis method (26.6%). The contact angle for TiO<sub>2</sub> was assumed to be 30°,<sup>1, 16, 17</sup> however, the nanostructure and roughness of the surface can also change this values.

**Table 0.3 - Calculations from Cassie's Equation.**

<b>Sample</b>	<b><math>\theta_{app-comp}</math></b>	<b><math>f_{TiO_2}</math></b>	<b><math>f_{PU}</math></b>	<b>Cos (<math>\theta_{app-comp}</math>)</b>	<b>Cos (<math>\theta_{app-PU}</math>)</b>	<b>Cos (<math>\theta_{app-TiO_2}</math>)</b>
<b>PU</b>	93.6±1.82	0	1		-0.062	
<b>5wt% TiO<sub>2</sub>-PU monomer functionalization</b>	89.4±3.91	0.079	0.921	0.011		0.866
<b>5wt% TiO<sub>2</sub>-PU polymer functionalization</b>	79.4±2.07	0.266	0.734	0.185		0.866
<b>10wt% TiO<sub>2</sub>-PU monomer functionalization</b>	76.6±1.67	0.317	0.682	0.232		0.866

However, the values shown in Table 5.3 are not entirely accurate because the surface roughness values for the polyurethane and TiO<sub>2</sub> samples were not calculated, and the

Wenzel equation was not used. AFM characterization, as shown in Figure 5.30, for the surface roughness showed inconclusive results due to the surface of the polymer samples being too soft, such that the cantilever tip of the atomic force microscope stuck to the surface of the samples deforming the samples and creating inaccurate results. However, Prasad-Shastri et al.<sup>84</sup> provided an estimated surface roughness factor found through AFM analysis for PU elastomers equal to 3.1. This roughness would decrease the fraction of TiO<sub>2</sub> on the surface significantly. The surface roughness for TiO<sub>2</sub> from the literature varies tremendously depending on the preparation, crystallinity, size and porosity of the TiO<sub>2</sub> crystals. Hwang et al.<sup>85</sup> calculated a surface roughness of R = 9.028, Karunagaran<sup>86</sup> et al. estimated R = 5.8, and Šícha et al.<sup>87</sup> found the surface roughness in terms of crystal type, where amorphous TiO<sub>2</sub>, R = 2, Rutile TiO<sub>2</sub>, R = 7.5, anatase TiO<sub>2</sub>, R = 6-8, anatase-rutile mixtures R = 12-18. As there is such a wide range of values for the roughness of TiO<sub>2</sub>, an accurate estimation of TiO<sub>2</sub> concentration on the surface of the composite cannot be accurately determined. Also, some of the TiO<sub>2</sub> pores will be surrounded and filled by the PU matrix, decreasing the surface roughness of TiO<sub>2</sub> in the composite from that expected.

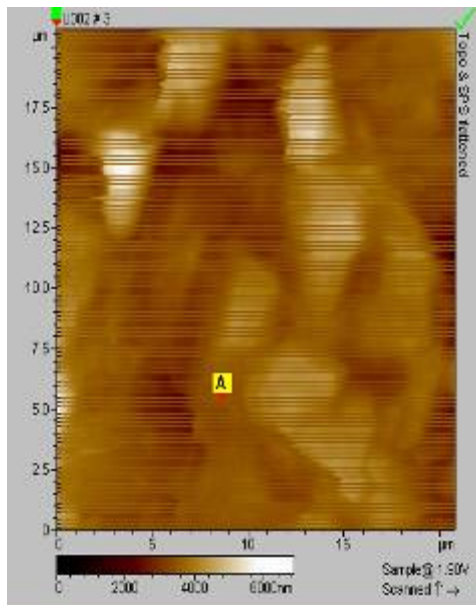


**Figure 0.30 - AFM Image of 5wt% TiO<sub>2</sub>-PU Composite Produced by the Monomer Method.**

Although theoretical surface concentrations of TiO<sub>2</sub> cannot be accurately calculated, SEM-EDX imaging (Figure 5.20) gave visual conformation of titanium dioxide in the

composite coating using titanium mapping. The titanium mapping agrees with the contact angles measured in Table 5.3. The 5wt% TiO<sub>2</sub>-PU composite formed from the monomer functionalization method displays far less TiO<sub>2</sub> on the surface compared to the 5wt% TiO<sub>2</sub>-PU composite formed from the polymer functionalization method. The estimated surface coverage using the Cassie equation ranges from 7.9% for the 5wt% TiO<sub>2</sub>/PU monomer functionalization method composites, to 18.5% for the 5wt% TiO<sub>2</sub>/PU polymer functionalization method composites, and 26.6% respectively for the 10wt% TiO<sub>2</sub>/PU monomer functionalization method composites. Although the same percentage of TiO<sub>2</sub> was added in solution, the larger agglomerates from the polymer functionalization method protrude from the matrix covering more surface area for the area measured, thus displaying poor dispersion. The monomer functionalization method disperses the nano-TiO<sub>2</sub> more thoroughly into the polymer matrix, causing smaller particles that may not project from the surface. The Cassie equation trend values solving for surface area fraction of TiO<sub>2</sub>,  $f_1$ , follows the same trend observed from the EDX Ti maps. The EDX Ti maps show the fraction of Ti on the surface of the samples increase between both methods from 7500/2000 counts for the 5wt% TiO<sub>2</sub>/PU monomer functionalization composites and 25000/5000 counts for the 5wt% TiO<sub>2</sub>/PU polymer functionalization composites, and increase with increasing TiO<sub>2</sub> mass in the polymer matrix from 7500/2000 counts to 31000/5100 counts for the 5 and 10wt% TiO<sub>2</sub>/PU monomer functionalization composites.

After irradiation, the contact angle decreased for all samples, however, there is error associated with the contact angle measurements as once the samples were removed from the UV source, the contact angle for the PU-TiO<sub>2</sub> composites could increase back to its original contact angle.<sup>1</sup> Therefore, these angles could be lower than that measured since the contact angles could not be measured directly after UV irradiation.

## RESULTS – DEGRADATION OF POLYURETHANE AND ITS COMPOSITES

All polymers can be degraded including polyurethanes. There are many ways in which polyurethanes can be degraded including: hydrolysis, photolysis, solvolysis, thermolysis, pyrolysis, oxidation, and microbial degradation. The main areas of degradation of interest for this study are photolysis, the decomposition of a chemical compound by the interaction of light, and thermolysis, degradation due to heat.<sup>75</sup>

### 1.22 Polyurethane Thermal Degradation

The thermal degradation of polymeric materials has been the focus of many studies to investigate the processes responsible for the deterioration of polymeric physical properties.<sup>82</sup> The temperature of the initial decomposition of the urethane bond depends on the type of di-isocyanate and di-alcohol used. Table 6.1 shows the onset dissociation temperature for different types of polyurethanes; although the aromatic based urethanes are the most important for this work. The aromatic-based urethane bond begins its thermal dissociation around 180 °C.<sup>75</sup> Polyurethanes are not typically thermally stable polymers. The thermal degradation of segmented PU's is a two step process in which the first step is ascribed to the hard segment degradation, while the second step is ascribed to the soft segment degradation.<sup>88</sup>

**Table 0.1 - Onset of Dissociation for various Polyurethanes**

<b>Linkage</b>	<b>Onset of Dissociation (°C)</b>
Aliphatic allophanate	85-105
Aromatic allophanate	110-120
Aliphatic biuret	100-110
Aromatic biuret	115-125
Aliphatic urea	140-180
Aromatic urea	160-200
Aliphatic urethane	160-180
Aromatic urethane	180-200
Di-substituted urea	235-250

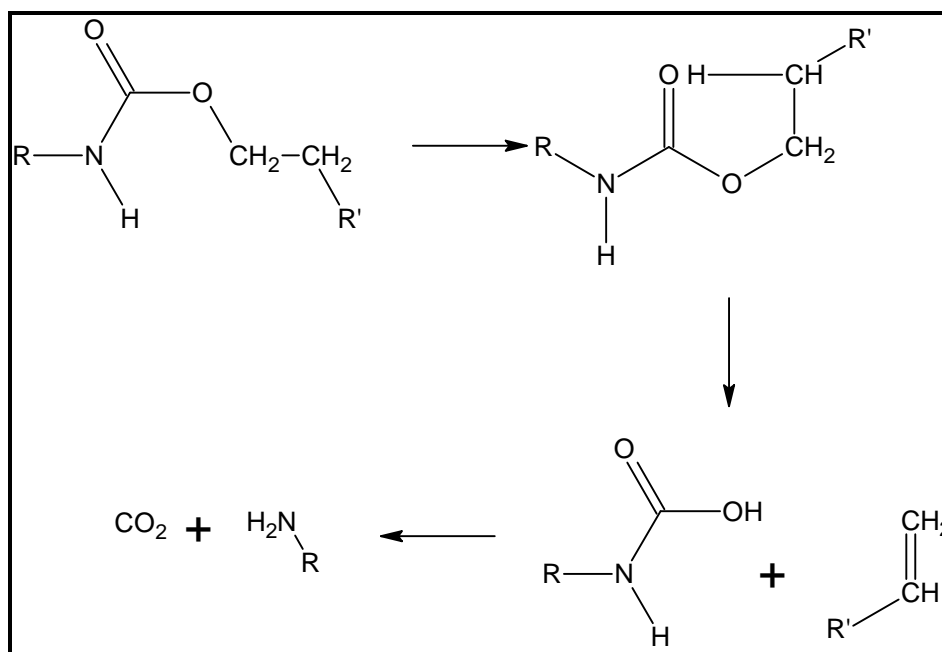


**Figure 0.1 – Thermal Degradation of Urethane Linkages Forming CO<sub>2</sub> and an Olefin.**

The urethane bond undergoes three separate types of thermal degradation: (a) depolymerization of PU to the precursor isocyanates and alcohols, (b) the cleavage of the oxygen to the alpha CH<sub>2</sub> group and the association of the hydrogen on the beta CH<sub>2</sub> group leading to the olefin and carbamic acid, which decomposes further to a primary amide and CO<sub>2</sub> (Figure 6.1), and (c) degrading the urethane into a secondary amine and CO<sub>2</sub> (Figure 6.2).<sup>75</sup>

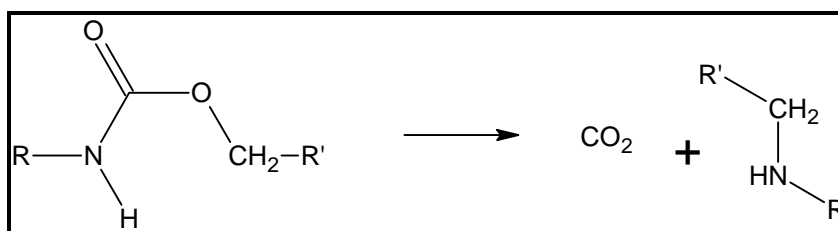


**Figure 0.2 - Thermal Degradation of Urethane Linkages Forming CO<sub>2</sub> and a Secondary Amine.**

### 1.23 Polyurethane Photodegradation

Not only can polymers experience photocatalytic degradation, polyurethanes also exhibit photodegradation on their own, especially MDI based polyurethanes, which are very susceptible to ultraviolet photooxidation degradation.<sup>22</sup> The exact mechanism for polyurethane photolytic degradations is still unknown.<sup>89</sup> One method of photooxidation in MDI derivative polyurethanes takes place through a quinoid route, as seen in Figure 6.3,<sup>90</sup> where the urethane bridge oxidizes to the quinone-imide structure.<sup>75</sup>

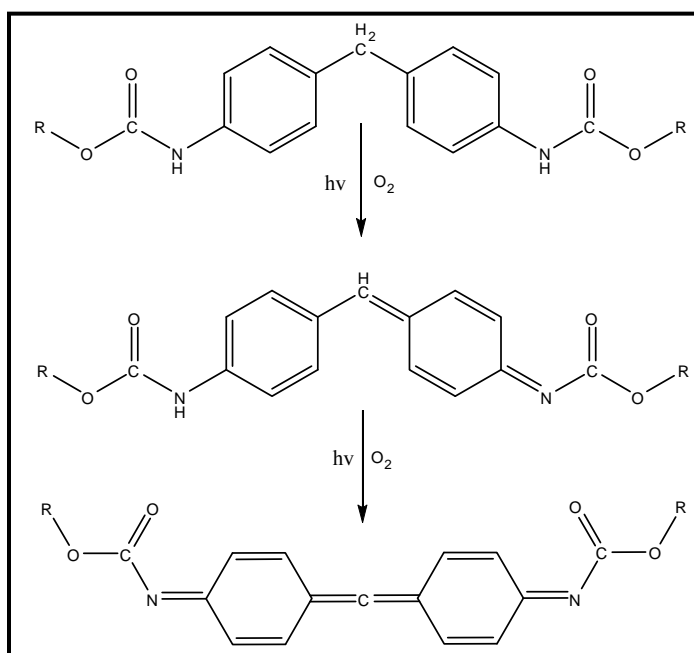
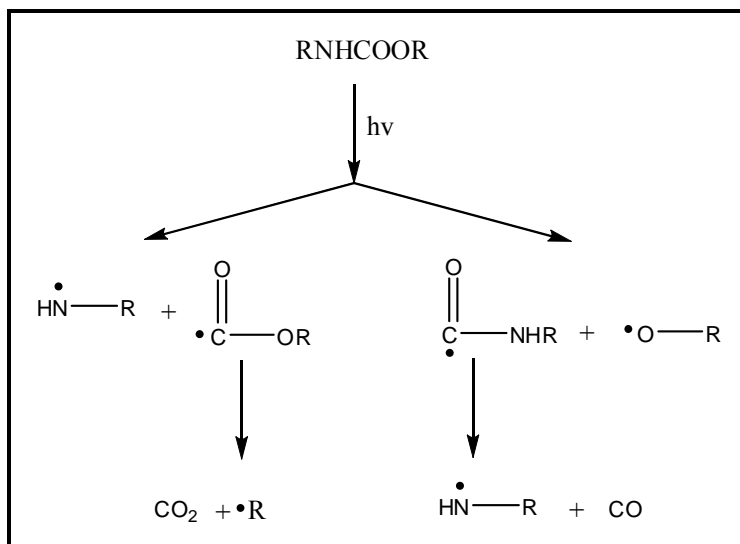


Figure 0.3 - Photolysis of MDI Polyurethanes via Photooxidation.

This quinone-imide structure is a strong chromophore resulting in the yellowing and eventual browning of polyurethanes. This limits polyurethane elastomer use for outdoor applications and high-quality products<sup>91</sup> without the incorporation of UV absorbers such as carbon black and  $TiO_2$ . Carbon black itself has drawbacks as light colours are not achievable with its incorporation, whereas,  $TiO_2$  has been used successfully in polyurethane chemistry as an opacifier to overcome photooxidation degradation.<sup>22</sup>

Another photodegradation possibility of PU elastomers is the scission of the urethane bond. There are two possible bonds within this linkage that are susceptible to scission: the nitrogen to carbon bond, resulting in an amino acid and formate radical liberating CO<sub>2</sub>; and the carbon oxygen scission, forming an alkoxy radical and a carbamyl radical decomposing to CO (Figure 6.4).<sup>90</sup>



**Figure 0.4 - Photolysis of Polyurethanes via Urethane Scission.**

To take advantage of the UV protection effect of rutile TiO<sub>2</sub> nanoparticles and the photocatalytic effect of anatase TiO<sub>2</sub>, one can add the appropriate TiO<sub>2</sub> nanoparticles into a polymer, both to create constant protection for outdoor applications, and to improve the service life of the products. A separate possibility is that TiO<sub>2</sub> can be added to accelerate degradation of waste polymers for reducing their solid waste environmental impact.<sup>22</sup>

In 2001, Bajsik and Rek<sup>82</sup> compared the thermal degradation of polyurethanes exposed to UV light. It was found that the initial temperatures of thermal degradation increased with samples that were exposed to UV light, indicating a higher thermal stability of UV-exposed elastomers to the beginning of thermal degradation. This is due to either the formation of the diquinone structure in the MDI polyurethane, or an increase in cross-linking of the polymer.

## 1.24 Polyurethane/TiO<sub>2</sub> Composite Degradation Chemistry

It has been noted that the photooxidation mechanism of PU lies in the direct photochemical oxidation of the carbon atoms in the urethane groups, and to the formation of primary hydroperoxy groups, which are decomposed into alkoxy and hydroxyl radicals. However, the initiation mechanism in the photocatalytic degradation of PU-TiO<sub>2</sub> composites also includes the photocatalytic oxidation of PU. TiO<sub>2</sub> particles are known to generate various active oxygen species such as  $\cdot\text{O}_2$ ,  $\cdot\text{OOH}$ , and  $\cdot\text{OH}$  under UV irradiation, which will attack neighboring polymer chains to abstract a hydrogen atom forming carbon-centered radicals, and then produce hydroxyl derivatives and carbonyl intermediates leading to chain cleavage.<sup>22</sup> Both the hard and soft segments of PU are susceptible to photocatalytic degradation.

### 1.24.1 Proposed Soft Segment Degradation

The soft segment of PU is composed of many CH<sub>2</sub>-CH<sub>2</sub> bonds. These bonds have the ability to be broken such that CO<sub>2</sub> is released.

1.  $\text{R-CH}_2\text{-CH}_2\text{-R}_1 + \text{HO}\cdot_{(\text{g})} \rightarrow \text{R}\cdot\text{-CH-CH}_2\text{-R}_1 + \text{H}_2\text{O}$
2.  $\text{R-CH}_2\text{-CH}_2\text{-R}_1 + \text{HO}\cdot_{(\text{g})} \rightarrow \text{R}\cdot\text{-CH-CH}_2\text{-R}_1 + \text{H}_2\text{O}$
3.  $\text{R-CH}_2\text{-CH}_2\text{-R}_1 + \text{HO}_2\cdot_{(\text{g})} \rightarrow \text{R}\cdot\text{-CH-CH}_2\text{-R}_1 + \text{H}_2\text{O}_2$
4.  $\text{R}\cdot\text{-CH-CH}_2\text{-R}_1 + \text{O}_2 \rightarrow \text{R-CH(OO}\cdot\text{)-CH}_2\text{-R}_1$
5.  $\text{R-CH(OO}\cdot\text{)-CH}_2\text{-R}_1 + \text{R-CH}_2\text{-CH}_2\text{-R}_1 \rightarrow \text{R-CH(OOH)-CH}_2\text{-R}_1 + \text{R}\cdot\text{-CH-CH}_2\text{-R}_1$
6.  $\text{R-CH(OOH)-CH}_2\text{-R}_1 + h\nu \rightarrow \text{R-CH(O}\cdot\text{)-CH}_2\text{-R}_1 + \text{HO}\cdot$
7.  $\text{R-CH(O}\cdot\text{)-CH}_2\text{-R}_1 \rightarrow \text{R-CHO} + \cdot\text{CH}_2\text{-R}_1$
8.  $\cdot\text{CH}_2\text{-R}_1 + \text{O}_2 \rightarrow \text{CO}_2 + \text{H}_2\text{O} + \text{H-R}_1$

The degradation of the soft segment begins with the hydroxyl and perhydroxy radicals reacting with the carbon chain exchanging the radical on a secondary carbon, described in Steps 1 and 2. These active oxygen species lead to the degradation reaction by attacking the polymer chain and successive chain cleavage.<sup>19</sup>

Steps 3-6 show the radical carbon reacting with oxygen and a photon such that the radical carbon is a primary carbon. In Step 7, the formation of an aldehyde material is formed. The primary carbons reacts with oxygen such that water and carbon dioxide are formed, where the polymer is photo degraded (Step 8). The mechanism for the photodegradation

of the PU soft segment is similar to the photodegradation mechanism for the degradation of PVC<sup>53</sup>, PEO<sup>82</sup> and polyacrylamide.<sup>83, 92</sup>

### 1.24.2 Hard Segment Degradation

As described above, the photooxidation of the MDI contained polyurethane elastomer degrades into a diquinone structure upon irradiation. However, the reaction between the excited state of  $\text{TiO}_2^*$  with the superoxide radical releases a singlet oxygen molecule,  $^1\text{O}_2$  which has the ability to attack any unsaturation existing in the polymer.<sup>53</sup> Compared to the soft segment, the proposed mechanism for the hard segment photocatalytic degradation occurs at a slow rate because the breaking of a double bond in the conjugated ring is more difficult to break than that of a regular unsaturated bond.

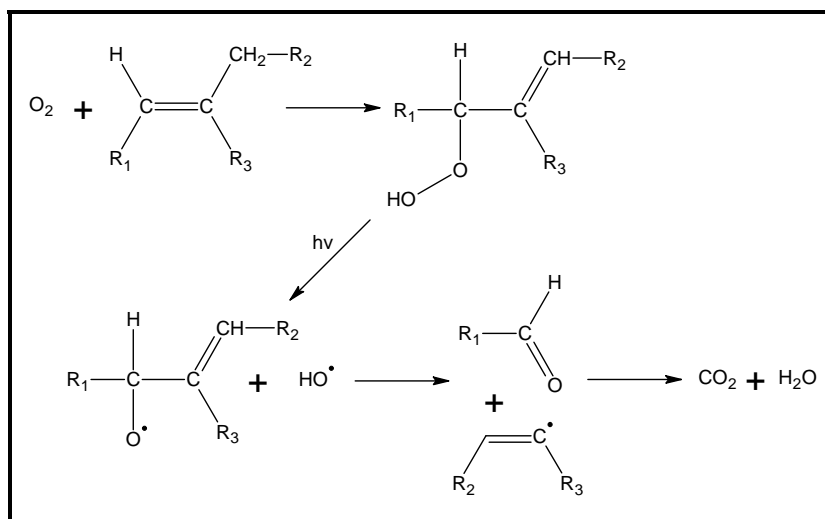


Figure 0.5 - Hard Segment Photocatalytic Degradation for  $\text{TiO}_2$ -Polyurethane Composites.

The proposed photocatalytic degradation of MDI is described in Figure 6.5, where the singlet oxygen breaks the bond in the conjugated ring to form an aldehyde and a new unsaturated chain. These products react further from both oxidative and reductive reactions, forming  $\text{CO}_2$  and  $\text{H}_2\text{O}$ .

## 1.25 Photocatalytic degradation of Polyurethane

As previously mentioned, polyurethanes are susceptible to photodegradation; however,  $\text{TiO}_2$  is capable of photocatalysis and can cause photocatalytic degradation to organic substrates. Therefore, a PU- $\text{TiO}_2$  composite coating has the ability to undergo both

photolysis and photocatalytic degradation. Two methods of evaluation were taken to study the effects of photolysis and photocatalytic degradation: TGA and FTIR analysis.

### 1.26 Thermogravimetric analysis

TGA analysis was used to quantify the thermal effects that UV irradiation has on both PU and its nano-TiO<sub>2</sub> composites for both photolysis and photocatalytic degradation effects. TGA analysis provides two functional curves, thermogravimetric (TG) and derivative thermogravimetric (DTG). The TG curves signify changes in thermal stability, while the DTG peaks aid in the quantification of the mass percentage of a given segment or section.

Figures 6.6-6.9 contain the TG and DTG curves measured at 0-96 hours of photodegradation for: PU, 5wt% TiO<sub>2</sub>-PU monomer method composite, 5wt% TiO<sub>2</sub>-PU polymer method composite, and 10wt% TiO<sub>2</sub>-PU monomer method composite samples respectively.

Before irradiation, all DTG and TG figures show two characteristic temperatures: the initial decomposition temperature of both the hard and soft segment,  $T_2^i$  and  $T_3^i$ , and the temperature corresponding to the maximum rate of thermal degradation,  $T_2^{\max}$  and  $T_3^{\max}$ . After irradiation, a third peak was created with decomposition temperatures,  $T_1^i$  and  $T_1^{\max}$ , corresponding to light weight components that were broken from the photocatalytic reaction of both the hard and soft segments of the PU coatings. These values are recorded in the Appendix section (Table A.4 – Table A.6) along with statistical analysis. Adjusted mass was used to compensate for the mass of TiO<sub>2</sub> in each sample to have a comparative analysis between samples. The change in mass is the mass fraction of each segment, and the adjusted mass eliminates the theoretical mass of TiO<sub>2</sub> in the sample to where comparative results can be made between different samples. The residue is combined mass of carbon black and TiO<sub>2</sub> that was not burned off at 700°C.

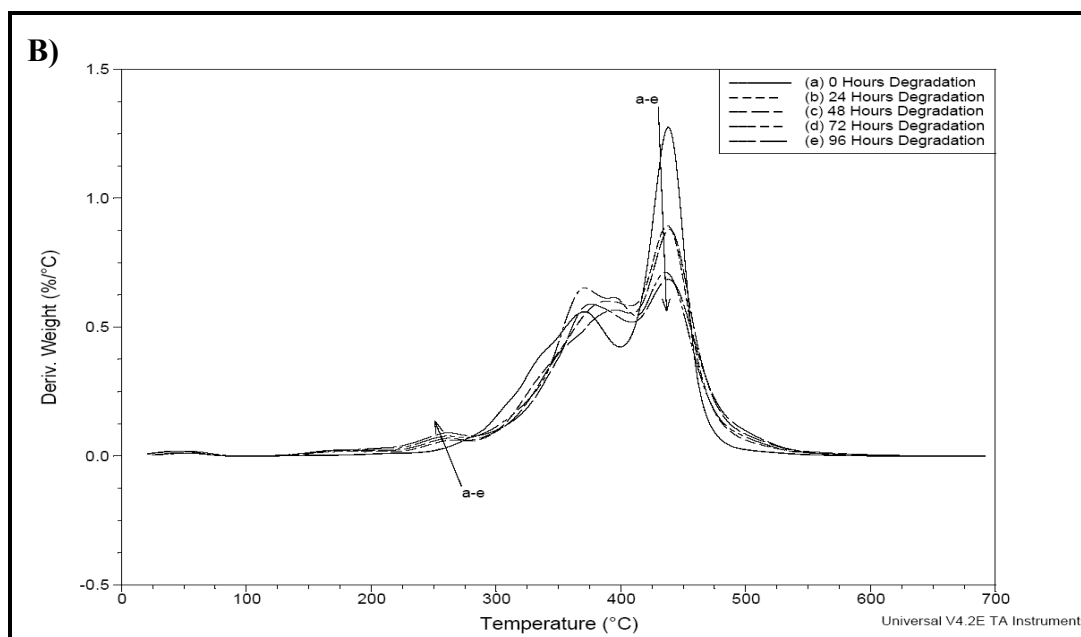
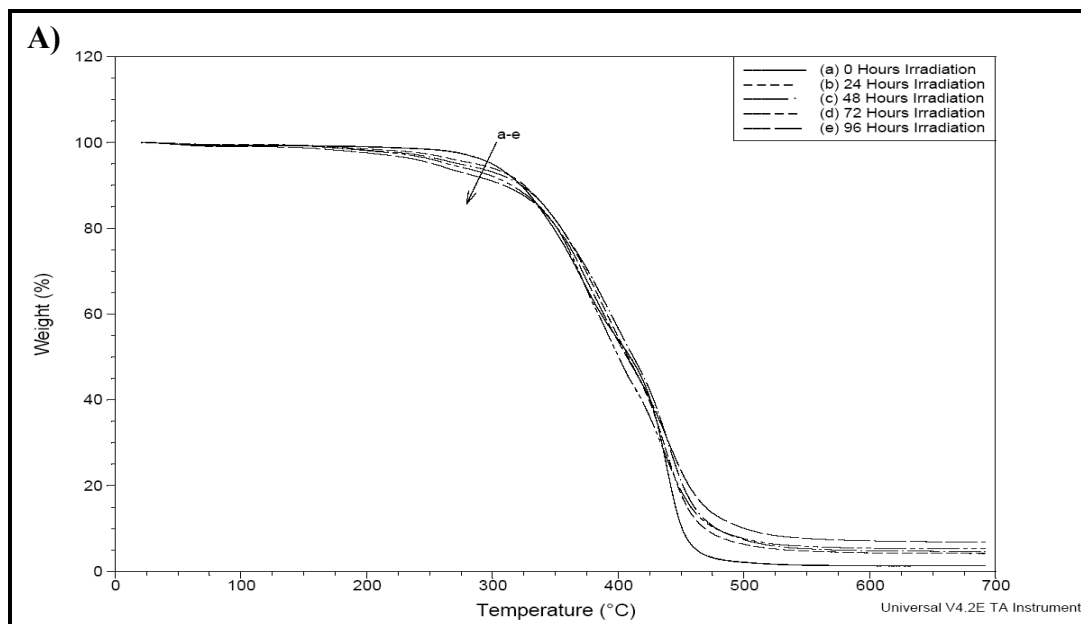


**Figure 0.6 – A) TG and B) DTG Curves for PU for (a) 0 (b) 24 (c) 48 (d) 72 (e) 96 Hours of Irradiation.**

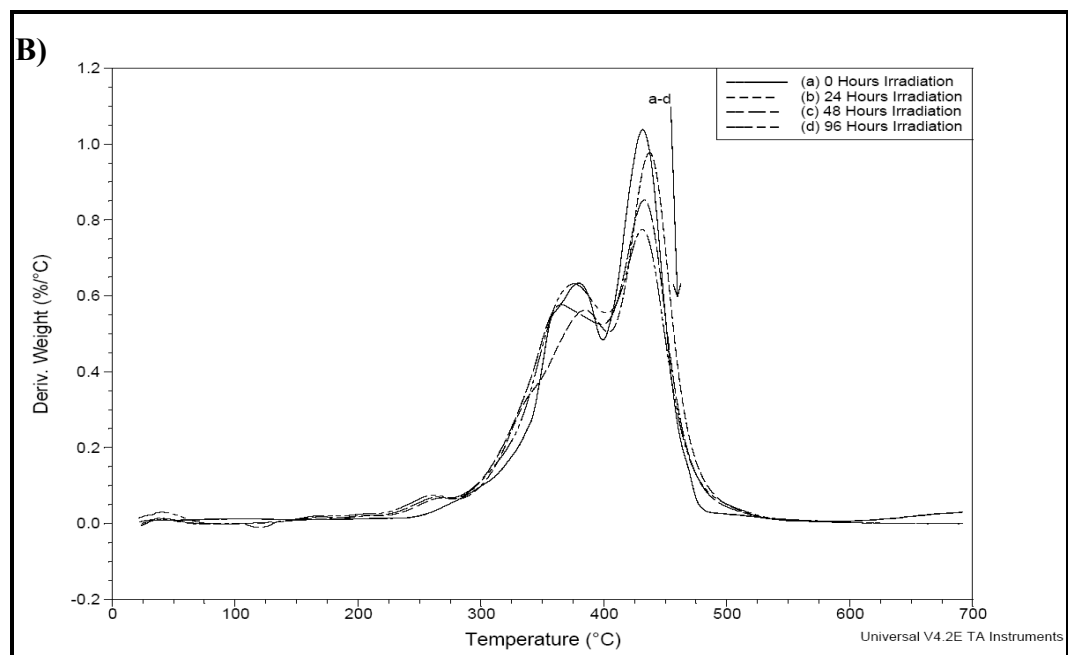
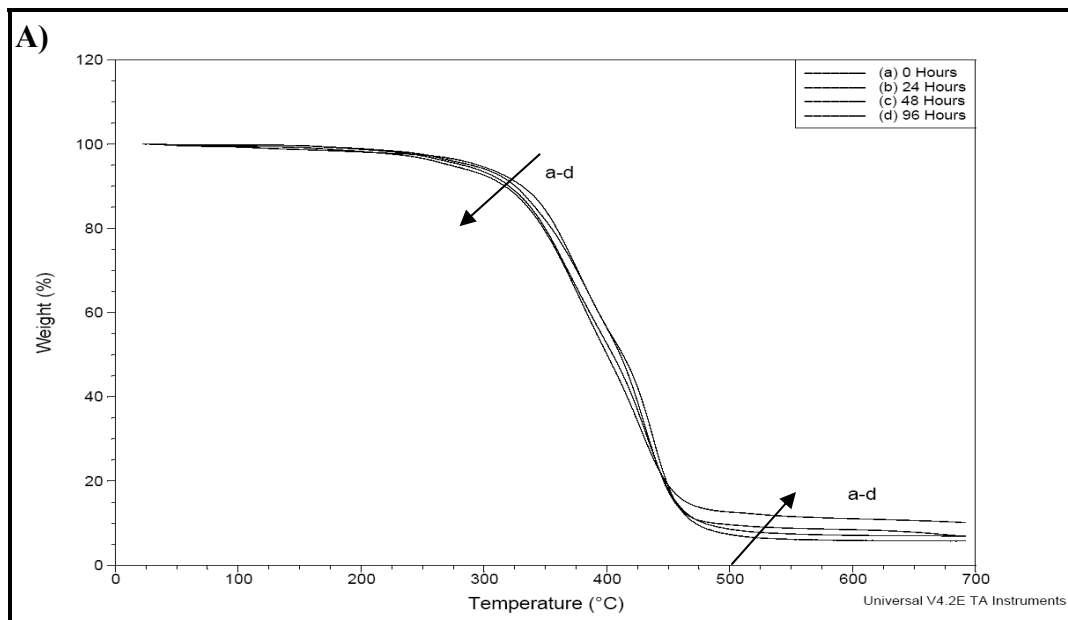


**Figure 0.7 – A) TG and B) DTG Curves for 5wt% TiO<sub>2</sub>-PU Composite - Monomer Method (a) 0 (b) 24 (c) 48 (d) 96 Hours of Irradiation.**

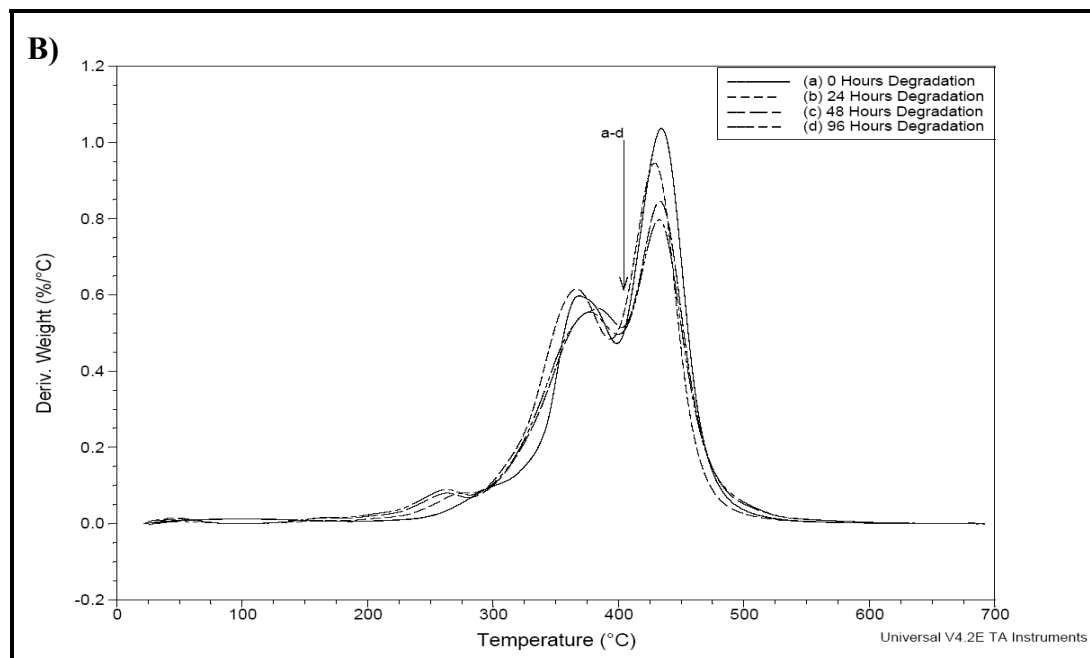
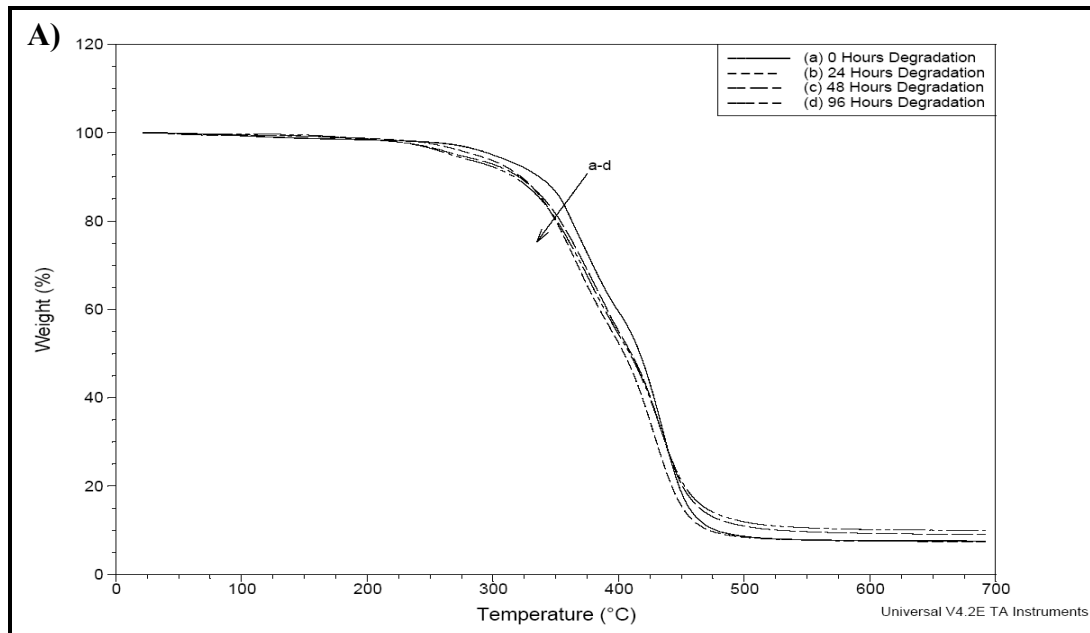


**Figure 8.8 – A) TG and B) DTG Curves for 5wt% TiO<sub>2</sub>-PU Composite – Polymer Method - for (a) 0 (b) 24 (c) 48 (d) 96 Hours of Irradiation.**

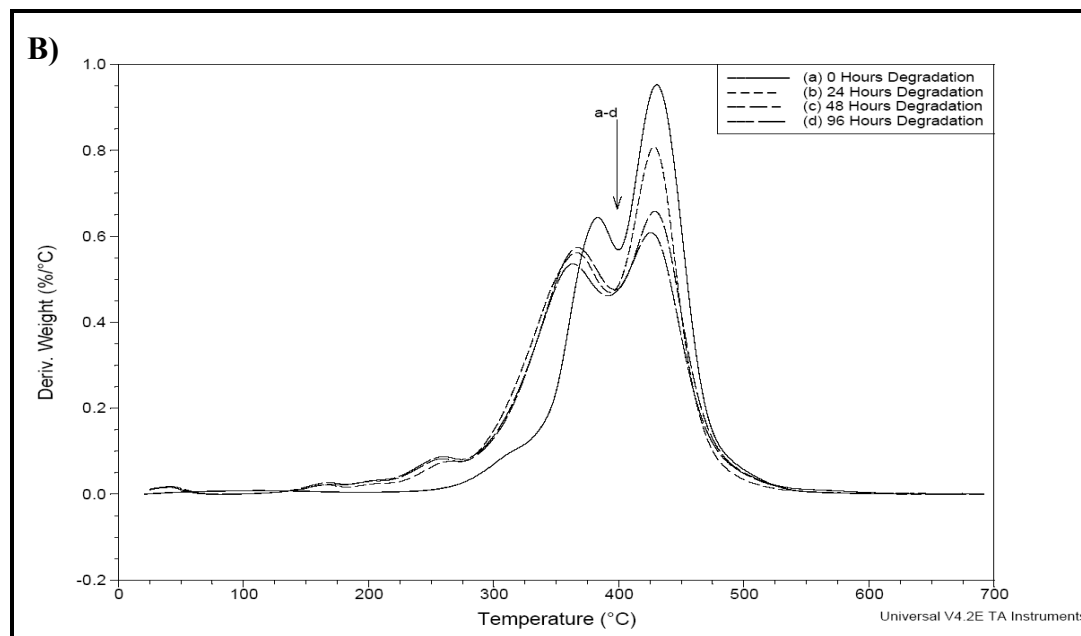
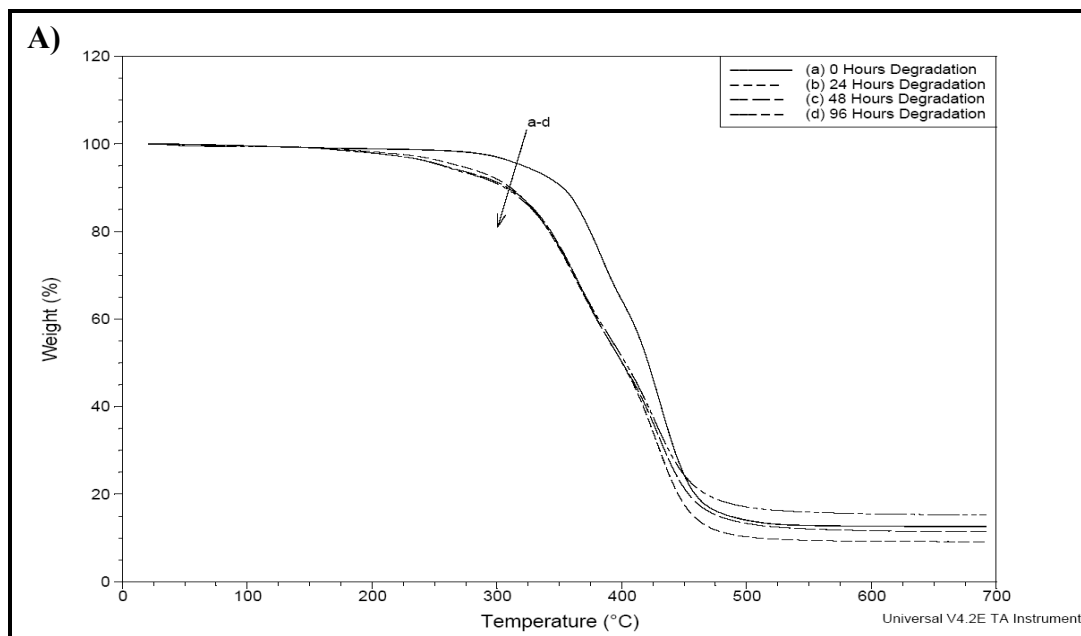


**Figure 0.9 – A) TG and B) DTG Curves for 10wt% TiO<sub>2</sub>-PU Composite – Monomer Method - for (a) 0 (b) 24 (c) 48 (d) 96 Hours of Irradiation.**

### 1.26.1 Polyurethane Samples

From Figure 6.6A and 6.6B, PU is shown to thermally decompose into two parts, i.e. the hard and soft segments. The PU begins decomposition at 0 hours of irradiation, at  $T_2^i = 277.6 \pm 0.8$  °C, corresponding to the hard segment of the polymer, and the second segment, soft segment, begins decomposition at  $T_3^i = 404.7 \pm 5.2$  °C. The maximum decomposition temperatures were shown to be  $T_2^{\max} = 370.6 \pm 3.9$  °C and  $438.0 \pm 5.2$  °C for the hard and soft segments respectively. These results are similar to that found by Basjic<sup>82</sup> for the thermal degradation of a MDI/PTMEG PU elastomeric coating. However, the hard segment in this work incorporates HMPA, to where the DTG peak for the PU samples hard segments are wider than that observed in the literature. This result is expected because the thermal degradation of HMPA is within the range of 200-400 °C as shown earlier in Figure 5.16.

After irradiation, the initial decomposition temperatures,  $T_2^i$  and  $T_3^i$ , increase to  $295.8 \pm 3.2$  °C and  $412.9 \pm 0.4$  °C, meaning that the TGA analysis describes a PU elastomeric coating that strengthens by increasing intermolecular forces upon irradiation, further curing the PU. Also, photooxidation in MDI derivative polyurethanes takes place through a quinoid route, where the urethane bridge oxidizes to the quinone-imide structure, as previously shown in Figure 6.3.

Although the hard and soft segments increase in thermal stability, as evidenced by increasing initial decomposition temperatures, the PU coating is still shown to undergo photolysis by the decreasing  $T_1^i$  from  $234.8 \pm 0.8$  °C at 0 hours of irradiation to  $198.9 \pm 1.2$  °C for 96 hours of irradiation. It is also evident that photodegradation occurs by the decreasing mass of the soft segment, from  $\Delta m_3 = 49.8 \pm 1.8\%$  at 0 hours of irradiation to  $\Delta m_3 = 38.7 \pm 1.8\%$  at 96 hours of irradiation. It was mentioned earlier that the energy of radiation for  $\lambda = 365\text{nm}$  was estimated at 328 KJ/mole or 78.5 kcal/mol. This energy is sufficient for photocatalytic reactions, although unable to break any of the bonds in polyurethane. However, as the filter on the black light is  $365 \pm 20$  nm and a wavelength of

345nm, energy of 83 kcal/mol has the ability for polyurethane degradation explaining why the PU sample underwent some photodegradation.

#### 1.26.2 5wt% TiO<sub>2</sub>-PU monomer method composite samples

From Figure 6.7, 5wt% TiO<sub>2</sub>-PU composites produced by the monomer method, is shown to thermally decompose into two parts much like the PU samples. The 5wt% TiO<sub>2</sub>-PU monomer method composites begins decomposition for 0 hours of irradiation at  $T_2^i = 288.2 \pm 1.3$  °C, corresponding to the hard segment of the polymer, and the second segment, soft segment, begins decomposition at  $T_3^i = 400.1 \pm 0.2$  °C. The maximum decomposition temperatures were shown to be  $T_2^{\max} = 381.4 \pm 1.8$  °C and  $433.6 \pm 2.1$  °C for the hard and soft segments at 0 hours of irradiation respectively. These results are similar to the TGA analysis of the PU samples mentioned previously, except for an increase in the decomposition temperatures of the hard segment and a decrease in the decomposition temperatures of the soft segment. This indicates functionalization because the increase in ionic bonds would increase the thermal stability of the hard segment seeing that the bonds are made between TiO<sub>2</sub> and the hard segment. However, as TiO<sub>2</sub> agglomerates were previously shown to exist, the non-coordinated nanoparticles in the polymer matrix can decrease the intermolecular forces between PU chains, thus decreasing the properties of the soft segment.

The TG and DTG curves in Figure 6.7 demonstrate that the soft and hard segments both decrease in thermal stability as the UV irradiation time increases, signifying that some photo reaction has taken place, where  $T_2^{\max}$  and  $T_3^{\max}$  decreased with increased time of irradiation from  $381.4 \pm 1.8$  °C to  $374.0 \pm 1.6$  °C, and from  $433.6 \pm 2.1$  °C to  $430.3 \pm 1.1$  °C, respectively. The trend error found in this data can be due to the free radical carbon molecules that are formed through photocatalytic reactions potentially combining with other free radical carbon chains, extending the polymer chains in certain areas, hence increasing the maximum rate of thermal degradation. This can also be due to TiO<sub>2</sub> agglomeration within the sample, to where uniformity between different TGA samples of the same irradiated sample may not exist, thus causing error within that given sample. This has also been found by Mills et al.<sup>16</sup> where not only are there sample unity changes

throughout one specific sample, but exact sample reproducibility is impossible. The finding by Mills also agreed with the SEM findings in Figure 5.19, where agglomeration of non-uniform TiO<sub>2</sub> molecules in each sample was found.

The most important aspect of the DTG curves in Figure 6.7B is the change in area under the curve of each segment, mainly the soft segment, because this area corresponds to the mass % of each segment. As can be seen, the area under the hard segment changes slightly with increasing irradiation, while the soft segment changes drastically from  $\Delta m_3 = 51.0 \pm 0.9\%$  at 0 hours of irradiation to  $\Delta m_3 = 41.1 \pm 0.9\%$  at 96 hours of irradiation. This change corresponds to the mass loss in the soft segment. The adjusted mass % of the hard segment, although increasing from  $41.7 \pm 0.4$  to  $47.6 \pm 0.2\%$ , is not really changing in mass %; it is the photodegradation of the soft segment that is dropping in mass that causes the increase in mass % to the hard segment. The DTG curve also shows a third thermal degradation peak ranging from  $T_1^i$  at 0 hours of irradiation of  $246.5 \pm 3.0$  °C to  $T_1^i$  at 96 hours of irradiation of  $216.7 \pm 1.2$  °C. This dramatic decrease in thermal stability also proves that smaller components are being formed through photodegradation, and are thermally decomposed at a lower temperature as the irradiation time is increased.

### 1.26.3 5wt% TiO<sub>2</sub>-PU polymer method composite samples

Similar to that for the monomer functionalization method, the polymer functionalization method for a 5wt% TiO<sub>2</sub>-PU composite experienced a significant decrease in thermal stability upon UV irradiation. Figure 6.8A and 6.8B contain the TG and DTG curves for the said samples, respectively. These curves show immediate drops in the thermal stability of the hard segment upon increased irradiation, attributed to the decrease in the initial decomposition temperature,  $T_1^i$ , from  $236.1 \pm 2.5$  °C to  $198.9 \pm 0.8$  °C. This thermal stability drop corresponds to an increase in the mass percent of this lower molecular weight material, increasing from  $\Delta m_1 = 3.9 \pm 0.1\%$  to  $\Delta m_1 = 6.7 \pm 0.1\%$ , demonstrating further photocatalytic degradation with increasing time of UV irradiation.

The DTG curve of the polymer method shows similar results to that of the monomer method in terms of the mass percentage loss of the soft segment, which significantly decreased in adjusted mass from  $\Delta m_3 = 53.2 \pm 0.4 \%$  to  $\Delta m_3 = 43.7 \pm 0.5 \%$ .

The decrease in soft segment mass % for the PU, 5wt% TiO<sub>2</sub>-PU monomer method composite, and 5wt% TiO<sub>2</sub>-PU polymer method composite are compared in Figure 6.10. Although the curves start and end at different mass percentages, the changes in mass % for all samples are similar. However, it is observed that the decrease in the soft segment of the polymer method was observed at a faster rate than what was observed in the more dispersed TiO<sub>2</sub> monomer method, as seen in Figure 6.10 where after 48 hours, no further mass loss was observed.

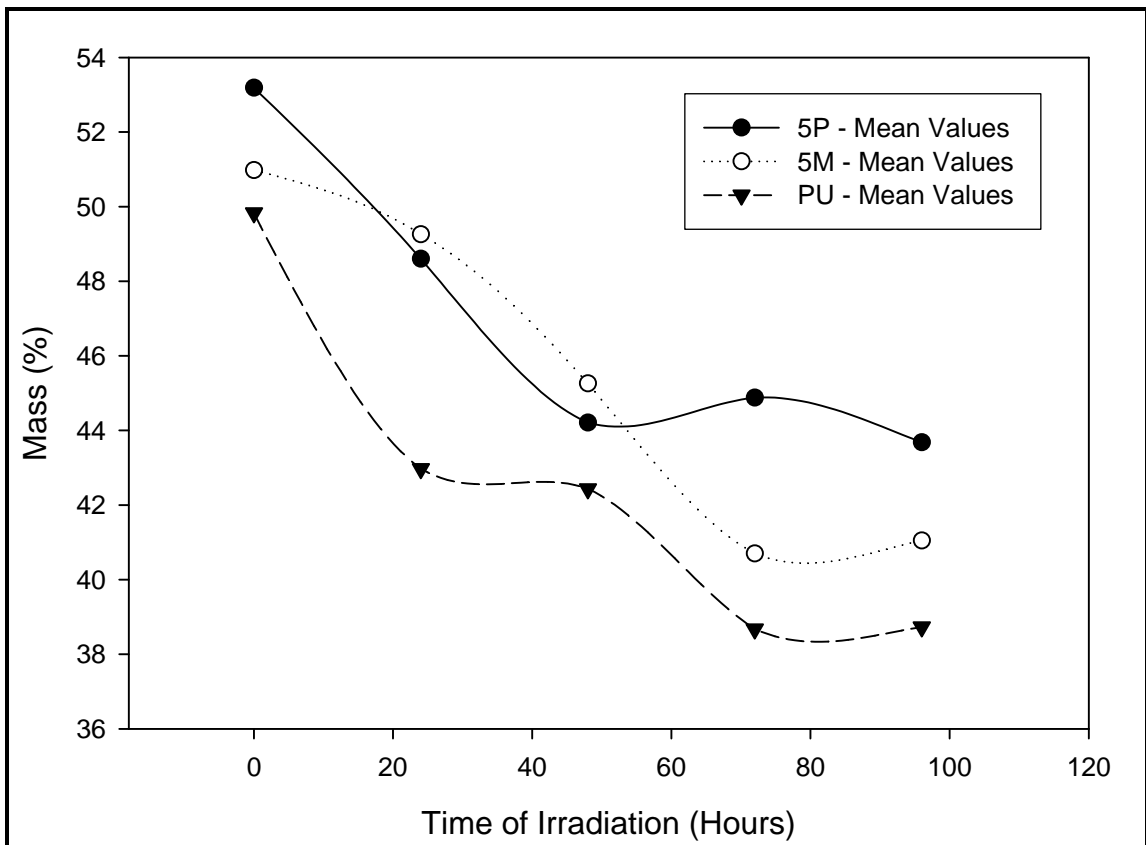


**Figure 0.10 – Soft Segment Degradation Mass Loss with Time for: PU, 5M – 5wt% TiO<sub>2</sub>-PU Monomer Method Composites, 5P – 5wt% TiO<sub>2</sub>-PU Polymer Method Composites.**

The statistical analysis for these three curves can be found using error bars in Figures A.1 – A.3 in the Appendix. These figures clearly demonstrate that the rate of soft segment photodegradation increases for the polymer functionalization method. Some of the error bars showed a rather large error, likely due to an increased amount of TiO<sub>2</sub> at that specific spot in one of the samples at that irradiation time.

#### 1.26.4 10wt% TiO<sub>2</sub>-PU monomer method composite samples

Figure 6.9A and 6.9B show the TG and DTG weight loss curves as a function of temperature peaks for this sample. The TG curve shows a rapid reduction in both the hard and soft segments, much like the polymer functionalization for 5wt% TiO<sub>2</sub>-PU composites, in which the hard segment appears to decrease rapidly. This decrease is due to the increase in  $\Delta m_1$ , where it decreases to a constant value, whereas the soft segment continually decreases in area as described in Figure 6.8. These figures show that increasing the wt% of TiO<sub>2</sub> to 10% TiO<sub>2</sub> using the monomer method has a combined effect of both the 5wt% TiO<sub>2</sub> monomer and polymer functionalization methods, because the sample contains too much mass of nano-TiO<sub>2</sub>. It has already been shown that TiO<sub>2</sub> agglomerates still exist even though there is good dispersion of TiO<sub>2</sub>. This corresponds to the data in Section 5.3 for Ti-HMPA, where a maximum functionalization percentage is reached for 25% TiO<sub>2</sub>; extra TiO<sub>2</sub> leads to increased agglomerates, achieving similar effects to the polymer functionalization method. The increase of TiO<sub>2</sub> amount in solution improves the titanium surface content, thus increasing the degradation rate, although high TiO<sub>2</sub> to polymer ratios lead to film instability.<sup>70</sup>

#### 1.26.5 Comparative TGA Analysis

Initially, it can be seen that increasing the functionalization of TiO<sub>2</sub> to PU increases the thermal stability of the hard segment in the composite, as can be seen in Figure 6.11 for 0-10% TiO<sub>2</sub>. Also, functionalization using the monomer method shows an initial increase in thermal stability. This is due mainly to the increase in ionic bonding between the carboxylic acid groups to nano TiO<sub>2</sub>. These are the strongest of the secondary forces, and are the attractive forces between positively and negatively charged ions.<sup>75</sup>

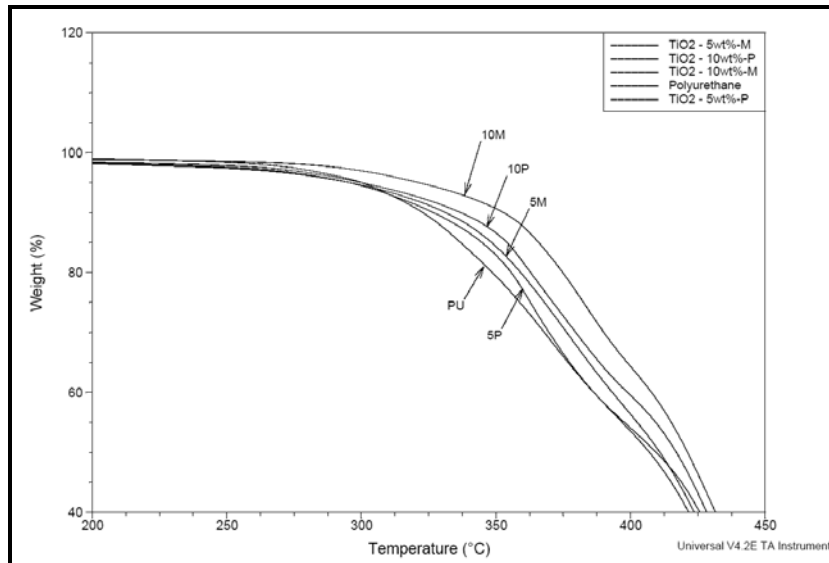


**Figure 0.11 – Comparative data at 0 hours of Irradiation for (PU) 0% TiO<sub>2</sub>, (5M) 5% TiO<sub>2</sub> – Monomer Method, (5P) 5% TiO<sub>2</sub> – Polymer Method, (10M) 10% TiO<sub>2</sub> – Monomer Method, (10P) 10% TiO<sub>2</sub> – Polymer Method.**

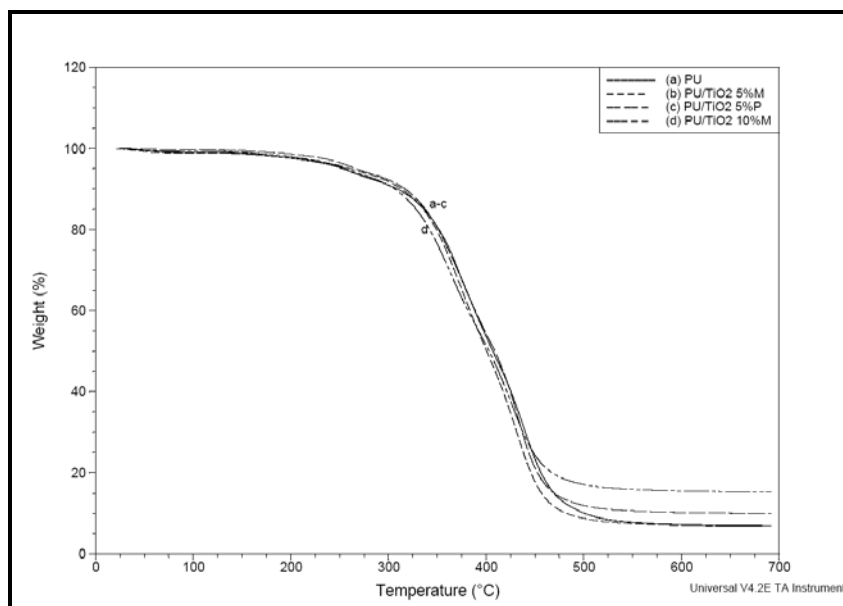


**Figure 0.12 - Comparative data at 100 hours of Irradiation for (a) 0% TiO<sub>2</sub>, (b) 5% TiO<sub>2</sub> – Monomer Method, (c) 10% TiO<sub>2</sub> – Polymer Method, (d) 10% TiO<sub>2</sub> – Monomer Method.**

However, after 96 hours of irradiation (Figure 6.12), it can be seen that the polyurethane elastomer and the 5% by weight TiO<sub>2</sub>-PU composites all decrease in thermal stability to roughly the same temperature. This further proves the problems of using a semi-closed system in which air flow and exchange were facilitated, although not controlled. Hence, as the irradiation preceded, the humidity level likely decreased, hindering photo-

oxidation. Therefore, for degradation or self cleaning to occur, humidity must be present to form a reaction, meaning that the oxidation process is the main photocatalytic process responsible for the chemical breakdown of organic materials.

However, the light penetration distance can greatly affect the photodegradation of a given PU elastomer coating, and the photocatalytic degradation of TiO<sub>2</sub>-PU composite coatings. The exact light penetration distance for the PU and its composites was not measured, but it was observed that discoloration for all experimental samples occurred, and that the degradation did not penetrate all the way through the samples, which had an average thickness of 90-100µm. As the composite was irradiated, the irradiated side of the film color changed from a white opaque color to a yellow color. However, this did not occur throughout the entire sample, as the bottom of the film remained white (compared in Figure 6.13) leading to the estimation that light penetration for a polyurethane coating is similar to that of a PVC coating studied by Cho and Choi,<sup>53</sup> 66µm. Therefore TGA analysis will not show precise photocatalytic degradation because both sides of the coating were irradiated at the same time to where the non-irradiated side of the coating had the same thermogravimetric properties as the coating at zero hours of irradiation for each sample time.

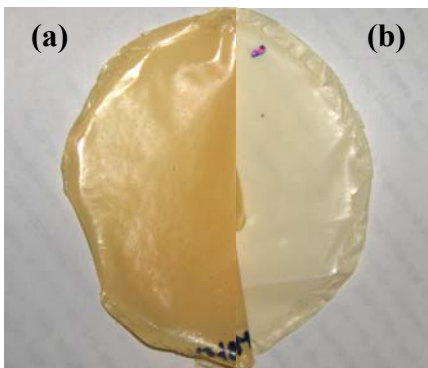


**Figure 0.13 - Digital Image for the (a) Top of the Film After UV Irradiation and (b) Bottom of the Film after UV Irradiation.**

## 1.27 Fourier Transform Infrared Analysis

TGA analysis does not indicate exactly what type of photodegradation is taking place, photolysis and/or photocatalysis. Therefore, FTIR analysis was taken to observe certain bond changes of PU and its composites.

### 1.27.1 Polyurethane Samples

Figure 6.14 compares the FTIR analysis of PU elastomers, before and after irradiation. It is evident that the PU degrades with increasing hours of irradiation due to the scission of the C-O bonds in the urethane linkage and in the PTHF ether linkage, as seen by the decrease in the absorbance of the C-O peak at  $1050\text{cm}^{-1}$ , by the formation of an aldehyde described by the slight increase at  $1710\text{cm}^{-1}$ , and by an increase in OH concentration at  $3000\text{-}3500\text{ cm}^{-1}$ .

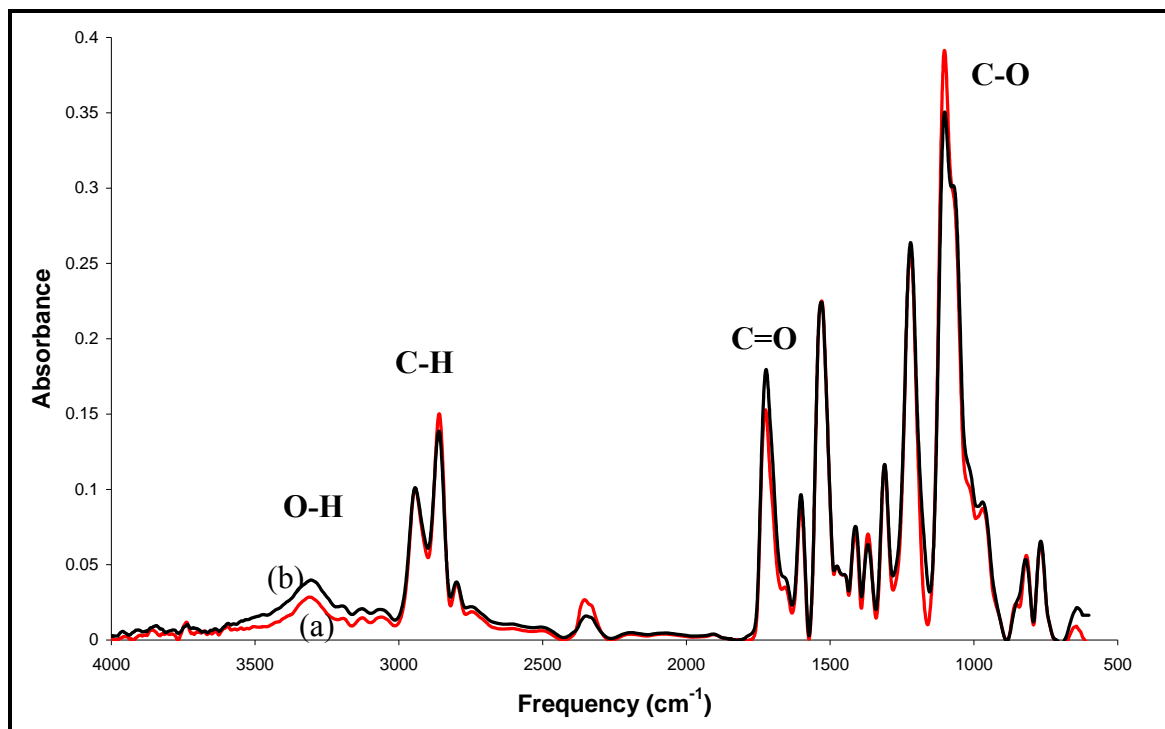


**Figure 0.14 – FTIR Analysis for Non-Functionalized PU Elastomer at (a) 0 Hours of Irradiation and (b) 100 Hours of Irradiation.**

This is consistent with the photooxidation degradation mechanisms outlined in Figure 6.4. Because the maximum energy produced by the UV lamp is not sufficient to break C-C bonds, only oxidation reactions can break the soft segment. The presence of C-H peaks at  $2800\text{-}3000\text{cm}^{-1}$  show that the formation of  $\text{CO}_2$  and  $\text{H}_2\text{O}$  were not formed from the

photooxidation of PU elastomers. This FTIR result matches that from the TGA analysis, and from the photooxidation degradation chemistry shown previously.

### 1.27.2 TiO<sub>2</sub>-PU Composite Degradation (5% monomer functionalization method)

Photocatalytic degradation of the 5wt% TiO<sub>2</sub>-PU monomer functionalization method composite material can be described further using FTIR analysis to study the type of bonds being destroyed and formed through the redox reactions. Figure 6.15 shows the FTIR spectra for the said composite in which noticeable changes in certain peaks occur.

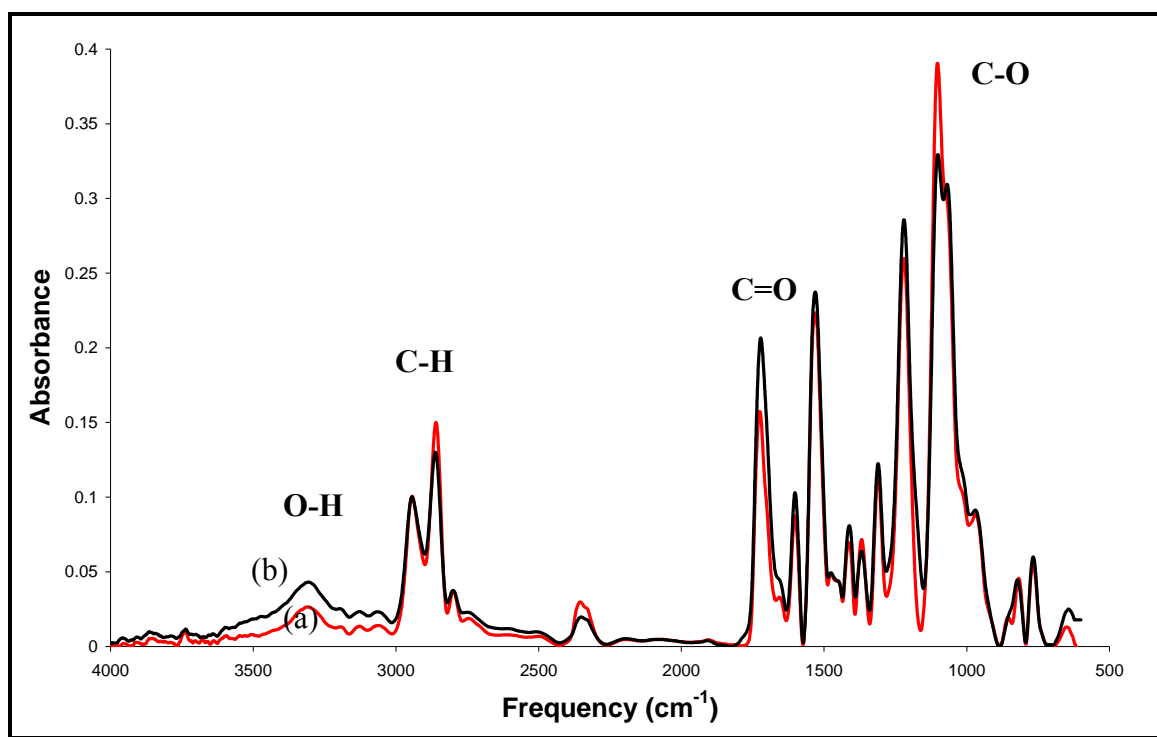


**Figure 0.15 - FTIR Analysis for 5% TiO<sub>2</sub>-PU Composite Coating Produced Through the Polymer Method at (a) 0 Hours of Irradiation and (b) 100 Hours of Irradiation.**

The increased area from 3000-3600cm<sup>-1</sup> indicates an increase in hydroxyl (OH) content in the polymer composite sample. The C-H stretch peaks from 2800-3000cm<sup>-1</sup> decrease slightly, meaning these samples do not undergo a great amount of photocatalytic degradation, but still exhibit photolysis. However, the area of a carboxylic acid OH group, 2500-3000cm<sup>-1</sup>, increases slightly, thus increasing the CH stretch peaks. Subtracting the OH area from the formed carboxylic acids, decreases the CH stretch

peaks, signifying that some photocatalytic degradation in the CH<sub>2</sub> groups of the soft segment have been converted to CO<sub>2</sub> and H<sub>2</sub>O.

The C-O-C peak at 1050cm<sup>-1</sup> also decreased, showing the urethane bond and PTHF ether groups being transformed. The C=O peak at 1710cm<sup>-1</sup> increases, likely due to the formation of aldehyde materials from photocatalytic reactions. All these characteristic peaks are similar to the results found by Lin and Lee<sup>21</sup> for a TiO<sub>2</sub>-silicone polymer composite.

### 1.27.3 TiO<sub>2</sub>-PU Composite Degradation (5% polymer functionalization method)

Figure 6.16 shows the FTIR analysis for the 5wt% TiO<sub>2</sub>-PU polymer functionalization method composite, where it is evident that the polymer method experiences much more photocatalytic degradation compared to the monomer method, and the photooxidation of the polyurethane samples. This is shown through an increase in the OH stretch with a broad peak from 3000cm<sup>-1</sup> to 3600cm<sup>-1</sup>; the decrease in C-H stretches seen from 2800cm<sup>-1</sup> to 3000cm<sup>-1</sup>; the decrease in the C-O-C stretch found at 1050cm<sup>-1</sup>; and the increase in carbonyl (C=O) groups at 1710cm<sup>-1</sup>. All these changes support the proposed photocatalytic degradation chemistry of the soft segment in the TiO<sub>2</sub>-PU composite. Horikoshi et al.<sup>81</sup> also found that incorporation of TiO<sub>2</sub> blended into PVC thin films decomposed CH<sub>2</sub> groups seen in the peaks from 2800-3000cm<sup>-1</sup> of the FTIR analysis.

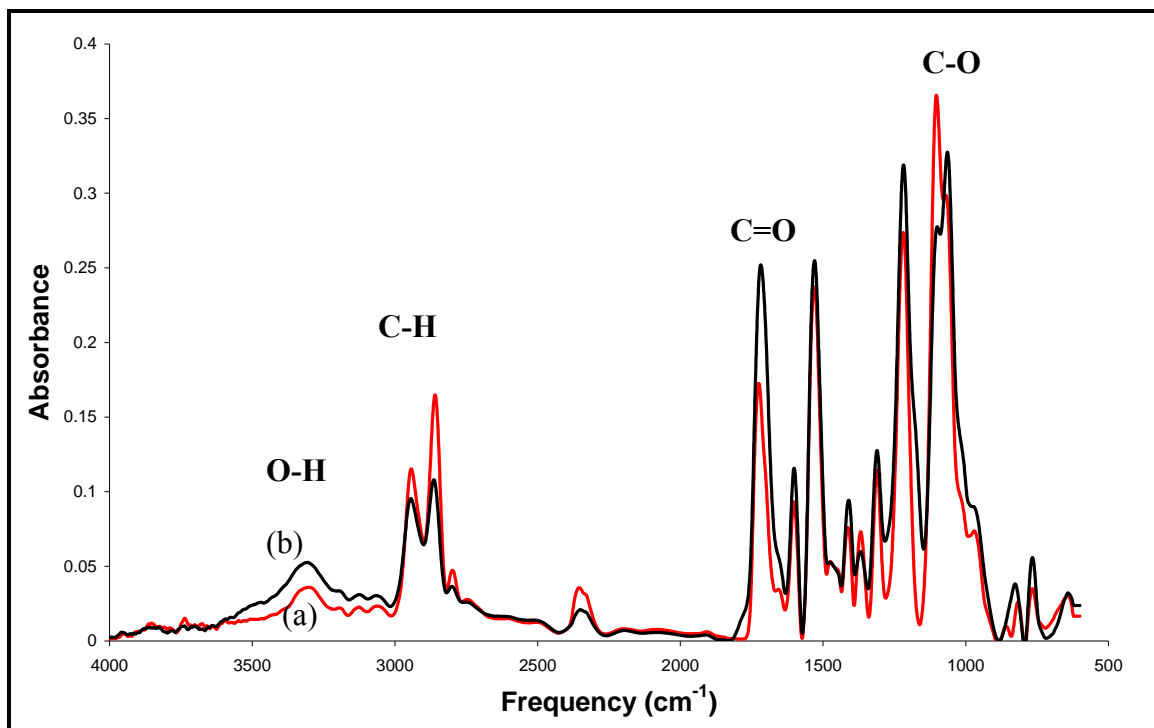


**Figure 0.16 - FTIR Analysis for 10% TiO<sub>2</sub>-PU Composite Coating Produced Through the Polymer Method at (a) 0 Hours of Irradiation and (b) 100 Hours of Irradiation.**

This data indicates that TiO<sub>2</sub> agglomerates aid in the trapping of holes and electrons, increasing the photocatalytic degradation efficiency. Kim et al.<sup>19</sup> found a different result, that micrometer-sized agglomeration significantly reduced the efficiency of photodegradation by decreasing the interface area between polymer and photocatalyst, as well as inducing rapid whitening that decreased the light penetration depth into the composite film. Zan et al stated that increasing the dispersion of TiO<sub>2</sub> nanoparticles into the polymer matrix was shown to increase polymer degradation significantly.<sup>20</sup> Increasing the dispersion of TiO<sub>2</sub> nanoparticles in polymeric systems through functionalization has been shown to decrease the size of agglomerates, increasing the photocatalytic degradation efficiency.<sup>19</sup> This was because TiO<sub>2</sub> particles will aggregate significantly in a low polarity medium if there is not sufficient steric hindrance.<sup>20</sup> However, their research only took into account the properties of surface area, and not electron-hole recombination and crystallinity of the TiO<sub>2</sub>, which are both important factors in the efficiency of photocatalytic degradation. Support against this assumption is provided by the work of Mills et al.<sup>16</sup> using FTIR analysis, in which the removal of

stearic acid by TiO<sub>2</sub> photocatalysis produced no film component other than stearic acid, and found that no gas phase products other than CO<sub>2</sub> and H<sub>2</sub>O were generated through this reaction.<sup>16</sup> However, in Mills work, the stearic acid peaks disappeared very slowly for coating samples with TiO<sub>2</sub> agglomerates in the nano range, versus coatings comprised of TiO<sub>2</sub> agglomerates in the micro range, due to a high electron-hole recombination rate.

During experiments in this work, the photocatalytic reactions took place in a semi-closed system in which air flow and H<sub>2</sub>O exchange were hindered. As the irradiation proceeded, the humidity in the air of the closed system may have decreased due to increased photo reactivity and the energy converted to heat, drying the air. It was noted by others that increasing the humidity in the air increased the conversion and concentrations of both toluene and trichloroethylene, due to the relationship of water increasing the photocatalysis reaction on the conduction band of the TiO<sub>2</sub> particles.<sup>93</sup>

Therefore, as accurate mass loss was not achieved for the reaction up to 96 hours of degradation, although the sample did show that the polymer method of functionalization experienced an increased rate of photocatalytic degradation, in which the humidity in the air was used up in the reaction in approximately 48 hours. As previously mentioned, this is attributed to the size of the TiO<sub>2</sub> agglomerates on the sample surface, where the rate of electron-hole recombination decreased compared to that which was seen in the more disperse grafting from method.

#### 1.27.4 TiO<sub>2</sub>-PU Composite Degradation (10wt% monomer functionalization method)

FTIR results in Figure 6.17 further prove the TGA analysis, where photocatalytic degradation of a 10% sample is definitely observed. This is shown through an even further increase in the broad peak ranging from 3000cm<sup>-1</sup> to 3600cm<sup>-1</sup> for OH groups; a large decrease in C-H stretches seen from 2800cm<sup>-1</sup> to 3000cm<sup>-1</sup>; the decrease in the C-O-C stretch found at 1050cm<sup>-1</sup>; and the increase in carbonyl (C=O) groups at 1710cm<sup>-1</sup>. The higher degradation of this sample is due mostly to increased mass percent of TiO<sub>2</sub> within the sample, to where the surface area of TiO<sub>2</sub> is high; reacting much faster than the other samples before the entrained water in the air is removed.

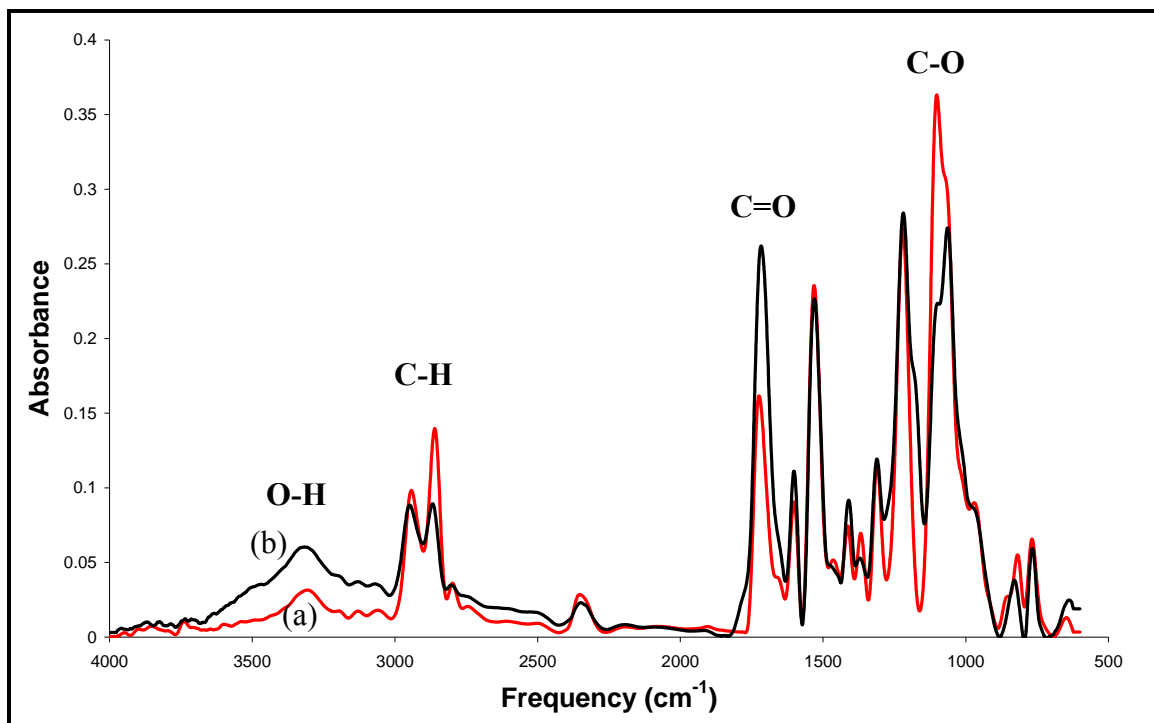


**Figure 0.17 - FTIR Analysis for 10% TiO<sub>2</sub>-PU Composite Coatings Produced Through the Monomer Method at (a) 0 Hours of Irradiation and (b) 100 Hours of Irradiation.**

Eren and Okte stated that higher percentages of nano-TiO<sub>2</sub> causes increased aggregation, reducing degradation significantly by decreasing the interface area between polymer and the photocatalytic agent, and also inducing rapid whitening that shortens the light penetration depth into the composite films.<sup>94</sup> This however contradicts what was noticed by Losito et al where they found that an increase of TiO<sub>2</sub> in solution improves the titanium surface content, thus increasing the degradation rate, although high TiO<sub>2</sub> to polymer ratios lead to film instability.<sup>70</sup> The polyurethane-TiO<sub>2</sub> composite film FTIR and TGA results for degradation both show that 10%-TiO<sub>2</sub> composite films achieved greater degradation compared to the 5%-TiO<sub>2</sub> composite films produced by the same method.

## CONCLUSIONS

It has been shown that the formulation of a NCO:OH polyurethane elastomeric coating produced the highest yield, after liquid-liquid extraction with methanol, when a ratio of 1:1.01 was utilized, producing a film with greater thermal properties. It was also found that for a fixed concentration of HMPA in 2-propanol, increasing the amount of TiO<sub>2</sub> achieved optimum functionalization by yield for 38.2 wt% TiO<sub>2</sub>, and using TGA analysis.

The functionalization via the monomer method was found to aid in the breaking up of TiO<sub>2</sub> agglomerates, giving better dispersion than the polymer functionalization method. TGA analysis showed that the hard segment of a TiO<sub>2</sub>-PU composite coating prepared by the monomer functionalization method had a higher thermal stability compared to the coatings prepared by the polymer method. However, the degradation of each of the methods showed that the polymer functionalization method experienced a higher rate of degradation according to TGA analysis, and also experienced a greater production of H<sub>2</sub>O and CO<sub>2</sub> using FTIR analysis. Hence, for a TiO<sub>2</sub>-PU composite coating, increasing the surface area of the TiO<sub>2</sub> semiconductor increased the amount of active sites for photocatalysis, but also increased the rate of electron-hole recombination, meaning that the crystallinity and defect sites of the TiO<sub>2</sub> nanoparticles play an important role in photocatalysis.

It was also shown that increasing the mass percentage of TiO<sub>2</sub> in the composite coating decreased the contact angle with water, thus increasing the wettability of the composite coating. The 5 wt% TiO<sub>2</sub>-PU elastomeric coating produced by the monomer method experienced the best industrial capabilities by being able to clean excess HMPA in air by UV irradiation yet experienced the least amount of degradation. Although the rate of cleanability was not found, it was expected that it follows the same trends as degradation rate to where the polymer functionalization method would experience a greater cleanability rate than that of the monomer method.

## RECOMMENDATIONS

TiO<sub>2</sub> photocatalysis has one major drawback, and that is the use of highly intensive UV light to carry out the photocatalytic reactions. For outdoor use, this is not an issue, however, UV light indoors is a little more difficult to obtain. It has been shown by others that phase separated semiconductors can be coupled to TiO<sub>2</sub> as a semiconductor heterojunction, by either incorporated nanoparticles or as a separate layer. At this interface, electrons and holes can migrate between the phases depending on the relative energies of their conduction and valence bands, thus either activating or deactivating the TiO<sub>2</sub> phase, depending on the choice of coupled semiconductor. Hence, by coupling a visible light absorbing semiconductor, such as CdS or WS<sub>2</sub>, with nano-TiO<sub>2</sub>, visible light generated charge carriers can be transferred to TiO<sub>2</sub> where they can induce photocatalysis and super-hydrophilicity.

Another issue with nano-TiO<sub>2</sub> photocatalysis is the electron-hole recombination rate for nano-TiO<sub>2</sub> due to the crystal structure and surface area from smaller charge separation distances. However, a solution to recombination is the incorporation of charge separators in the form of platinum or gold. Excited electrons are transferred from the irradiated conduction band of the semiconductor to the metal, preventing it from recombining with the oxidative holes. The accumulated electrons migrated to the charge carrier are able to reduce adsorbed organics on the surface,<sup>46</sup> increasing the cleanability rate because reduction reactions on the surface of a metallic charge carrier is faster than that of the semiconductor surface reduction reactions.<sup>95</sup> Another possibility to decrease this recombination is TiO<sub>2</sub> surface modification to increase crystallinity, and decreasing surface defect site while keeping a large surface area. This can increase the photoreactivity and transparency of TiO<sub>2</sub> and can be accomplished by making TiO<sub>2</sub> nanofibers or nanotubes.

Also, the superhydrophilicity of the TiO<sub>2</sub> decreases drastically when not exposed to UV light. It is required that the water contact angle rises slowly in a dark place and stays low for a long time. For industrial processes, the coating is not always irradiated by UV light such as at night or on a cloudy day. However, research has shown that adding SiO<sub>2</sub> to

TiO<sub>2</sub>, the contact angle of water is low immediately after production, and the maintenance of hydrophilicity in a dark place is also good when 30-40 mole% SiO<sub>2</sub> is incorporated into the coating. Also, TiO<sub>2</sub>/SiO<sub>2</sub> composite coatings have been found to improve photocatalysis for 10-20 mole% SiO<sub>2</sub> in the composite.<sup>1</sup>

On the polymer side, polyurethanes have much more applications in paints and coatings using aliphatic isocyanates rather than aromatic ones. Researching the effects of TiO<sub>2</sub> photocatalysis on aliphatic isocyanates, including wettability, cleanability, and self degradation is a project on its own and could prove very valuable industrially.

## REFERENCES

1. Guan, K. H., Relationship between photocatalytic activity, hydrophilicity and self-cleaning effect of TiO<sub>2</sub>/SiO<sub>2</sub> films. *Surface & Coatings Technology* 2005, 191, (2-3), 155-160.
2. Kuisma, R.; Froberg, L.; Kymalainen, H. R.; Pesonen-Leinonen, E.; Piispanen, M.; Melamies, P.; Hautala, M.; Sjoberg, A. M.; Hupa, L., Microstructure and cleanability of uncoated and fluoropolymer, zirconia and titania coated ceramic glazed surfaces. *Journal of the European Ceramic Society* 2007, 27, (1), 101-108.
3. Fujishima, A.; Honda, K., Electrochemical Photolysis of Water at a Semiconductor. *Nature* 1972, 238, 37.
4. Dibble, L. A.; Raupp, G. B., Fluidized-Bed Photocatalytic Oxidation of Trichloroethylene in Contaminated Airstreams. *Environmental Science & Technology* 1992, 26, (3), 492-495.
5. Lim, T. H.; Jeong, S. M.; Kim, S. D.; Gyenis, J., Photocatalytic decomposition of NO by TiO<sub>2</sub> particles. *Journal of Photochemistry and Photobiology a-Chemistry* 2000, 134, (3), 209-217.
6. Nam, W.; Kim, J.; Han, G. Y., Photocatalytic oxidation of methyl orange in a three-phase fluidized bed reactor. *Chemosphere* 2002, 47, (9), 1019-1024.
7. Larson, S. A.; Widegren, J. A.; Falconer, J. L., Transient studies of 2-propanol photocatalytic oxidation on titania. *Journal of Catalysis* 1995, 157, (2), 611-625.
8. Vidal, A. J. M.; Soria, J.; Augugliaro, V.; Loddo, V., Oxidation of ethanol in gas phase via heterogeneous photocatalysis. *Chemical and Biochemical Engineering Quarterly* 1997, 11, (2), 89-95.
9. Zhao, J.; Yang, X. D., Photocatalytic oxidation for indoor air purification: a literature review. *Building and Environment* 2003, 38, (5), 645-654.
10. Sauer, M. L.; Ollis, D. F., Acetone Oxidation in a Photocatalytic Monolith Reactor. *Journal of Catalysis* 1994, 149, (1), 81-91.
11. Luo, Y.; Ollis, D. F., Heterogeneous photocatalytic oxidation of trichloroethylene and toluene mixtures in air: Kinetic promotion and inhibition, time-dependent catalyst activity. *Journal of Catalysis* 1996, 163, (1), 1-11.
12. Agustina, T. E.; Ang, H. M.; Vareek, V. K., A review of synergistic effect of photocatalysis and ozonation on wastewater treatment. *Journal of Photochemistry and Photobiology C: Photochemistry Reviews* 2005, 6, 264-273.

13. Sánchez, L.; Peral, J.; Domènech, X., Aniline degradation by combined photocatalysis and ozonation. *Applied Catalysis B: Environmental* 1998, 19, 59-65.
14. Wang, S.; Shiraishi, F.; Nakano, K., A synergistic effect of photocatalysis and ozonation on decomposition of formic acid in an aqueous solution. *Chemical Engineering Journal* 2002, 87, 261-271
15. Zhang, L.; Kanki, T.; Sano, N.; Toyoda, A., Development of TiO<sub>2</sub> photocatalyst reaction for water purification. *Separation and Purification Technology* 2003, 31, 105-110.
16. Mills, A.; Lepre, A.; Elliott, N.; Bhopal, S.; Parkin, I. P.; O'Neill, S. A., Characterisation of the photocatalyst Pilkington Activ (TM): a reference film photocatalyst? *Journal of Photochemistry and Photobiology a-Chemistry* 2003, 160, (3), 213-224.
17. Parkin, I. P.; Palgrave, R. G., Self-cleaning coatings. *Journal of Materials Chemistry* 2005, 15, (17), 1689-1695.
18. Kemmitt, T.; Al-Salim, N. I.; Waterland, M.; Kennedy, V. J.; Markwitz, A., Photocatalytic titania coatings. *Current Applied Physics* 2004, 4, (2-4), 189-192.
19. Kim, S. H.; Kwak, S. Y.; Suzuki, T., Photocatalytic degradation of flexible PVC/TiO<sub>2</sub> nanohybrid as an eco-friendly alternative to the current waste landfill and dioxin-emitting incineration of post-use PVC. *Polymer* 2006, 47, (9), 3005-3016.
20. Zan, L.; Tian, L. H.; Liu, Z. S.; Peng, Z. H., A new polystyrene-TiO<sub>2</sub> nanocomposite film and its photocatalytic degradation. *Applied Catalysis a-General* 2004, 264, (2), 237-242.
21. Lin, L. H.; Lee, H. T., A new modified silicone-TiO<sub>2</sub> polymer composite film and its photocatalytic degradation. *Journal of Applied Polymer Science* 2006, 102, (4), 3341-3344.
22. Chen, X. D.; Wang, Z.; Liao, Z. F.; Mai, Y. L.; Zhang, M. Q., Roles of anatase and rutile TiO<sub>2</sub> nanoparticles in photooxidation of polyurethane. *Polymer Testing* 2007, 26, (2), 202-208.
23. Nakajima, A.; Hashimoto, K.; Watanabe, T., Recent studies on super-hydrophobic films. *Monatshefte Fur Chemie* 2001, 132, (1), 31-41.
24. Hunter, R. J., *Foundations of colloid science*. 2nd ed.; Oxford University Press: Oxford, UK ; New York, 2001; p xii, 806 p.
25. Butt, H.-J.; Graf, K.; Kappl, M., *Physics and chemistry of interfaces*. 2nd, rev. and enl. ed.; Wiley-VCH ;

John Wiley, distributor]: Weinheim  
[Chichester, 2006; p xii, 386 p.

26. Coulson, S. R.; Woodward, I.; Badyal, J. P. S.; Brewer, S. A.; Willis, C., Super-repellent composite fluoropolymer surfaces. *Journal of Physical Chemistry B* 2000, 104, (37), 8836-8840.
27. Marmur, A., The lotus effect: Superhydrophobicity and metastability. *Langmuir* 2004, 20, (9), 3517-3519.
28. Guo, C. W.; Feng, L.; Zhai, J.; Wang, G. J.; Song, Y. L.; Jiang, L.; Zhu, D. B., Large-area fabrication of a nanostructure-induced hydrophobic surface from a hydrophilic polymer. *Chemphyschem* 2004, 5, (5), 750-753.
29. Furstner, R.; Barthlott, W.; Neinhuis, C.; Walzel, P., Wetting and self-cleaning properties of artificial superhydrophobic surfaces. *Langmuir* 2005, 21, (3), 956-961.
30. Benedix, R.; Dehn, F.; Quaas, J.; Orgass, M., Application of Titanium Dioxide Photocatalysis to Create Self-Cleaning Building Materials. *Leipzig Annual Civil Engineering Report* 2000, 5, 157-168.
31. Bico, J.; Marzolin, C.; Quere, D., Pearl drops. *Europhysics Letters* 1999, 47, (2), 220-226.
32. Shibuichi, S.; Onda, T.; Satoh, N.; Tsujii, K., Super water-repellent surfaces resulting from fractal structure. *Journal of Physical Chemistry* 1996, 100, (50), 19512-19517.
33. Chen, W.; Fadeev, A. Y.; Hsieh, M. C.; Oner, D.; Youngblood, J.; McCarthy, T. J., Ultrahydrophobic and ultralyophobic surfaces: Some comments and examples. *Langmuir* 1999, 15, (10), 3395-3399.
34. Cassie, A. B. D.; Baxter, S., Wettability of Porous Surfaces. *Transactions of the Faraday Society* 1944, 40, 546 - 551.
35. Kutal, C.; Serpone, N.; American Chemical Society. Division of Inorganic Chemistry., *Photosensitive metal-organic systems : mechanistic principles and applications*. American Chemical Society: Washington, DC, 1993; p xiii, 449 p.
36. Herrmann, J. M., Heterogeneous photocatalysis: fundamentals and applications to the removal of various types of aqueous pollutants. *Catalysis Today* 1999, 53, (1), 115-129.
37. Serpone, N.; Pelizzetti, E., *Photocatalysis : fundamentals and applications*. Wiley: New York ; Toronto, 1989; p x, 650 p.

38. Wold, A., Photocatalytic Properties of  $\text{TiO}_2$ . *Chemistry of Materials* 1993, 5, (3), 280-283.
39. Kaneko, M.; Okura, I., *Photocatalysis : science and technology*. Kodansha ; Springer: Tokyo  
Berlin ; New York, 2002; p xvi, 356 p.
40. Ohtani, B.; Ogawa, Y.; Nishimoto, S., Photocatalytic activity of amorphous-anatase mixture of titanium(IV) oxide particles suspended in aqueous solutions. *Journal of Physical Chemistry B* 1997, 101, (19), 3746-3752.
41. Ohtani, B.; Zhang, S.; Handa, J.; Kajiwara, H.; Nishimoto, S.; Kagiya, T., Photocatalytic Activity of Titanium(IV) Oxide Prepared from Titanium(IV) Tetra-2-Propoxide - Reaction in Aqueous Silver Salt-Solutions. *Journal of Photochemistry and Photobiology a-Chemistry* 1992, 64, (2), 223-230.
42. Diebold, U., The surface science of titanium dioxide. *Surface Science Reports* 2003, 48, (5-8), 53-229.
43. Kopf, P.; Gilbert, E.; Eberle, S. H.,  $\text{TiO}_2$  photocatalytic oxidation of monochloroacetic acid and pyridine: influence of ozone. *Journal of Photochemistry and Photobiology a-Chemistry* 2000, 136, (3), 163-168.
44. Fujishima, A.; Rao, T. N.; Tryk, D. A., Titanium dioxide photocatalysis. *Journal of Photochemistry and Photobiology, C: Photochemistry Reviews* 2000, 1, (1), 1-21
45. Hagfeldt, A.; Graetzel, M., Light-Induced Redox Reactions in Nanocrystalline Systems. *Chemical Reviews* 1995, 95, (1), 49-68.
46. Sun, B.; Smirniotis, P. G., Interaction of anatase and rutile  $\text{TiO}_2$  particles in aqueous photooxidation. *Catalysis Today* 2003, 88 (1-2), 49-59
47. Landsberg, P. T., *Recombination in semiconductors*. Cambridge University Press: Cambridge ; New York, 1991; p xxii, 595 p.
48. Martin, S. T.; Herrmann, H.; Choi, W. Y.; Hoffmann, M. R., Time-Resolved Microwave Conductivity .1.  $\text{TiO}_2$  Photoreactivity and Size Quantization. *Journal of the Chemical Society-Faraday Transactions* 1994, 90, (21), 3315-3322.
49. Martin, S. T.; Herrmann, H.; Hoffmann, M. R., Time-Resolved Microwave Conductivity .2. Quantum-Sized  $\text{TiO}_2$  and the Effect of Adsorbates and Light-Intensity on Charge-Carrier Dynamics. *Journal of the Chemical Society-Faraday Transactions* 1994, 90, (21), 3323-3330.
50. Carp, O.; Huisman, C. L.; Reller, A., Photoinduced reactivity of titanium dioxide. *Progress in Solid State Chemistry* 2004, 32, (1-2), 33-177.

51. Bickley, R. I.; Gonzalezcarreno, T.; Lees, J. S.; Palmisano, L.; Tilley, R. J. D., A Structural Investigation of Titanium-Dioxide Photocatalysts. *Journal of Solid State Chemistry* 1991, 92, (1), 178-190.
52. Linsebigler, A. L.; Lu, G. Q.; Yates, J. T., Photocatalysis on TiO<sub>2</sub> Surfaces - Principles, Mechanisms, and Selected Results. *Chemical Reviews* 1995, 95, (3), 735-758.
53. Cho, S. M.; Choi, W. Y., Solid-phase photocatalytic degradation of PVC-TiO<sub>2</sub> polymer composites. *Journal of Photochemistry and Photobiology a-Chemistry* 2001, 143, (2-3), 221-228.
54. Kemp, T. J.; McIntyre, R. A., Transition metal-doped titanium(IV) dioxide: Characterisation and influence on photodegradation of poly(vinyl chloride). *Polymer Degradation and Stability* 2006, 91, (1), 165-194.
55. Poznyak, S. K.; Kokorin, A. I.; Kulak, A. I., Effect of electron and hole acceptors on the photoelectrochemical behaviour of nanocrystalline microporous TiO<sub>2</sub> electrodes. *Journal of Electroanalytical Chemistry* 1998, 442, (1-2), 99-105.
56. Sui, R. H.; Rizkalla, A. S.; Charpentier, P. A., Formation of titania nanofibers: A direct sol-gel route in supercritical CO<sub>2</sub>. *Langmuir* 2005, 21, (14), 6150-6153.
57. Bach, U.; Lupo, D.; Comte, P.; Moser, J. E.; Weissortel, F.; Salbeck, J.; Spreitzer, H.; Gratzel, M., Solid-state dye-sensitized mesoporous TiO<sub>2</sub> solar cells with high photon-to-electron conversion efficiencies. *Nature* 1998, 395, (6702), 583-585.
58. Jones, A. C.; Chalker, P. R., Some recent developments in the chemical vapour deposition of electroceramic oxides. *Journal of Physics D-Applied Physics* 2003, 36, (6), R80-R95.
59. Hupa, L.; Bergman, R.; Froberg, L.; Vane-Tempest, S.; Hupa, M.; Kronberg, T.; Pesonen-Leinonen, E.; Sjoberg, A. M., Chemical resistance and cleanability of glazed surfaces. *Surface Science* 2005, 584, (1), 113-118.
60. Takagi, K.; Makimoto, T.; Hiraiwa, H.; Negishi, T., Photocatalytic, antifogging mirror. *Journal of Vacuum Science & Technology a-Vacuum Surfaces and Films* 2001, 19, (6), 2931-2935.
61. Watanabe, T.; Fukayama, S.; Miyauchi, M.; Fujishima, A.; Hashimoto, K., Photocatalytic activity and photo-induced wettability conversion of TiO<sub>2</sub> thin film prepared by sol-gel process on a soda-lime glass. *Journal of Sol-Gel Science and Technology* 2000, 19, (1-3), 71-76.
62. Sung, L.-P.; Scierka, S.; Baghai-Anaraki, M.; Ho, D. L. In *Characterization of Metal-Oxide Nanoparticles: Synthesis and Dispersion in Polymeric Coatings*,

Nanomaterials for Structural Applications 2002; Berndt, C. C.; Fischer, T. E.; Ovid'ko, I.; Skandan, G.; Tsakalakos, T., Eds. Materials Research Society: 2002.

63. Khaled, S. M.; Sui, R.; Charpentier, P. A.; Rizkalla, A. S., Synthesis of TiO<sub>2</sub>-PMMA Nanocomposite: Using Methacrylic Acid as a Coupling Agent *Langmuir* 2007, 23, (7), 3988-3995.
64. Jordan, J.; Jacob, K. I.; Tannenbaum, R.; Sharaf, M. A.; Jasiuk, I., Experimental trends in polymer nanocomposites - a review. *Materials Science and Engineering a-Structural Materials Properties Microstructure and Processing* 2005, 393, (1-2), 1-11.
65. Jung, Y. C.; Sahoo, N. G.; Cho, J. W., Polymeric nanocomposites of polyurethane block copolymers and functionalized multi-walled carbon nanotubes as crosslinkers. *Macromolecular Rapid Communications* 2006, 27, (2), 126-131.
66. Mansky, P.; Liu, Y.; Huang, E.; Russell, T. P.; Hawker, C., Controlling polymer-surface interactions with random copolymer brushes. *Science* 1997, 275, (5305), 1458-1460.
67. Minko, S.; Gafijchuk, G.; Sidorenko, A.; Voronov, S., Radical Polymerization Initiated from a Solid Substrate. 1. Theoretical Background. *Macromolecules* 1999, 32, (14), 4525-4531.
68. Lott, J. R., Reversible Addition-Fragmentation Chain-Transfer (RAFT) Polymerization in Grafting Polymer Chains from TiO<sub>2</sub> Nanoparticles. In Rochester Institute of Technology: 2006; pp 1-79.
69. Sathiyarayanan, S.; Azim, S. S.; Venkatachari, G., A new corrosion protection coating with polyaniline-TiO<sub>2</sub> composite for steel. *Electrochimica Acta* 2007, 52, (5), 2068-2074.
70. Losito, I.; Amorisco, A.; Palmisano, F.; Zambonin, P. G., X-ray photoelectron spectroscopy characterization of composite TiO<sub>2</sub>-poly(vinylidene fluoride) films synthesised for applications in pesticide photocatalytic degradation. *Applied Surface Science* 2005, 240, (1-4), 180-188.
71. Liao, L. C. K.; Tung, M. T., Kinetic investigation of photocatalytic effects on poly(vinyl butyral) photodegradation. *Industrial & Engineering Chemistry Research* 2006, 45, (7), 2199-2205.
72. Kemp, T. J.; McIntyre, R. A., Influence of transition metal-doped titanium(IV) dioxide on the photodegradation of polyethylene. *Polymer Degradation and Stability* 2006, 91, (12), 3020-3025.

73. Kemp, T. J.; McIntyre, R. A., Influence of transition metal-doped titanium(IV) dioxide on the photodegradation of polystyrene. *Polymer Degradation and Stability* 2006, 91, (12), 3010-3019.
74. Li, C.; Yu, X.; Speckhard, T. A.; Cooper, S. L., Synthesis and Properties of Polycyanoethylmethylsiloxane Polyurea Urethane Elastomers - a Study of Segmental Compatibility. *Journal of Polymer Science Part B-Polymer Physics* 1988, 26, (2), 315-337.
75. Szycher, M., *Szycher's handbook of polyurethanes*. CRC Press: Boca Raton, 1999; p 1 v. (various pagings).
76. Alibeik, S.; Rizkalla, A. S.; Mequanint, K., The effect of thiolation on the mechanical and protein adsorption properties of polyurethanes. *European Polymer Journal* 2007, 43, (4), 1415-1427.
77. Yu, X.; Nagarajan, M. R.; Li, C.; Gibson, P. E.; Cooper, S. L., Poly(chloropropylmethyltrimethylsiloxane) - polyurethane elastomers: Synthesis and properties of segmented copolymers related to zwitterionomers. *Journal of Polymer Science Part B: Polymer Physics* 1986, 24, 2681-2701.
78. Gratzel, M., Solar energy conversion by dye-sensitized photovoltaic cells. *Inorganic Chemistry* 2005, 44, (20), 6841-6851.
79. Mao, C. B.; Li, H. D.; Cui, F. Z.; Feng, Q. L.; Ma, C. L., The functionalization of titanium with EDTA to induce biomimetic mineralization of hydroxyapatite. *Journal of Materials Chemistry* 1999, 9, (10), 2573-2582.
80. Hojjati, B.; Sui, R. H.; Charpentier, P. A., Synthesis of TiO<sub>2</sub>/PAA nanocomposite by RAFT polymerization. *Polymer* 2007, 48, (20), 5850-5858.
81. Horikoshi, S.; Serpone, N.; Hisamatsu, Y.; Hidaka, H., Photocatalyzed degradation of polymers in aqueous semiconductor suspensions. 3. Photooxidation of a solid polymer: TiO<sub>2</sub>-blended poly(vinyl chloride) film. *Environmental Science & Technology* 1998, 32, (24), 4010-4016.
82. Bajsic, E. G.; Rek, V., Thermal stability of polyurethane elastomers before and after UV irradiation. *Journal of Applied Polymer Science* 2001, 79, (5), 864-873.
83. Vijayalakshmi, S. P.; Madras, G., Photocatalytic degradation of poly(ethylene oxide) and polyacrylamide. *Journal of Applied Polymer Science* 2006, 100, (5), 3997-4003.
84. Prasad-Shastri, V.; Lipski, A. M.; Sy, J. C.; Znidarsic, W.; Choi, H.; Chen, I. W., Nano-scale engineering of surfaces - Functionalized Nanoparticles as Versatile Tools for the Introduction of Biomimetics on Surfaces. In *NATO-Advance Study Institute (ASI)*

*Nanoengineered Nanofibrous Materials*, University of Pennsylvania, Philadelphia: Antalya, Turkey, 2003; pp 255-262.

85. Hwang, K. S.; Lee, S. O.; Kang, B. A.; Yun, Y. H.; Shim, Y. A.; Oh, J. S.; Yang, S. H., Transparent titanium dioxide film with nanocrystalline structure by using a titanium naphthenate. *Journal of Materials Science Letters* 2003, 22, (4), 307– 309.
86. Karunagaran, B.; Rajendra-Kumar, R. T.; Viswanathan, C.; Mangalaraj, D.; Narayandass, S. K.; Mohan-Rao, G., Optical constants of DC magnetron sputtered titanium dioxide thin films measured by spectroscopic ellipsometry. *Crystal Research and Technology* 2003, 38,, (9), 773-778.
87. Šícha, J.; Herman, D.; Musil, J.; Strýhal, Z.; Pavlíket, J., Surface Morphology of Magnetron Sputtered TiO<sub>2</sub> Films. *Šícha, Jan; Herman, David; Musil, Jindřich; Strýhal, Zdenek; et. al. pp. S345 - S349* 2007, 4, (S1), S345 - S349
88. Lee, H. K.; Ko, S. W., Structure and Thermal-Properties of Polyether Polyurethaneurea Elastomers. *Journal of Applied Polymer Science* 1993, 50, (7), 1269-1280.
89. Hoyle, C. E.; No, Y. G.; Malone, K. G.; Thames, S. F.; Creed, D., Laser Flash-Photolysis of a 4,4'-Methylenebis(Phenyl Isocyanate) (Mdi) Based Polyurethane and Model Carbamates. *Macromolecules* 1988, 21, (9), 2727-2730.
90. Liaw, D. J.; Lin, S. P.; Liaw, B. Y., Photolysis of bisphenol-based polyurethanes in solution. *Journal of Polymer Science Part a-Polymer Chemistry* 1999, 37, (9), 1331-1339.
91. Lee, D. K.; Tsai, H. B., Properties of segmented polyurethanes derived from different diisocyanates. *Journal of Applied Polymer Science* 2000, 75, (1), 167-174.
92. Hidaka, H.; Suzuki, Y.; Nohara, K.; Horikoshi, S.; Hisamatsu, Y.; Pelizzetti, E.; Serpone, N., Photocatalyzed degradation of polymers in aqueous semiconductor suspensions .1. Photooxidation of solid particles of polyvinylchloride. *Journal of Polymer Science Part a-Polymer Chemistry* 1996, 34, (7), 1311-1316.
93. Obee, T. N.; Hay, S. O., Effects of moisture and temperature on the photooxidation of ethylene on Titania. *Environmental Science & Technology* 1997, 31, (7), 2034-2038.
94. Eren, T.; Okte, A. N., Polymerization of methacryl and triethoxysilane functionalized stearate ester: Titanium dioxide a composite films and their photocatalytic degradations. *Journal of Applied Polymer Science* 2007, 105, (3), 1426-1436.
95. Hoffmann, M. R.; Martin, S. T.; Choi, W.; Bahnemann, D. W., Environmental Applications of Semiconductor Photocatalysis. *Chemical Reviews* 1995, 95, (1), 69-96.

96. Wade, L. G., *Organic chemistry*. 6th ed.; Pearson Prentice Hall: Upper Saddle River, N.J., 2006; p xli, 1262, 7, 1, 14 p.

## APPENDIX A

Table 0.1 – Raw Kinetic Data for the Functionalization of HMPA – Peak 1710cm<sup>-1</sup>

Time	Peak Area	Conversion	x * Mo	[M]	ln([Mo]/[M])
0.0000	0.1970	0.0000	0.0000	0.4030	0.0000
60.0000	0.1970	0.0000	0.0000	0.4030	0.0000
120.0000	0.1970	0.0000	0.0000	0.4030	0.0000
180.0000	0.1970	0.0000	0.0000	0.4030	0.0000
240.0000	0.1970	0.0000	0.0000	0.4030	0.0000
300.0000	0.1970	0.0000	0.0000	0.4030	0.0000
360.0000	0.1880	0.0457	0.0184	0.3846	0.0468
420.0000	0.1470	0.2538	0.1023	0.3007	0.2928
480.0000	0.1180	0.4010	0.1616	0.2414	0.5125
540.0000	0.0970	0.5076	0.2046	0.1984	0.7085
600.0000	0.0840	0.5736	0.2312	0.1718	0.8524
660.0000	0.0780	0.6041	0.2434	0.1596	0.9265
720.0000	0.0790	0.5990	0.2414	0.1616	0.9138
780.0000	0.0785	0.6015	0.2424	0.1606	0.9201
840.0000	0.0780	0.6041	0.2434	0.1596	0.9265
900.0000	0.0780	0.6041	0.2434	0.1596	0.9265

**Table 0.2 - Raw Kinetic Data for the Functionalization of HMPA – Peak 1050cm<sup>-1</sup>**

<b>Time</b>	<b>Peak Area</b>	<b>Conversion</b>	<b>x * Mo</b>	<b>[M]</b>	<b>ln([Mo]/[M])</b>
0.0000	0.3320	0.0000	0.0000	0.4030	0.0000
60.0000	0.3320	0.0000	0.0000	0.4030	0.0000
120.0000	0.3320	0.0000	0.0000	0.4030	0.0000
180.0000	0.3320	0.0000	0.0000	0.4030	0.0000
240.0000	0.3320	0.0000	0.0000	0.4030	0.0000
300.0000	0.3260	0.0181	0.0073	0.3957	0.0182
360.0000	0.2960	0.1084	0.0437	0.3593	0.1148
420.0000	0.2380	0.2831	0.1141	0.2889	0.3329
480.0000	0.1840	0.4458	0.1797	0.2233	0.5902
540.0000	0.1440	0.5663	0.2282	0.1748	0.8353
600.0000	0.1240	0.6265	0.2525	0.1505	0.9849
660.0000	0.1200	0.6386	0.2573	0.1457	1.0176
720.0000	0.1180	0.6446	0.2598	0.1432	1.0345
780.0000	0.1180	0.6446	0.2598	0.1432	1.0345
840.0000	0.1180	0.6446	0.2598	0.1432	1.0345
900.0000	0.1180	0.6446	0.2598	0.1432	1.0345

**Table 0.3 - Common bond dissociation enthalpies<sup>96</sup>**

Single Bonds	$\Delta H^\circ^*$	Single Bonds	$\Delta H^\circ^*$	Multiple Bonds	$\Delta H^\circ^*$
H-H	104.2	B-F	150	C=C	146
C-C	83	B-O	125	N=N	109
N-N	38.4	C-N	73	O=O	119
O-O	35	N-CO	86	C=N	147
F-F	36.6	C-O	85.5	C=O (CO <sub>2</sub> )	192
Si-Si	52	O-CO	110	C=O (aldehyde)	177
P-P	50	C-S	65	C=O (ketone)	178
S-S	54	C-F	116	C=O (ester)	179
Cl-Cl	58	C-Cl	81	C=O (amide)	179
Br-Br	46	C-Br	68	C=O (halide)	177
I-I	36.	C-I	51	C=S (CS <sub>2</sub> )	138
H-C	99	C-B	90	N=O (HONO)	143
H-N	93	C-Si	76	P=O (POCl <sub>3</sub> )	110
H-O	111	C-P	70	P=S (PSCl <sub>3</sub> )	70
H-F	135	N-O	55	S=O (SO <sub>2</sub> )	128
H-Cl	103	S-O	87	S=O (DMSO)	93
H-Br	87.5	Si-F	135	P=P	84
H-I	71	Si-Cl	90	P≡P	117
H-B	90	Si-O	110	C≡O	258
H-S	81	P-Cl	79	C≡C	200
H-Si	75	P-Br	65	N≡N	226
H-P	77	P-O	90	C≡N	213

**Table 0.4 – Average Photodegradation Values for Polyurethane Samples**

<b>Time (hours)</b>	<b>T<sub>1i</sub>(°C)</b>	<b>T<sub>1max</sub>(°C)</b>	<b>Δm<sub>1</sub></b>	<b>Δm<sub>1adj</sub></b>
0	234.8±0.8		2.8±0.9%	2.8±0.9%
24	225.5±0.8	271.5±0.5	4.5±0.1%	4.5±0.1%
48	206.0±0.3	264.0±1.3	5.4±0.2%	5.4±0.2%
72	202.0±0.9	264.2±0.3	6.2±0.8%	6.2±0.8%
96	198.9±1.2	263.3±0.4	7.4±0.2%	7.4±0.2%
<b>Time (hours)</b>	<b>T<sub>2i</sub>(°C)</b>	<b>T<sub>2max</sub>(°C)</b>	<b>Δm<sub>2</sub></b>	<b>Δm<sub>2adj</sub></b>
0	277.6±18.8	370.6±3.8	45.4±2.1%	45.4±2.1%
24	286.1±1.9	389.4±0.1	47.8±1.1%	47.8±1.1%
48	291.7±0.5	395.3±6.6	46.4±2.2%	46.4±2.2%
72	281.9±18.1	370.7±22.7	48.9±4.6%	48.9±4.6%
96	295.8±3.2	376.1±6.0	46.5±2.3%	46.5±2.3%
<b>Time (hours)</b>	<b>T<sub>3i</sub>(°C)</b>	<b>T<sub>3max</sub>(°C)</b>	<b>Δm<sub>3</sub></b>	<b>Δm<sub>3adj</sub></b>
0	404.7±5.2	438.0±0.1	49.8±1.8%	49.8±1.8%
24	414.2±1.4	438.2±1.2	43.0±1.3%	43.0±1.3%
48	413.6±1.3	439.6±0.6	42.4±2.0%	42.4±2.0%
72	413.2±0.7	437.9±2.8	38.7±2.7%	38.7±2.7%
96	412.9±0.4	438.1±2.0	38.7±1.8%	38.7±1.8%
<b>Time (hours)</b>	<b>Residue</b>	<b>Total</b>	<b>Mass Adjusted</b>	
0	1.4±0.2%	99.4±0.2%	98.0±0.1%	
24	4.3±0.6%	99.6±0.1%	95.3±0.5%	
48	5.2±0.3%	99.4±0.1%	94.3±0.2%	
72	5.9±1.1%	99.6±0.1%	93.7±1.1%	
96	6.8±0.7%	99.5±0.5%	92.7±1.1%	

**Table 0.5 – Average Photocatalytic Degradation Values for 5wt% TiO<sub>2</sub>-PU Composites Produced by the Monomer Functionalization Method**

<b>Time (hours)</b>	<b>T<sub>1i</sub>(°C)</b>	<b>T<sub>1max</sub>(°C)</b>	<b>Δm<sub>1</sub></b>	<b>Δm<sub>1adj</sub></b>
0	246.5±3.0		3.6±0.1%	3.8±0.1%
24	228.1±2.9	269.6±2.1	4.6±0.4%	4.8±0.4%
48	218.4±0.8	265.1±1.4	5.1±0.4%	5.4±0.4%
72	219.8±1.4	265.5±1.3	5.8±0.1%	6.1±0.1%
96	216.7±1.2	263.1±1.6	6.9±0.2%	7.2±0.2%
<b>Time (hours)</b>	<b>T<sub>2i</sub>(°C)</b>	<b>T<sub>2max</sub>(°C)</b>	<b>Δm<sub>2</sub></b>	<b>Δm<sub>2adj</sub></b>
0	288.2±1.2	381.4±1.8	39.6±0.4%	41.7±0.4%
24	290.1±1.2	383.0±1.7	41.3±1.4%	43.5±1.4%
48	284.7±1.2	370.1±5.1	44.2±2.3%	46.5±2.3%
72	288.6±1.1	375.0±1.4	45.8±1.6%	48.2±1.7%
96	295.7±5.1	374.0±1.6	45.2±0.2%	47.6±0.2%
<b>Time (hours)</b>	<b>T<sub>3i</sub>(°C)</b>	<b>T<sub>3max</sub>(°C)</b>	<b>Δm<sub>3</sub></b>	<b>Δm<sub>3adj</sub></b>
0	400.1±0.2	433.6±2.1	48.4±0.9%	51.0±0.9%
24	407.4±0.9	438.6±2.0	46.8±1.0%	49.3±1.1%
48	406.9±0.3	432.4±1.2	43.0±1.3%	45.3±1.4%
72	406.3±0.4	427.0±0.9	38.7±3.5%	40.7±3.7%
96	406.3±0.5	430.3±1.1	39.0±0.9%	41.1±0.9%
<b>Time (hours)</b>	<b>Residue</b>	<b>Total</b>	<b>Mass Adjusted</b>	
0	7.7±0.9%	99.4±0.2%	96.5±1.1%	
24	6.9±0.9%	99.6±0.2%	97.6±1.1%	
48	7.3±0.5%	99.6±0.1%	97.1±0.6%	
72	9.4±1.7%	99.7±0.2%	95.0±2.0%	
96	8.3±1.2%	99.4±0.5%	95.9±0.7%	

**Table 0.6 - Average Photocatalytic Degradation Values for 5wt% TiO<sub>2</sub>-PU Composites Produced by the Polymer Functionalization Method**

<b>Time (hours)</b>	<b>T<sub>1i</sub>(°C)</b>	<b>T<sub>1max</sub>(°C)</b>	<b>Δm<sub>1</sub></b>	<b>Δm<sub>1adj</sub></b>
0	236.1±2.5		3.9±0.1%	4.1±0.1%
24	226.2±1.3	271.4±0.4	5.1±0.2%	5.4±0.2%
48	206.7±1.4	264.0±0.7	5.8±0.2%	6.1±0.2%
72	201.3±1.2	263.7±0.8	6.5±0.3%	6.9±0.4%
96	198.9±0.8	262.9±0.3	6.7±0.1%	7.1±0.1%
<b>Time (hours)</b>	<b>T<sub>2i</sub>(°C)</b>	<b>T<sub>2max</sub>(°C)</b>	<b>Δm<sub>2</sub></b>	<b>Δm<sub>2adj</sub></b>
0	292.9±3.2	370.2±1.8	37.4±0.7%	39.4±0.7%
24	296.7±1.1	368.9±3.2	40.4±0.3%	42.5±0.3%
48	293.4±1.1	382.4±3.5	42.3±1.0%	44.6±1.1%
72	290.3±0.7	374.9±2.1	40.3±0.7%	42.4±0.7%
96	291.7±0.7	377.1±0.7	41.1±0.1%	43.3±0.1%
<b>Time (hours)</b>	<b>T<sub>3i</sub>(°C)</b>	<b>T<sub>3max</sub>(°C)</b>	<b>Δm<sub>3</sub></b>	<b>Δm<sub>3adj</sub></b>
0	401.2±1.1	434.5±1.1	50.5±0.4%	53.2±0.5%
24	398.4±1.3	429.3±0.8	46.2±0.3%	48.6±0.3%
48	407.2±1.4	433.7±1.4	42.0±0.9%	44.2±0.9%
72	401.8±0.7	432.3±1.4	42.6±0.6%	44.9±0.7%
96	404.6±1.0	432.4±0.3	41.5±0.5%	43.7±0.5%
<b>Time (hours)</b>	<b>Residue</b>	<b>Total Mass</b>	<b>Mass Adjusted</b>	
0	7.6±0.1%	99.5±0.3%	96.7±0.4%	
24	7.8±0.3%	99.5±0.3%	96.5±0.3%	
48	9.4±0.3%	99.5±0.3%	94.8±0.3%	
72	10.1±0.3%	99.6±0.1%	94.2±0.6%	
96	10.3±0.5%	99.6±0.1%	94.0±0.3%	

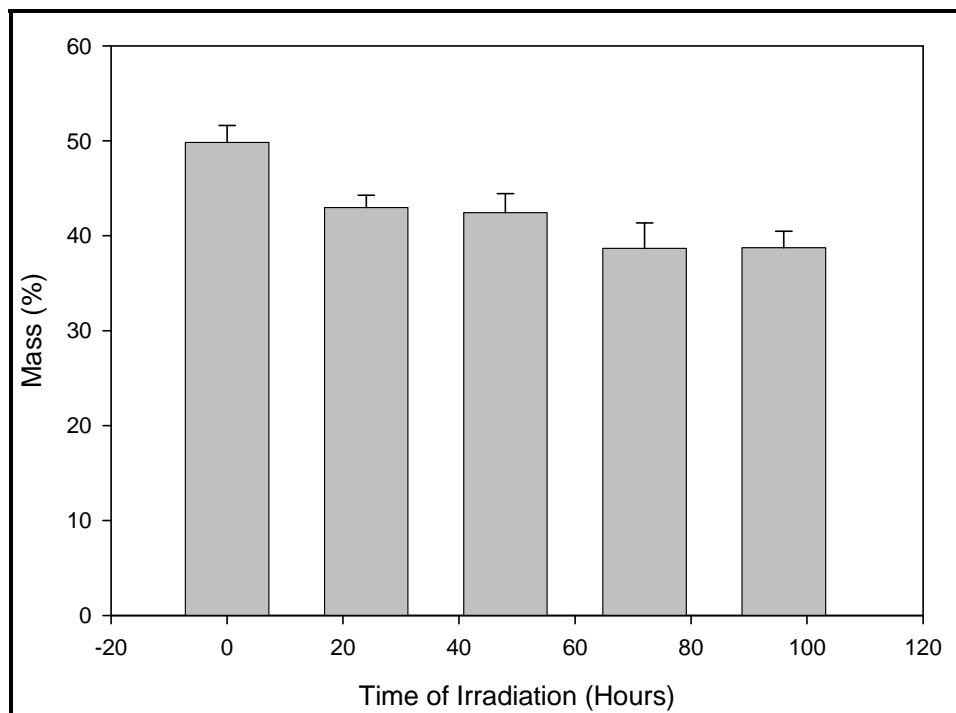


**Figure 0.1 - Soft Segment Degradation for Decreasing Mass % with Increasing Time of Irradiation – PU Elastomers.**

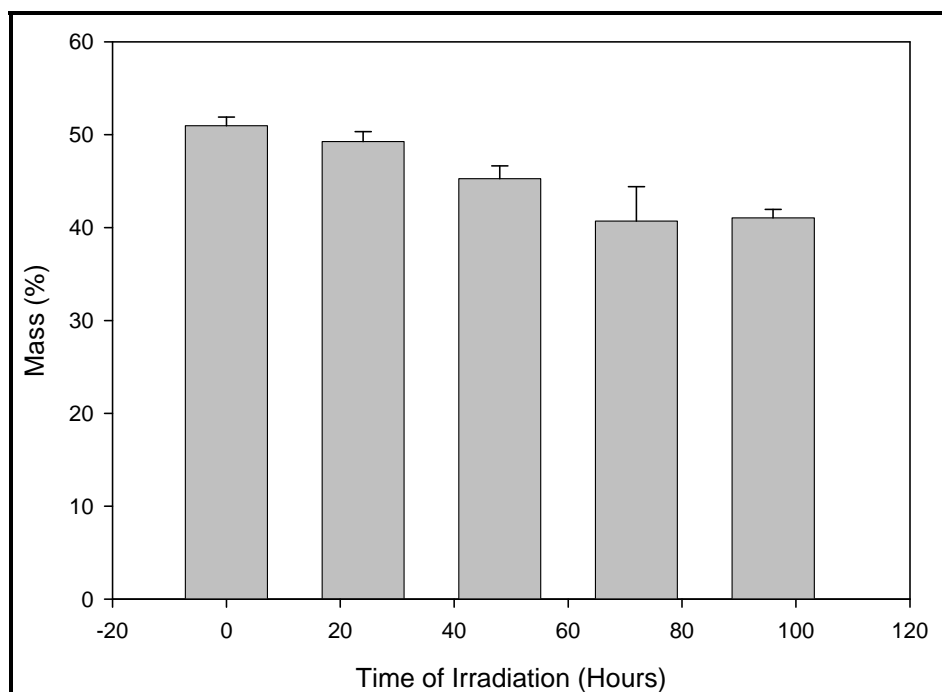


**Figure 0.2 - Soft Segment Degradation for Decreasing Mass % with Increasing Time of Irradiation – 5wt% TiO<sub>2</sub>-PU Composite – Monomer Method.**

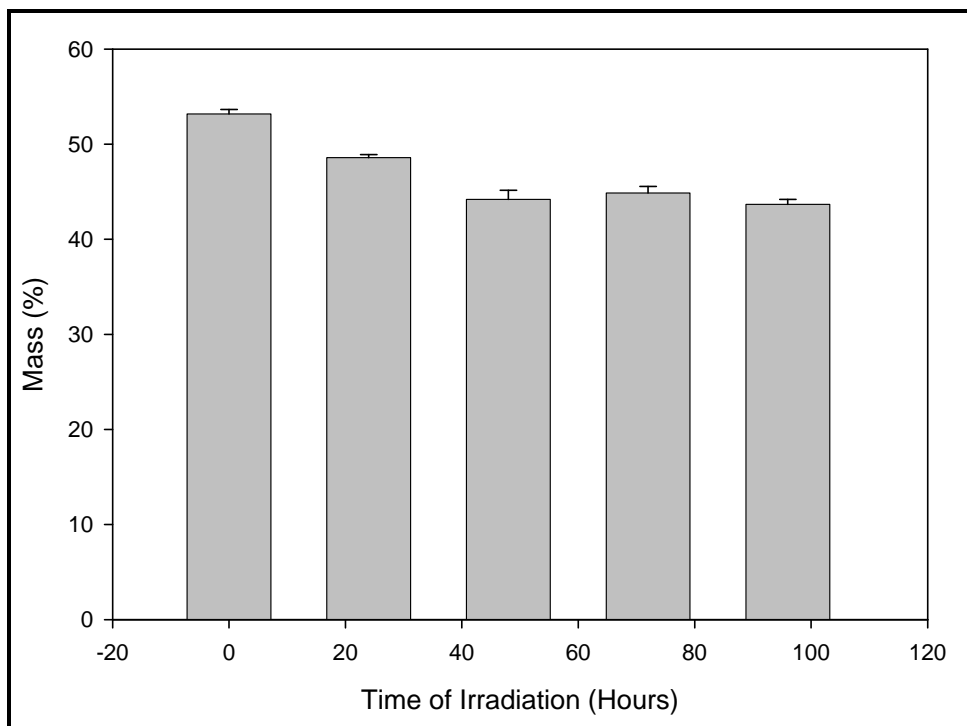


**Figure 0.3 - Soft Segment Degradation for Decreasing Mass % with Increasing Time of Irradiation – 5wt% TiO<sub>2</sub>-PU Composite – Polymer Method.**

## CURRICULUM VITAE

**Kevin David Burgess**

---

### Education

---

**The University of Western Ontario, London, ON** 2005-2007  
**Chemical and Biochemical Engineering**  
*M.E.Sc. Graduate*  
Thesis Title: Self-Cleaning Titania-Polyurethane Composites  
Chief Advisor: Dr. Paul A. Charpentier

**The University of Western Ontario, London, ON** 2001-2005  
**Chemical and Biochemical Engineering**  
*B.E.Sc. Graduate*

---

### Honors and Awards

---

Western Engineering Scholarship 2005-2007  
World Petroleum Congresses Millennium Scholarship 2003-2004  
Western Entrance Scholarship 2001-2002  
Munday and Associates Business Award 2000-2001

---

### Related Work Experiences

---

**The University of Western Ontario, London, ON** 2005-2007  
Department of Chemical Engineering  
*Graduate Research Assistant*

**The University of Western Ontario, London, ON** 2005-2007  
Department of Chemical Engineering  
*Graduate Teaching Assistant, Industrial Organic Chemistry*

**The University of Western Ontario, London, ON** 2005-2007  
Richard Ivey School of Business  
*Teaching Assistant, Business for Engineers*

---

### Publications and Presentations

---

EMK/MMO Poster Presentations 2005-2007  
Western Research Day Poster Presentation 2006-2007